



**UNIVERSITY OF BRASILIA**  
**FACULTY OF TECHNOLOGY**  
**DEPARTMENT OF CIVIL AND ENVIRONMENTAL ENGINEERING**

**SITE CHARACTERIZATION AND ANALYSIS OF LANDSLIDE  
DYNAMICS UNDER THE INFLUENCE OF TRIGGERING FACTORS  
BY GEOPHYSICAL METHODS**

**Yawar Hussain**

**Supervisor: Hernan Eduardo Martinez-Carvajal, DSc**

**Co-supervisor: Juan Felix Rodriguez Rebolledo, DSc**

**-Brasilia-**

UNIVERSITY OF BRASÍLIA  
FACULTY OF TECHNOLOGY  
DEPARTMENT OF CIVIL AND ENVIRONMENTAL ENGINEERING

SITE CHARACTERIZATION AND ANALYSIS OF LANDSLIDE DYNAMICS  
UNDER THE INFLUENCE OF TRIGGERING FACTORS BY GEOPHYSICAL  
METHODS

YAWAR HUSSAIN

TESE DE DOUTORADO SUBMETIDA AO DEPARTAMENTO DE ENGENHARIA CIVIL  
E AMBIENTAL DA UNIVERSIDADE DE BRASÍLIA COM PARTE DOS REQUISITO  
NECESSÁRIO PARA A OBTENÇÃO GRAU DE DOUTOR.

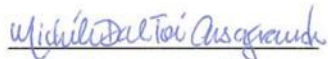
APROVADA POR:



HERNAN EDUARDO MARTINEZ-CARVAJAL, D.Sc. (ENC/UnB)  
(ORIENTADOR)



JUAN FELIX RODRIGUEZ REBOLLEDO, D.Sc. (ENC/UnB)  
(COORDINADOR)



MICHÉLE DAL TOÉ CASAGRANDE, D.Sc. (ENC/UnB)  
(EXAMINADOR INTERNO)



GASPAR MONSALVE MEJIA, Ph.D. (GEOPHY/UNAL)  
(EXAMINADOR EXTERNO)



JUAN CARLOS OLARTE, Ph.D. (ENG/UNAL)  
(EXAMINADOR EXTERNO)

## FICHA CATALOGRÁFICA

**HUSSAIN, Y.**

Site characterization and analysis of landslide dynamics under the influence of triggering factors by geophysical methods, 2018. xiv, 103p. (ENC/FT/UnB, Doutor, Geotecnia, 2018).

Tese de Doutorado. Programa de Pós-Graduação em Geotecnia Universidade de Brasília. Faculdade de Tecnologia. Departamento de Engenharia Civil e Ambiental.

- |                                 |                           |
|---------------------------------|---------------------------|
| 1. Ambient Noise Interferometry | 2. Expander Body Pile     |
| 3. Dispersion Curve             | 4. Nanoseismic Monitoring |
| 5. Prototype Experiment         |                           |

I. ENC/FT/UnB                      II. Título (série)

## REFERÊNCIA BIBLIOGRÁFICA

HUSSAIN, Y. (2018). Site characterization and analysis of landslide dynamics under the influence of triggering factors by geophysical methods, Publicação G.TD-149/18, Tese de Doutorado, Programa de Pós-Graduação em Geotecnia, Departamento de Engenharia Civil e Ambiental, Universidade de Brasília, Brasília, DF, 103p.

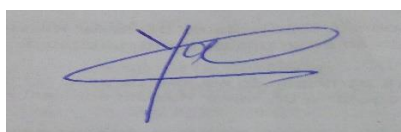
## CESSÃO DE DIREITOS

NOME DO AUTOR: Yawar Hussain

TÍTULO DA TESE: Site characterization and analysis of landslide dynamics under the influence of triggering factors by geophysical methods

GRAU / ANO: Doutor/2018

É concedida à Universidade de Brasília a permissão para reproduzir cópias desta tese de doutorado e para emprestar ou vender tais cópias somente para propósitos acadêmicos e científicos. O autor reserva outros direitos de publicação e nenhuma parte desta tese de doutorado pode ser reproduzida sem a autorização por escrito do autor.



Yawar Hussain

SCLN-114 Boloco-C App. 108 Asa Norte Brasília Brasil.

E-mail: [yawar.pgn@gmail.com](mailto:yawar.pgn@gmail.com)

## ACKNOWLEDGEMENT

I would like to thank my supervisor Dr. Hernan Martinez-Carvajal and my co-supervisor Dr. Juan Felix for their continuous support during my research. I would also like to thank Dr. Martin Cardenas-Soto (UNAM) and Dr. Salvatore Martino (University of Rome, Italy) for helping me in all stages of my PhD. I am thankful to Dr. Rogerio Uagoda and his research group (UnB), Dr. Soares and his team, Dr. Marcelo Rocha (UnB), Dr. Clebber (FUG) and their students and members of PhyGeo (UnB) for their help in the data acquisition. Along with them I would also like to thank number of PhD students (Cristobal Condori, Alexandre Moreno) and Postdoctoral fellows (Noami Villamoze and Gregious Yftanis) for the helps they offered at the initial stage of my research.

I would also like to mention the names of different funding bodies involved in this research such as CNPq, FAPDF. Thanks to the Pool of Brazil Geophysical Equipment, Rio de Janeiro for lending seismometers used in this study.

Last but not the least, I would like to thank my family and my wife for their continuous support and encouragement.

## **ABSTRACT**

Landslides are results of natural geomorphological processes that alter the physical properties of the site. These anomalous alterations in the geomaterials can lead to microseismic emissions and can also change the properties of ambient noise waves propagating through them both of which can be detected by the application of geophysical techniques (cheaper, noninvasive and applicable).

The subsurface characterization (geophysical techniques) of landslide site is done in the first stage where Multi-Channel Analysis of Surface Waves (MASW), Electrical Resistivity Tomography (ERT) and Horizontal to Vertical Spectral Ratio (HVSr) methods are used.

In the second stage, the dynamic analysis of landslide is done with ambient noise and emitted microseismicity. The seasonal changes in stiffness of landslide mass is analyzed by time-lapse HVSr (natural frequency) and ambient noise interferometry (relative velocity change). The results are optimized by a field scaled prototype experiments in the experimental field of the University of Brasilia, Brazil where the normal load was kept on rising on the soil. Finally, a typological analysis on the seismic records of landslide and at a controlled scale experiment is performed.

Resultant slip surface and permeable paths were identified well on the modeled resistivity sections, while a three layered 2D shear wave velocity stratigraphic section is obtained from MASW where a continuous increasing rigidity trend and a decrease in velocity at landslide scarp are observed. The seismic noise recorded at different sites in the landslide is analyzed in order to reconstruct the landslide geometry and its seasonal dynamics. Resultant HVSr curves are divided into three groups based on the frequency peak values, each one is a representative of a mutually detached randomly scattered dynamic zones created by the erosional (fluvial) effects of the underlying Capetinga river. The HVSr along with ambient noise f-k curves are used for the estimation of 1-D shear wave velocity as well. Results of the prototype experiment show two frequency peaks at HVSr curve, the amplitude variations at higher frequency peak at different stress levels in the soil are observed. A decrease of -0.6 % in  $dV/V$  was observed before the soil collapse in plate loading test. Neither ANI nor HVSr shows the seasonal response at the landslide.

The short duration signals having a unique typology are observed during pull out tests on expander body pile. The same analysis was applied at Sobradinho landslide where signals of

particular typology are observed during the rainy season which are possibly related with the landslide dynamics or the sediments loads of the river.

The study will prove effective in understanding precollapse dynamics of unstable slopes in clayey formations in terms of seasonal variations in rigidity, alteration in physical properties, stress accumulation phases in the soil, seasonal changes in resonance, and typology of the seismic records.

Keywords: Ambient Noise Interferometry; Expander Body Pile; Dispersion Curve; Nanoseismic Monitoring; Prototype Experiment

## RESUME

Deslizamentos de terra são resultados de processos geomorfológicos naturais que alteram as propriedades físicas do local. Essas alterações anômalas nos materiais podem levar a emissões micro-sísmicas e também podem alterar as propriedades das ondas de ruído ambiente se propagando através delas, sendo que ambas podem ser detectadas pela aplicação de técnicas geofísicas (mais baratas, não invasivas e aplicáveis).

A caracterização subsuperficial (técnicas geofísicas) do sítio de escorregamento é feita no primeiro estágio, onde são utilizados os métodos Análise Multicanal de Ondas de Superfície (MASW), Tomografia de Resistividade Elétrica (ERT) e Relação Espectral Horizontal para Vertical (HVSR).

Na segunda etapa, a análise dinâmica do escorregamento é feita com ruído ambiente e micro-sismicidade emitida. As mudanças sazonais na rigidez da massa de escorregamento são analisadas por HVSR com lapso de tempo (frequência natural) e interferometria de ruído ambiente (mudança de velocidade relativa). Os resultados são otimizados por um experimento de talude normal de campo, em escala de campo, no campo experimental da Universidade de Brasília, Brasil, onde a carga normal foi mantida na elevação do solo. Finalmente, uma análise tipológica dos registros sísmicos de escorregamentos e em um experimento em escala controlada.

A superfície de escorregamento resultante e os caminhos permeáveis foram identificados bem nas seções de resistividade modeladas, enquanto a seção estratigráfica de velocidade de onda de cisalhamento 2D de três camadas é obtida pelo MASW onde uma tendência de rigidez crescente contínua e diminuição da velocidade na escarpa é observada. O ruído sísmico registrado em diferentes locais no escorregamento é analisado para reconstruir a geometria do escorregamento e sua dinâmica sazonal. As curvas de HVSR resultantes são divididas em três grupos com base nos valores de pico de frequência, cada um representando as zonas dinâmicas aleatoriamente dispersas e mutuamente separadas criadas pelos efeitos erosionais (fluviais) do rio de Capetinga subjacente. O HVSR juntamente com as curvas de ruído ambiente f-k são usados para a estimativa da velocidade de onda de cisalhamento 1-D também. Os resultados do experimento protótipo mostram dois picos de frequência na curva HVSR, as variações de amplitude no pico de maior frequência em diferentes acumulações de estresse no solo são

observadas. Uma diminuição de -0,6% em  $dV / V$  foi observada antes do colapso do solo no teste de carga da placa. Nem o ANI nem o HVSR mostram a resposta sazonal no deslizamento.

Os sinais de curta duração, com uma tipologia única, são observados durante os testes de retirada da pilha do corpo de expansão. A mesma análise foi aplicada ao deslizamento de terra de Sobradinho, onde os sinais de uma tipologia particular são observados durante a estação chuvosa, possivelmente relacionados com a dinâmica do escorregamento ou as cargas de sedimentos do rio.

O estudo será eficaz na compreensão da dinâmica pré-colapso de encostas instáveis em formações argilosas em termos de variações sazonais na rigidez, alteração nas propriedades físicas, fases de acumulação de tensão no solo, mudanças sazonais na ressonância e tipologia dos registros sísmicos.

Palavras-chave: Interferometria de Ruído Ambiente; Curva de Dispersão; Ensaio protótipo; Monitoramento Nanosísmico; Pilha de corpo de expansão.

## TABLE OF CONTENTS

1. INTRODUCTION	1
1.1. PROBLEM STATEMENT	1
1.2. LANDSLIDE TYPES	2
1.3. LANDSLIDE TRIGGERS	3
1.4. LANDSLIDE MONITORING TECHNIQUES	3
1.5. GENERAL OBJECTIVE	4
1.6. SPECIFIC OBJECTIVES	4
1.7. SCOPE	4
1.8. THESIS OUTLINES	5
2. MATERIAL AND METHODS	6
2.1. GEOPHYSICAL TECHNIQUES	6
2.1.1. AMBIENT NOISE BASED TECHNIQUES	6
2.1.1.1. AMBIENT NOISE INTERFEROMETRY	7
2.1.1.2. HORIZONTAL TO VERTICAL SPECTRAL RATIO	10
2.1.1.3. MULTI-CHANNEL ANALYSIS OF SURFACE WAVE	12
2.2. SEISMIC EMISSION BASED APPROACHES	13
2.2.1. NANOSEISMIC MONITORING	14
2.2.1.1. MINI-ARRAY	15
2.2.1.2. DATA PROCESSING	16
2.2.1.3. SONOGRAMS AND SUPERSONOGRAMS	16
2.2.1.4. HYPOLINE AND JACKKNIFING	17
2.2.1.5. NANOSEISMIC SUITE	18
2.2.1.6. SIGNAL NOMENCLATURE	18
2.2.1.7. EVENT LOCATION	19
2.2.1.7.1. ABSOLUTE LOCATION	19
2.2.1.7.2. RELATIVE LOCATION	23
2.2.1.8. MAGNITUDE	24
2.2.1.9. LIMITATIONS	24
2.3. OTHER GEOPHYSICAL TECHNIQUES	25
2.3.1. ELECTRICAL RESISTIVITY METHOD	25
2.3.2. GROUND PENETRATION RADAR	25
2.3.3. GEODETIC MONITORING	26
24. APPLICATIONS	27
2.4.1. APPLICATIONS OF NM	27

2.4.1.1. LANDSLIDE MONITORING	27
2.4.1.2. MONITORING OF GRAVITY-INDUCED SLOPE	31
2.4.1.3. STRUCTURAL HEALTH MONITORING	31
2.4.1.4. CLIFF EROSION MONITORING	32
2.4.1.5. PRE-COLLAPSE IDENTIFICATION OF SINKHOLES	32
2.4.1.6. HYDRAULIC FRACTURING	33
2.4.1.7. ACTIVE FAULT MAPPING	33
2.4.1.8. JOINT APPLICATIONS	33
2.4.2. APPLICATIONS OF GEOPHYSICS TO LANDSLIDE DYNAMICS	34
2.4.2.1. TIME-LAPSE LANDSLIDE MONITORING	35
2.4.2.2. GEOPHYSICS FOR LANDSLIDE SITE CHARACTERIZATION	37
2.4.3. SUITABILITY OF APPLIED TECHNIQUES	38
2.5. APPLIED METHODOLOGY	40
2.5.1. SOBRADINHO LANDSLIDE	41
2.5.1.1. GEOLOGY AND GEOTECHNICAL PARAMETERS	42
2.5.2. FIELD SCALED EXPERIMENT	45
2.5.2.1. NORMAL SLOPE EXPERIMENT	45
2.5.2.2. EXPERIMENT ON EXPANDER BODY PILE	47
2.6. DATA ACQUISITION AND PROCESSING	49
2.6.1. ERT AND MASW	49
2.6.2. AMBIENT NOISE INTERFEROMETRY PROCESSING	52
2.6.2.1. COMPUTATION OF CROSS-CORRELATION FUNCTIONS	54
2.6.2.2. MOVING-WINDOW CROSS-SPECTRAL (MWCS) TECHNIQUE	56
3. RESULTS AND DISCUSSIONS	57
3.1. SITE CHARACTERIZATION	57
3.1.1. MASW AND ERT	57
3.1.2. ELECTRICAL RESISTIVITY TOMOGRAPHY	59
3.2. NOISE CHARACTERIZATION	62
3.2.1. SPD AND PDF	62
3.2.2. FREQUENCY-WAVENUMBER	64
3.3. JOINT INVERSION	66
3.4. HVSr	69
3.4.1. FIELD SCALE EXPERIMENT	69
3.4.2. UBIQUITOUS FREQUENCY	70
3.4.3. LANDSLIDE FREQUENCY	72

3.4.4. FLAT HVSR	73
3.4.5. SEASONAL ANALYSIS	74
3.5. AMBIENT NOISE INTERFEROMETRY	76
3.5.1. CROSS-CORRELATION FUNCTION	76
3.5.2. PROTOTYPE EXPERIMENT	77
3.5.2.1. TERRESTRIAL LASER SCANNING	79
3.5.2. SOBRADINHO LANDSLIDE	79
4. DISCUSSION AND CONCLUSIONS	85
5. RECOMMENDATIONS	88
REFERENCES	92

## LIST OF FIGURES

Figure 1 Schematic presentation of ANI with working principle of MWCS technique (Modified after Jonsdottir, 2018).....	8
Figure 2 Data acquisition with SNS (Sick et al., 2014) .....	15
Figure 3 An example of Sonogram (Sick et al., 2014).....	17
Figure 4 A presentation of supersonogram (Sick et al., 2014) .....	17
Figure 5 Snogram with waveform of collapse and failure events (Fiorucci et al., 2017). ...	19
Figure 6 (a) Hyperbolae with two sensors at the foci and a signal solution (source location). (b) Intersection of three hyperbolae obtained from the distance of source and sensors. Dotted and solid lines are the initial and final solutions, respectively (Modified after Silva, 2010). .....	20
Figure 7 (a) Wavefront incident on sensor S1 at time t1, after a time $\Delta t = t_2 - t_1$ on sensor S2 at angle. (b) Here wavefront incident perpendicularly. (c) Velocity wavefront $\alpha$ incident on the earth's surface at an angle $i$ .....	22
Figure 8 Principle procedure of event location with network processing including data from three stations. Sketch in (a) shows the intersection of a horizontal plane at depth. Sketch in (b) is a zoom window of (a) (Häge & Joswig, 2009).....	23
Figure 9 Methodological workflow explaining the stepwise application of the techniques along with their objectives. ....	41
Figure 10 (A) Location of Ribeirão Contagem watershed on Federal District map, (B its geology, (C) Sobradinho landslide along with HVSR measuring points (red dots), red dashed ellipse is the landslide boundary and (D) zoomed landslide image with triangular array used for time lapse monitoring.....	43
Figure 11 (A) Outcrops of rocks in the higher elevation areas, with a low degree of weathering. B) Saprolite with fragments of quartzite with micaceous minerals. C) Profile photo with alluvial deposit superimposed on the alluvium .....	44
Figure 12 Prototype field experiment (compressional test) in the University of Brasilia. Position of the seismometers (A) as well as loading mechanism (B) are shown. ....	46
Figure 13 Experimental setup dimension of excavation, reaction piles, positions of seismometers, location of artificial source of ambient noise and presentation of loading mechanism.....	47
Figure 14 (A) Mini-array configuration (B) its blind zone (Personal communication, Salvatore Martino) (C) Mechanism used for extraction test on expendable body pile and (D) SPT-N profile of the soil of the experimental site.....	48

Figure 15 MASW acquisition geometry at three profiles (top to bottom L1, L2 and L3) Inverted triangles are the source positions while blue dots are the positions of geophones. ....	50
Figure 16 (A) Seismogram of the profile L2 and apparent resistivity values at profile ERT-2 are shown. ....	51
Figure 17 Ambient noise processing work-flow starting from Raw data and ends in the estimation of changes in relative velocity (dV/V). ....	53
Figure 18 One hour record of ambient noise (A). Unprocessed trace is displayed after normalization (C). A segment of 30 sec around a transient event (B). Units in the figure are arbitrary. ....	54
Figure 19 Velocity spectrum (Velocity vs Frequency) along with interpreted dispersion curves (solid lines) over three profiles (from left to right L1, L2, and L3). The color scale presents amplitude values.....	58
Figure 20 Results of MASW a 2D shear wave velocity profile of the area (L1 to L3 top to bottom). Color bars are the Vs velocities in km/sec.....	59
Figure 21 Inversion results of electrical resistivity tomography at Sobradinho landslide. The black dotted line shows landslide area which is zoomed in Figure 22.....	60
Figure 22 Zoomed image of the profile shown in Figure 21, which shows the subsurface structure of the landslide .....	61
Figure 23 Longitudinal profile of length 280m taken along the landslide.....	62
Figure 24 Time-frequency plot of PSD variations for S1. Color bar presents energy levels in decibels [dB] relative to the velocity ( $10 \log_{10} [(m/s)^2 / Hz]$ ). Dashed white squares indicate different phases of noise energy. ....	63
Figure 25 PDF of vertical component of S1 (inside) and S8 (outside) the Sobradinho landslide. ....	64
Figure 26 The f-k analysis of E-W component, results as a function of the velocity (top), and results as a function of the backazimuth (bottom). ....	65
Figure 27 Dispersion of recorded noise wave field of Julian day 307. After 7 Hz there are little variations in phase velocity of wave with frequency. ....	65
Figure 28 HVSR curve at S1 station (black line) and its standard deviation, and set of solutions (color lines) of joint inversion results. The best fit curve is the red color line. Bar scale color indicates the best misfit curves to experimental HVSR curve. ....	67
Figure 29 Set of solutions (color lines) of joint inversion results for f-k dispersion curve (black line). The bestfit curve is the red color line. Bar scale color indicates the best misfit curves to experimental HVSR curve.....	67

Figure 30 Set of solutions (color lines) of joint inversion results for final subsoil models. The bestfit curve is the red color line. Bar scale color indicates the mistfit curves to experimental HVSR curve. ....	68
Figure 31 The HVSR curves produced at each loading episode. The Zoomed image second peak is shown in the box. The load displacement curve is also shown (below).....	70
Figure 32 HVSR curves class A, peaks at 2 Hz and 4-6 Hz. The two dashed lines represent the HVSR standard deviation, while the gray areas represent the peak frequency standard deviation, which quantifies the experimental error associated with the average peak frequency value. Below is results of spectrum rotate at each point, y-axis is azimuth in degree and x-axis is the frequency. ....	71
Figure 33 HVSR curves of class B, peaks at 2 Hz and 8-10 Hz. The two dashed lines represent the HVSR standard deviation, while the gray areas represent the peak frequency standard deviation, which quantifies the experimental error associated with the average peak frequency value. Below is the results of spectrum rotate at each point, y-axis is azimuth in degree and x-axis is the frequency. ....	73
Figure 34 Class C, no peak/flat response of the strata on the HVSR curves. Dotted lines are HVSR standard deviation, while the gray areas represent the peak frequency standard deviation, which quantifies the experimental error associated with the average peak frequency value...	74
Figure 35 Seasonal response of HVSR curves recorded at triangular array of three sensors. Color presents HVSR amplitude. Station DF01, dry (top), intermediate (middle) and saturated (bottom).....	75
Figure 36 Seasonal response of HVSR curves recorded at triangular array of three sensors. Color presents HVSR amplitude. Station DF02, dry (top), intermediate (middle) and saturated (bottom).....	76
Figure 37 Cross-correlations traces of the prototype normal slope experiment (above), ZZ, RR and TT filtered between 6 and 16 Hz. ....	77
Figure 38 Relative velocity changes between stations PL01-PL02 at RR (top) and TT (middle) and ZZ (bottom) components representative of different stages of plate loading test. ....	78
Figure 39 DEM of the normal slope surface at 5 minute temporal delays from beginning (0) to 25 minute (05). ....	79
Figure 40 Relative velocity changes between stations DF01-DF02 at ZZ component representative of dry (above) and wet (below) conditions. Color bar presents $dV/V$ values...	80
Figure 41 Event screening after 3 hours of the prototype experiment at the end of experiment the signals so identified are linked with the fracturing in the tropical soil. ....	81

Figure 42 Zoomed sonogram images of the small energy fractures (micro-fractures) produced as a result of pullout test on an expendable body pile..... 82

Figure 43 Load-displacement curve of the prototype expander body pile pullout experiment. Maximum soil displacement as well extension tremor are observed between 700-100 KN load. .... 82

Figure 44 Zoom screening using super-sonograms, natural scale a) dry, no prominent slidequakes are observed b) after rainfall events of propagating nature are identified which suspiciously linked the river dynamics. .... 83

Figure 45 Zoomed sonogram presentation of the slidequakes at landslide immediate after the rainfall at two mini-arrays. .... 84

Figure 46 Typologies of the signals observed during rainy season at Sobradinho landslide, recorded using signal station. First row is the sonogram, 2nd and 3rd rows are waveform and spectrum, respectively. .... 85

## List of Tables

Table 1 Number of hyperbolae and triple points as a function of the number of receivers (Joswig, 2008).....	21
Table 2 F-t signatures and principal characteristics of seismic events induced by creeping LS dynamics (Vouillamoz, 2015).....	30
Table 3 MASW and ERT acquisition parameters.....	49
Table 4 The parameters used for dV/V estimation at normal slope as well as at landslide experiments. ....	55

## TERMS USED

---

2-D	Two Dimensional
$\alpha$	Angle of seismic waves with sensor
ANb	Ambient Noise based
ANI	Ambient Noise Interferometry
CC	Cross-correlation
DEM	Digital Elevation Model
dV/V	Relative Change in Velocity
EB	Expander Body
ERT	Electrical Resistivity Tomography
f-k	Frequency-wavenumber
$f_0$	Fundamental Frequency
GPS	Global Positioning System
H	Thickness
HVSR	Horizontal to vertical spectral ratio
Hz	Hertz
K	Geometric Factor
$M_L$	Local Magnitude
MSEED	Mini-SEED
$M_w$	Moment magnitude
MWCS	Moving Window Cross Spectral
NCF	Noise Correlation Function
NM	Nanoseismic Monitoring
SAC	Seismic Analysis Code
SEb	Seismic Emission Based
SNS	Seismic Navigation System
T	Natural Period
UAV	Unmanned Ariel vehicle
$V_p$	P-Wave Velocity
$V_s$	Shear Wave Velocity
$\rho_a$	Apparent Resistivity
DC	Direct Current
RMS	Root Mean Square Error
R	Attenuation Factor
A	Amplitude
CCref	Refrence Cross-correlation

---

---

CFCcur	Current Cros-correlation
ZZ	Vertical-Vertical
RR	Radial-Radial
TT	Transverse-Transverse
EW	Est West component
PDF	Probability Density Function
PSD	Power Spectral Density
SNR	Signal to Noise Ratio
PDM	Power Spectral Density Matrix
TLS	Terrestrial Laser Scanning
FFT	Fast Fourier Transfer
$\tau$	Travel-Time Lag

---

# 1. INTRODUCTION

## 1.1. PROBLEM STATEMENT

Landslide failures may seriously damage the human and environmental resources of the affected region. Shallow and rainfall triggered landslides have a greater share in the global terrestrial hazards (Fernandes and Amaral, 1997) and a significant share of the Brazilian physical hazards. There are shallow rainfall triggered landslides in Brazil. From 1988-2015 period, there were 733 landslides events in 243 municipalities, with 4.000 fatalities. Economic losses, homelessness are the other impacts of these hazardous events, especially in states of *Rio de Janeiro, Sao Paulo, Minas Gerais and Santa Catarina*. The tragedies of 1966, 1967, 1985, 1988, 1995, 2008, 2009, 2010, 2011 and 2014 are the historical reminder of the atrocities caused by the rainfall triggered shallow landslides (Martins et al., 2017).

The area of District Federal (DF) is characterized by the thick and collapsible soil which is less supportive for the civil engineering structures (Araki, 1997). Because of these problematic soil conditions, the shallow slopes of the region are unstable. The growths of population on these unstable slopes have greatly affected the ecosystem of the area by distrusting the natural drainages that are not being compensated by the appropriate managerial landuse planning. Water quality deterioration and soil erosion are the two major environmental responses to these unplanned urban growths on the problematic soil in surrounding areas of DF (Mendonça et al., 1994).

Nevertheless, the involvement of high technicality along with high costs makes early warning systems impossible, especially for landslides in poor countries. There are landslide monitoring and early warning systems available worldwide however, these systems are suffering from poor investments and (EWS) consequently bad standardization. On the other hand, EWSs for landslides prediction are very vulnerable because the influencing parameters are still incompletely or unsatisfactorily understood.

However, in the case of landslide, the failure dynamics is complicated to the fact that signals are generated by two types of processes as endogenic and exogenic. The seismic signals recorded at a landslide are possible results of underlying processes, like deformation and stick-slip within the landslide mass and from exogenous landslide dynamics such as rockfalls, small debris flows (Vouillamoz et al., 2018) or dynamical effects of nearby rivers. The separations of the signals resisting from these two source mechanisms are very important the landslide dynamic analysis.

In the case of soil landslides, the emission of seismic signals is questionable to the fact that there is an absence of brittle failure in these landslides. Along with this, the signals are of low magnitude and soil medium is of high attenuated which make their monitoring challenging by the surface array of sensors.

## 1.2 LANDSLIDE TYPES

Any ground movement such as rockfalls, deep failure of slopes, and shallow debris flows are termed as landslide. Landslide can be classified, according to the most adopted system of classification proposed by Varnes, (1978), on the basis of two terms: material type and movement type. Materials can be distinguished in:

**Rock:** is “a hard or firm mass that was intact and in its natural place before the initiation of movement”.

**Soil:** is “an aggregate of solid particles, generally of minerals and rocks that either was transported or was formed by the weathering of rock in place. Gases or liquids filling the pores of the soil form part of the soil”.

**Earth:** “describes material in which 80% or more of the particles are smaller than 2mm, the upper limit of sand sized particles”.

**Mud:** “describes material in which 80% or more of the particles are smaller than 0.06mm, the upper limit of silt sized particles”.

**Debris:** “contains a significant proportion of coarse material; 20% to 80% of the particles are larger than 2mm, and the remainder are less than 2mm”.

The terms used should describe the displaced material in the landslide before it was displaced. The types of movement describe how the landslide movement is distributed through the displaced mass. The five kinematically distinct types of movement are described in the sequence fall, topple, slide, spread and flow. Combining the two terms gives classifications such as Rockfall, Rock topple, Debris slide, Debris flow, Earth slide, Earth spread.

### **1.3. LANDSLIDE TRIGGERS**

Triggers are considered as those mechanisms that act on the landslide because of some external sources (natural, man-made or both). The changes in soil rigidity because of varying degree of rainfall induced saturation is one of the most common landslide triggering mechanism, especially in soft sediment landslide. Due to the involvement of multiprocess like tree roots, soil loosening make identification of such trigger mechanism difficult. The identification of these trigger at natural scale lies beyond the scope of the present study. However, in controlled prototype experiments where a known trigger (applied load) is used. Again applied methodologies are not used for the identification of triggers like loading, they are only used for the creation of microfractures in the soil that are monitored by using geophysical methods.

### **1.4. LANDSLIDE MONITORING TECHNIQUES**

A detailed description of these techniques is provided in the next chapter. There are three main techniques used for the analysis of landslides. However, each one has its own merits and demerits and their choice depends on the site conditions, budget in hand and the study objectives.

In an initial site visit, the possible conditions of landslide are seen. The optimal positions for the sensors are marked. Based on this next survey are planned. The better roads to reach the site are marked as well as safe working conditions are ensured.

In situ geotechnical site investigations is another commonly adopted techniques which consist of soil sampling and in situ testing. These techniques provide the most accurate results. However, high costs and measurements at point are the drawbacks of the techniques.

Geophysical techniques aimed at measuring the physical alteration in the land because of the occurrence of landslide which are easy to be carried out, however, the interpretations of their results are ambiguous and need special attention. These are very common in these days, used for the determination of landslide displacements from a distant position and its site characterization.

The geodetic techniques often combined with geophysical techniques that provide the surficial displacement especially in the dynamic analysis of landslides. The detailed of all these techniques are presented in the methodology section.

### **1.5. GENERAL OBJECTIVE**

The main aim of this study is the soft landslide (soil) site characterization as well as the analysis of its dynamics under the influence of triggering factors such as rain (saturation, pore pressure and river erosional effects). The applied stresses from controlled (prototype) to natural experimental conditions are studied. In these experiments, stress is applied on the soil in order to monitor its effects on the soil, in the form the released energy (NM), and alteration in the properties of ambient noise wave-fields while passing through changed soil states (microfracturing). However, the effects of stress field change are not monitored with geophysical techniques.

### **1.6. SPECIFIC OBJECTIVES**

The present study is conducted to fulfill the following specific objectives.

- Near surface characterization of the area by geophysical means.
- Ambient noise characterization of the area.
- Delineation of mechanical resonance and directional response of deformed materials by single station HVSR (natural scale).
- Determining the spatial extent of the unstable zones and to test the reactivation of landslide in response to rainfall induced stiffness variations in the landslide mass.
- Time-lapse monitoring of prototype experiment by coda wave interferometry for the detection of microfracturing in terms of relative changes in the velocity.
- Seismic velocity's susceptibility to rainfall induced variations in stiffness at natural scale.
- Typological analysis of slidequakes at both natural and prototype experiment by Nanoseismic Monitoring for the possible separation of landslide endogenic from exogenic source mechanisms.

### **1.7 SCOPE**

Recording the seismic signals produced by the slope movement and alteration in the ambient noise wave-field, can provide relevant information on the dynamics of the slidequakes and may

allow the identification of precursors. We have proposed methods for landslide site characterization (geotechnical, geophysical) and dynamical analysis (NM, ANI and HVSR) as new engineering tools. These methods can be linked with other methods for their use in the determination of stress states and the damaged zones identification in tunnel, roads and other engineering structures in addition to landslide.

The use of the geophysical techniques will emerge as a new tool both for the site characterization as well as for the dynamics analysis of landslide. In this way the competitiveness of the engineers will rise. Additionally, it will enhance the ability to detect weak precursor signals in the form of earthquakes and changes in the ambient noise wave fields of a potential failure. However, the specially designed array of the short period seismometers, being portable, easily transferred and the processing in dedicated softwares will provide a visual inspection of the recorded signals in real-time. In the longer-term, applied methodology could also be developed for public hazard monitoring, such as rainfall-induced landslides. Results of this study will prove a milestone in strengthening the landslide early warning systems based on low cost, non-invasive and passive methods.

## **1.8. THESIS OUTLINES**

This thesis will investigate the potential of commonly used geophysical techniques for the analysis of soil landslides. Only landslides in the soil are considered, which are high attenuative of the weak energy associated with the small fractures. Along with their applications at a natural scale landslide, the novel optimizations of the applied techniques at controlled scaled experiments are also included.

This thesis is divided into sections starting from the review and common applications of the adopted methodologies for landslide analysis. The site characterization of Sobradinho landslide is done by geophysical (HVSR, F-K, MASW, ERT). Then the ambient noise characteristics are presented. After this preliminary analysis, the application of time-lapse HVSR and time-lapse noise interferometry and their field scaled novel optimization are given. The last section is based on the typological analysis of the nanoquakes (slidequakes) released after rainfall at Sobradinho landslide and in response to applied stresses at a prototype experiment (pull out test on expander body pile). Finally, all the used methodologies are jointly compared in order to prove the consistency of all findings and then recommendations for the future studies are also provided.

## **2. MATERIAL AND METHODS**

### **2.1. GEOPHYSICAL TECHNIQUES**

#### **2.1.1. AMBIENT NOISE BASED TECHNIQUES**

Ambient noise based (ANb) techniques have been applied for the subsurface structural interpretation as well as for the analysis of mechanical and elastic properties of the landslide mass. The frequency contents and the direction of noise sources are essential. In ambient noise interferometry (ANI) that frequency band is selected which provide maximum coherent energy of the incoming noise wave-field. There are many advantages of using ambient noise for the monitoring purposes, and primarily it excludes the source parameters like focal mechanism and source location. Secondly, it provides a dense and continuous data availability, which leads to high temporal coverage and thirdly its nondestructive (D' HOUR, 2015).

Among ANb techniques, the applications ANI include stress changes with magma migration in the case of active volcanoes (Sens-Schönfelder and Wegler, 2006; Obermann et al., 2013), structural images like in the case of oil and gas (Bakulin et al., 2007), stress changes due to active faults (Wegler and Sens-Schönfelder, 2007; Brenguier et al., 2008), stress level monitoring in gold and silver mining (Gret et al., 2006), deep earth (Boué et al., 2013). In spite of these applications this technique has also been applied to monitor civil and geotechnical structures like buildings (Nakata et al., 2013), landslides (Renalier et al., 2010a) as well as temporal changes in earthen embankments at laboratory-scale experiments (Planès et al., 2016).

Another ANb technique HVSR has been very extensively used in recent times. Comparative to traditional seismological techniques, the HVSR is very easy to apply since it is based on the very short time data acquisition (about 30min) at a single station considering in single short period seismometer. Data processing and interpretations are carried without troubles and the peak observed on HVSR curve is linked with the soil resonance frequency.

Among the geophysical techniques, ANb is advantageous because: (a) seismometers/geophones can be deployed inside as well as outside the landslide borders (b) it can be used as a continuous monitoring method because of the availability of ambient noise sources, (c) it is non-invasive and low-cost tool especially suited for urban areas (d) data can be transmitted in real-time and (e) analyzed automatically by software routines providing information regarding the behavior of the landslide, (f) no active sources such as earthquakes and explosives are necessary. These advantages lead to increase the popularity of ambient noise based techniques during the last

decade (Soler-Llorens et al., 2018). The following section aims at describing the theory and worldwide adaptability of these techniques briefly.

### **2.1.1.1. AMBIENT NOISE INTERFEROMETRY**

Based on the typologies of ambient noise sources, ANI is divided into active and passive category. However, in this study, only passive ANI is discussed which was introduced by Sens-Schönfelder and Wegler, (2006) and was used for the calculation of Green's function. Here the changes in seismic velocities are monitored in a more suitable way (Richter et al., 2014). The Green function/impulse response of the material is calculated by cross-correlation of the ambient noise wave-field that travels between a virtual source and receiver. The traveling ambient noise wave-field presents the elastic state of the material and can be calculated by three mathematical operations, autocorrelation, deconvolution and cross-correlation. The most widely used method is cross-correction which is a proxy for time-lapse changes in the medium. If the medium exhibits a spatially homogeneous relative velocity change  $dV/V$ , the relative travel-time shifts ( $d\tau$ ) between the perturbed and reference Green functions is independent of the lapse time ( $\tau$ ) at which it is measured and  $dV/V = -d\tau / \tau = \text{constant}$  (Hadziioannou et al., 2009).

The processing of ANI is quite variable and is carried out in two stages. A first preliminary stage is called pre-processing and is aiming at balancing the effects of high energy spiky events that can affect ANI results. The pre-processing is adopted from Bensen et al., (2007). However, there are few methodologies in which pre-processing is skipped (Schimmel et al., 2011). The comparisons were made between the Classical Ambient Noise Interferometry (C-ANI) with preprocessing and Phase Stacked Ambient Noise Interferometry (PS-ANI) without preprocessing, and mostly the quality of results found useful even in the absence of preprocessing (Dantas et al., 2018). Despite these conclusions, the pre-processing is still a very commonly adoptive ANI processing workflow.

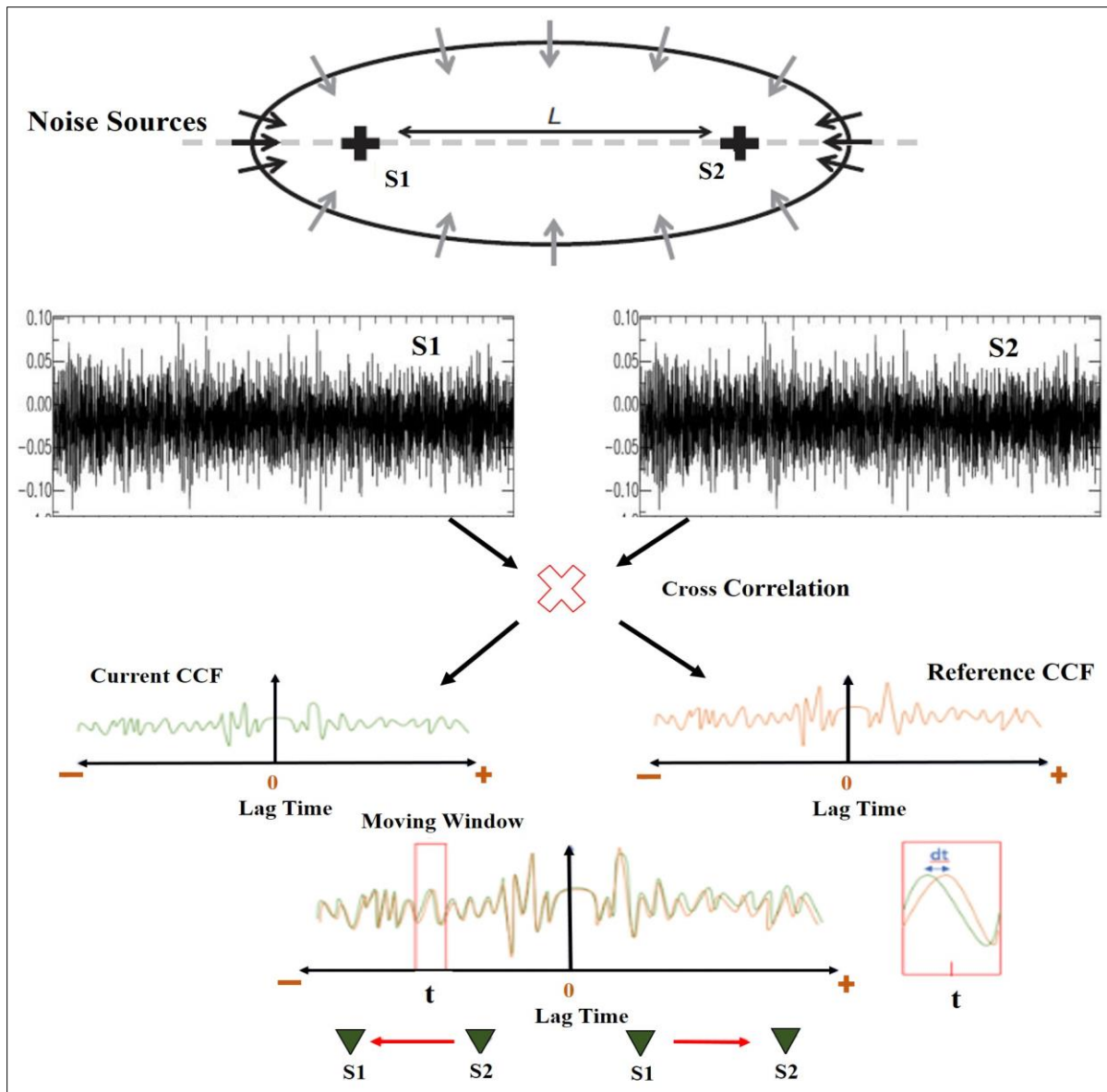


Figure 1 Schematic presentation of ANI with working principle of MWCS technique (Modified after Jonsdottir, 2018)

After pre-processing the ambient noise is gone through one of the flowing mathematical operations to be converted into empirical Green functions. Most commonly used processing schemes are autocorrelation (Wegler and Sens-Schonfelder, 2007), cross-correlation (Hobiger et al., 2014) or deconvolution (Nakata et al., 2013) at a variety of temporal scales (Czarny et al., 2016).

The first application of ANI was based on cross-coherence, but most widely adopted algorithm is cross-correlation (Wapenaar, 2004). A normalized cross-correlation is a coherence, used for determination of stacking velocity of multichannel seismic data. Later a relationship between spatial coherency of the noise field and Green function was found in both frequency and time

domains (Prieto et al., 2009). It was also proposed that earth structure can be extracted from ambient noise wave-field based on its spatial coherency. Later in 2011, the Green function between stations pairs was constructed by cross-coherence of the recorded ambient noise wave-field.

In ANI cross-correlation is an operation that provides the travel-times of seismic phases between two sensors. The signals recorded represent the same wave-field shifted in time that it takes to reach from one sensor to the second. Therefore, the cross-correlation function contains a peak which corresponding to the travel-time of wave-field between the sensors.

The cross-correlation operation measures the wave similarity at different locations using travel-time lag ( $\tau$ ) between the sensors. The cross-correlation of two signals S1 and S2,  $CC_{S1, S2}$ , is a function of time lag, and is commonly defined as:

$$CC_{S1, S2}(\tau) = \int A(t, S1)A(t - \tau, S2)dt \quad (1)$$

Where integration is performed over the length of the records, and A is the amplitude of a signal as a function of time. From equation (1),  $CC(S1, S2)$  is maximum when the sum of the products,  $u(t, S1) \times u(t-\tau, S2)$  is at a maximum, meaning that S1 and S2 are most similar when S2 is shifted by that amount relative to S1.

Cross-correlation of all the station pairs is computed usually at daily time step. The pattern of correlation is complex under non-ideal conditions which is the case with the experiment in natural world where the ambient noise wave-field is not truly diffuse. The cross-correlation does not represent symmetric surface waves at opposite time shifts correspond to intra-station surface waves come out of two sensors. The isolated wave packets are observed over a geographically small areas having no multipathing, under these conditions these packets correspond to the distance between the stations divided by the average velocity. However, under natural conditions, a wide range of such wave packets are observed over the cross-correlograms having a non-symmetric time shifts (Sgattoni et al., 2017).

The autocorrelation (performed at one station) is a particular case of cross-correlation where a signal is correlated with itself (D'HOOR, 2015). It is one of the earlier technique of extracting time-lapse changes. In this technique, a wave is recorded that moves from one sensor to another sensor (as happen in cross-correlation) and then come back again to the first sensor.

Autocorrelation has suffered from a limitation based on the ambiguity of the types of waves. It is not clear whether these waves are surface or body.

In deconvolution interferometry, the impulse response can be extracted independently of structural coupling and the complicated wave propagation (e.g. attenuation and scattering) below the sensor (Snieder & Şafak, 2006). According to Nakata & Snieder, (2014), this is a useful technique for the extraction of impulse response of one dimensional structures like buildings, the details can be found at (Nakata et al., 2013). Monitoring of these structures by deconvolution interferometry changes the boundary conditions at the base, so an impulse response is constructed independently of coupling and the soil properties (Snieder & Şafak, 2006). It is done based on the removal of source signals from the record by spectral division, the mathematical explanation is provided by de Vasconcelos and Snieder, (2008). The other empirical example of real ambient noise data can be found in studies carried out by de Vasconcelos & Snieder, (2008).

All methods mentioned above for the impulse response construction based on ambient noise interferometry have their own merits and demerits and their applications are dependent on the quality of data (Nakata et al., 2011) and the study objectives.

#### **2.1.1.2. HORIZONTAL TO VERTICAL SPECTRAL RATIO**

Among ANb the HVSR technique has been gaining popularity in landslide hazard assessment and vulnerability to different triggering factors like earthquakes and rainfalls. It offers a logistically efficient and cost-effective method to map landslide and its dynamics. It provides information about the resonance behaviors of lithomorphologies and geomorphological features as well (Galea et al., 2014).

The single station HVSR technique is based on very simple ambient noise processing steps. In the first step, after the application of bandpass filters in order to remove the effects of transients, the Fourier spectra of north-south, east-west and vertical components are calculated. In the second step, spectra of both horizontal components are averaged (contains Rayleigh and Love waves) and are divided by the spectrum of vertical component, that results in a HVSR curve as a function of frequency. This curve provides a peak that is related to the resonance of the subsoil stratigraphy and in particular to stiffness contrast between soft deposits and their bedrock.

The shape of HVSR can be explained based on different viewpoints. In one viewpoint HVSR peak is linked with the ellipticity of Rayleigh waves around the fundamental frequency of the site provided that there exists a sharp impedance contrast between the soil and bedrock (Bard, 1999). This viewpoint is based on the Rayleigh wave dominance of ambient noise, however other authors claimed for the dominance of body waves around the peak of the H/V (Bonney-Claudet et al., 2008). The HVSR ratio peak is also considered to be related with the transfer function of vertically polarized SH waves (Nakamura, 1989) or the S wave amplification. However, based on the diffuse wave-field assumption, where the microtremor is treated as a diffuse field, containing both surface (Love and Rayleigh) and body (P and S) waves (Sánchez-Sesma et al., 2011). The ambient noise wave-field is the outcome of random uncorrelated forces or sources present near the earth surface, which contains scattering effects of different elastic modes, so it can be better explained by considering it as a diffuse field. Here it is assumed at a given point in the given direction, the given component of the average autocorrelation of motion is proportional to Directional Energy Density (DED). DED is proportional to the imaginary part of the Green function if source and receiver lie at the same point. The peak of HVSR is explained in terms of DED as opposed to the traditionally held assumption where it is linked with Rayleigh wave ellipticity. This assumption of a diffuse field will provide deep insight into HVSR and is explained as a square root of the imaginary part of the Green function of each component. The mathematical explanation can be found at Sanchez-Sesma et al. (2011).

The successful application of HVSR technique is conditioned by the presence of strong impedance contrast in the subsurface (Delgado et al., 2015; Martino et al., 2016). However, under the rainfall-induced saturation in the case of clayey landslide reduces the impedance contrast. This happens because of the changes in rheology of the upper unconsolidated material. It is the base for the application of HVSR for the analysis of seasonal dynamics of rainfall triggered landslide.

Statistical tests have been carried out to check the reliability criteria of peak and curve clarity (SESAME, guidelines, 2005). The measurements have not met the reliability criteria (i.e. presence of a clear peak with sufficiently large amplitude) are usually removed from the analysis. The correct HVSR peak identification which represents the shear wave resonance frequency of the site (soil-bedrock contrast), is a paramount step in this technique. The peak identification is very straightforward for the higher subsurface contrast. However, the ambiguities rise in the case where there exist two velocity contrasts and depth-dependent rise

in shear wave velocity, under these conditions the HVSR curve represents two peaks and correct peak identification become challenging.

Landslide affected areas show the directional effect as demonstrated in many past studies (Burjánek et al., 2010; Del Gaudio and Wasowski, 2011; Imposa et al., 2017; Iannucci et al., 2018). In the directional analysis, the horizontal components of the ambient noise records are rotated from 0 and up to 180° by 10° in each step and computed the HVSR for each pair of azimuth. The contour maps of the HVSR as a function of the frequency and rotation angle are plotted. In this way, results are produced because of the path effects of geomorphological features of the area and not because of the non-stationarity of the noise sources. Hence the spatiotemporal variabilities of noise sources in the area can be tested easily. Surface wave polarization can be used to zone landslide prone areas in the framework of risk management studies (Panzerà et al., 2012; Galea et al., 2014; Iannucci et al., 2017; 2018).

#### **2.1.1.3. MULTI-CHANNEL ANALYSIS OF SURFACE WAVE**

The surface waves are dispersive, this means that different frequencies behave differently while passing through a layered subsurface each constitutes a distinct impedance contrast. This property of surface waves is used for the subsurface site characterization (such as stratigraphy, shear velocity, and depth to bedrock). Different methods utilize this characteristic of the surface waves. However, the Multi-channel Analysis of Surface Waves (MASW) is proved advantageous over other geophysical methods in the determination of soil stiffness, especially in a case where subsurface characterization is required over undisturbed conditions and coarse grain material like gravels, as is the case with landslide affected areas.

The f-k analysis applied to active seismic data is also known as MASW (Park et al., 1999). The data acquisition systems are used as applied in traditional seismic refraction and reflection surveying. It is of two types based on the source of energy use as active and passive. In active MASW and a wide range of frequencies are produced by changing the weight of impulsive source (hammer) used, the light weight hammer produces higher frequencies compared to heavier one that usually generates low frequencies. Then dispersion curve (wavelength vs phase velocity) are generated from the delays in different phases of different wave field frequencies at the receiver array (Park et al., 1999). The MASW analysis includes surface waves, body waves, reflected waves, and higher order harmonics (Lontsi et al., 2016). In the final stage, the dispersion curve is inverted to obtain the shear wave velocity profile of the subsurface.

## 2.2. SEISMIC EMISSION BASED APPROACHES

Previous studies have experimentally proved the presence of the brittle failure in the rainfall-triggered clay-rich landslide contradictory to the commonly held assumption of the absence of brittle material doesn't support microseismic emission (Walter et al., 2009; 2012; 2013; 2015).

The signals produced by the landslide are of low magnitude and they are quickly attenuated by the soil heterogeneous conditions, a variable degree of saturation and surface deformation at the landslide. Usually, the attenuation patterns of the landslide are checked with the hammer blows. Only those signals are considered that show a consistent and prominent pattern of maximum amplitude attenuation cross the seismic network (Vouillamoz et al., 2018) such signals are linked with the dynamism of landslide and some author called them "slidequakes" (Walter et al., 2012).

The emergence of slidequakes has been observed in many previous studies. The signals that were of earthquake type having short-duration and were found discernable, traceable wave packets were observed by Gomberg et al. (1995) and Gomberg et al. (2011). The 5-sec long earthquake like signals having a frequency in the range of 10-80 were reported by Walter et al. (2013) and these signals were referred to as slidequakes. The short-duration about 1 sec and 10 Hz frequency quakes signals were analyzed by Tonnellier et al. (2013) and Provost et al. (2017). These signals did not show a distinguishable P and S waves onsets so the time picking is based on the traditional seismological analysis is not applicable under these scenarios. As is the case with the tremors recorded at Super-Sauze and Valoria landslides (Walter et al., 2013; Tonnellier et al., 2013; Provost et al., 2017). At Super-Sauze tremor, signals were related with the surface deformations recorded with the extensometers. The authors also observed signals produced by the scratching and grinding of landslide material (Walter et al., 2012). Fiorucci et al. (2016) detected and characterized blasts from a quarry district in Central Italy and recognized rock failures originated from different quarry walls, which occurred after the blasts. A scheme for the classification the microseismic signals emitted from the landslide was revamped after the work of Vouillamoz et al. (2018) where the following signals attributes were used in the analysis.

The apparent velocity of signals is used for their classification. Sometimes the signals emerge in the form of multiple jolts and energetic spikes and sometimes they appear as separate individual signals; these features are important in the analysis of the signal typology. The signal duration is an important attribute used for the typological analysis. According to Vouillamoz et

al. (2018), it can be distinguished into different categories based the duration as short-duration (< 2 s), medium duration (2–20 s) and long-duration (> 20 s –minutes) signals. The frequency patterns of signals recorded by arrays is another important attribute and is determined from the signal spectrograms and amplitude spectrum at selected bandpass filters. The other important signals attributes include harmonic peaks, dispersive, gliding or multiple-band dominant frequencies (Vouillamoz et al., 2018). These above mentioned attributes were used as benchmarks in the clarification of microseismic signals (Gomberg et al., 1995; Walter and Joswig, 2008, 2009; Gomberg et al., 2011; Lenti et al., 2012; Walter et al., 2012; Tonnellier et al., 2013; Fiorucci et al., 2017; Provost et al., 2017; Vouillamoz et al., 2018).

The typological classification of seismic signals divided into three groups as Earthquakes (local, regional and teleseisms), Quakes (source–receiver distance < 50–500 m) and Tremors (landslide-induced tremor signals and external sources of tremor-like radiations). There is absence of any unequivocal classification of the tremor like signals because of the presence of wide range of dominant frequencies and waveform intricacy and its attenuation pattern that is dependent on the size and the distance of rockfall event from the recording array which can be observed from the remote sensing of the landslide surface. The tremor like (<20s) signals are distinguished from tremor like radiation (minute long) signal based on the duration of the signal. The waveform and spectrograms of dispersive tremors vary a lot from one station to another because of the dispersive nature of the signal makes its detection tough (Vouillamoz et al., 2018).

### **2.2.1. NANOSEISMIC MONITORING**

Nanoseismic Monitoring (NM) is a field of passive seismic, constitute of specialized acquisition and processing methods for the detection and localization of weak energy signals ( $M_L < 1$ ) usually less than background noise levels (Wust-Bloch & Joswig, 2006; Wust-Bloch, 2009; Walter et al., 2011; Wust-Bloch & Tsesarsky, 2013; Joswig, 1990; 1995). The robustness against noise levels and autonomy in event detection are the two aspects of this technique that took it to new highs of unprecedented sensitivity. The essence of autonomy lies in the application of SNS because it can be achieved on the principle that event of weak magnitude can be detected at nearest station only. And the second pillar of NM i.e. robustness against noise is achieved in signal processing where a detected software 'HypoLine' reduces the signal detection below 0 decibel (dB). The rapid system setup, together with its ultra-portability turns the SNS into a truly optimal aftershock monitoring system (Joswig, 2008).

### 2.2.1.1. MINI-ARRAY

The use of sensors arrays can be traced back in 1960s. In comparison to single stations array has many advantages that are useful in engineering applications. Each mini array, consists of one three-component and three vertical one components seismometers installed at an appropriate angle ( $120^{\circ}$ ) (Figure 2). The aperture size is a function of slant distance (source-receiver distance) which is usually kept in the range of 50-200m (Joswig, 2008). The aperture is very crucial component of this system because it will only resolve those events at certain aperture distance. Because the target signals in NM are characterize by high frequency contents so the choice of the sensors is usually short period/broad band seismometers both one components and three components together with high sampling rate and continuous data loggers.

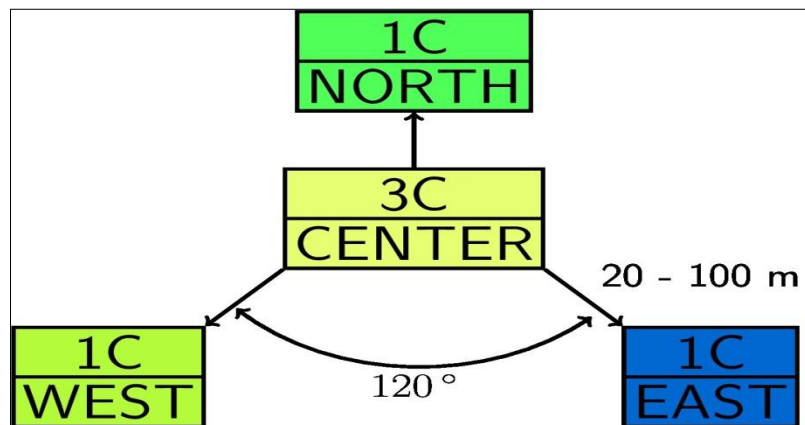


Figure 2 Data acquisition with SNS (Sick et al., 2014)

The importance of seismic arrays in the detection of events cannot be neglected from local to teleseismic scales. Their operations are similar to phased arrays used in radar acquisition and were applied first time to seismic problem in 1960s (Rost & Thomas, 2002). The maximum phase coherence among all stations is achieved by utilization the concept that plane waves travel along the array aperture. The SNR is improved by utilizing the sum and delay concepts commonly referred to as beamforming, where SNR is proportional to the square root of number of stations used. In turn array gives only one location by using many stations. The three-component stations provide backazimuths from station to event and are constrained in the direction of tS-tP that gives distance in this way the events are localized (Joswig, 2008).

### **2.2.1.2. DATA PROCESSING**

In the absence of a priori velocity model, the signal processing in NM is of a constant loop type which rests on trial and error approach. Both array and network analysis were introduced to find the influence of single trace onto location space. The signal energy is displayed in time-frequency domain and in slowness space. The error bars are accessed by jackknifing through hundreds of options in parameter space in a virtual reality manner. In NM the nano events having ML -2.0 are obtained from cross-correlation of captured earthquake events (Joswig & Schulte-Thesis, 1993).

Data processing in NM has following important steps. Data is processed using a software package NanoseismicSuite (Sick et al., 2014).

### **2.2.1.3. SONOGRAMS AND SUPERSONOGRAMS**

The sonogram is a graph, where the vertical axis is the logarithm of the frequency and the horizontal axis is the time. This graph allows the user to view the energy density as a function time-frequency (Joswig, 1990). The sonogram calculation is done in four processing steps as; 1) Power Spectral Density Matrix (PDM) estimation, 2) the energy binned at 13th half octave wide bandpass and results are being transformed to a logarithmic scale. 3) In this step a noise adaptation Stive filter is applied, the advantage of applying this filter is that it rates the fracturation of energy which can help in differentiation of potential signals from the background noise. 4) In the last step, the influence of noisy pikes are reduced by prewhitening, in this way disturbances in the signal visualization are minimized (Joswig, 1990, 1995; Sick et al., 2014; Vouillamoz, 2015). A typical sonogram is shown in Figure 3 and Supersonogram in Figure 4. The spectral whitening equalizes the spectrum of the signal by enhancing low level spectral components and attenuating high level, making it similar to the white noise spectrum (spectral amplitude equal to one). Here the aim is to remove the influence of signals which manifest in amplitude spectra such as frequency-localized noise sources. Thus, knowing the characteristics spectral content of some types of noise or events of interest, we can identify them (Joswig, 2006).

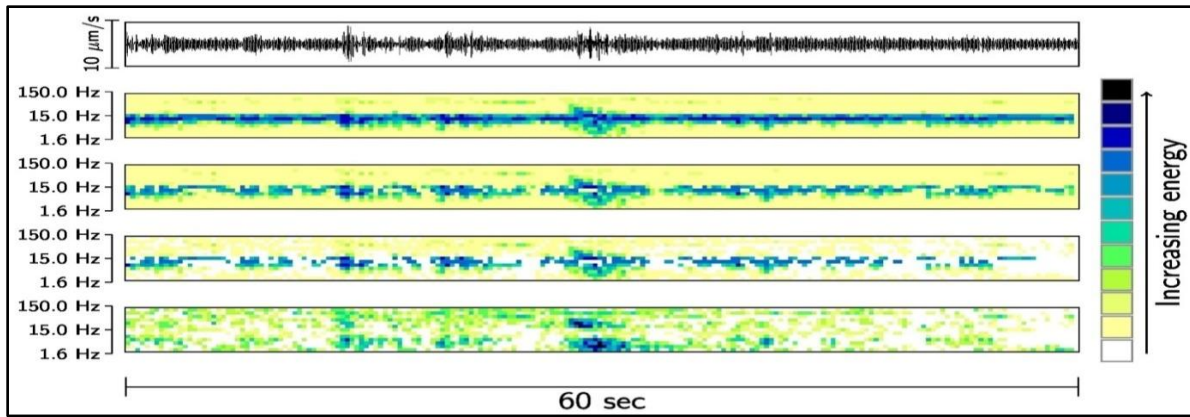


Figure 3 An example of Sonogram (Sick et al., 2014)

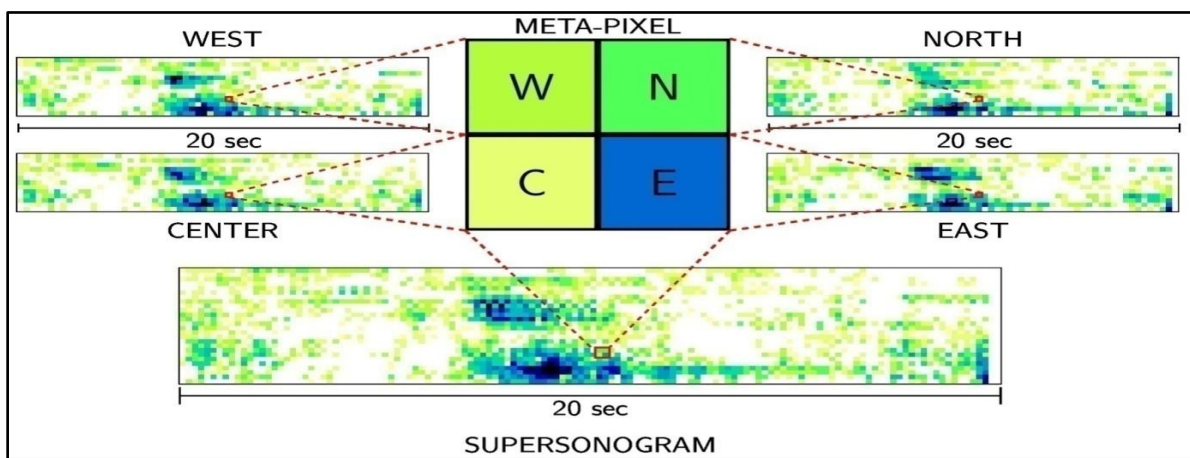


Figure 4 A presentation of supersonogram (Sick et al., 2014)

#### 2.2.1.4. HYPOLINE AND JACKKNIFING

Here the contribution of each individual phase in event location are displayed as hypolines (constraining curves in event location or hyperbola of  $t_p - t_p$  of any two stations or circle of  $t_S - t_P$  of any single station, it can be an array beam) and are determined by HypoLine program. The highest concentration of these hypolines in solution space is the best event location. These hyperbolae are best suited for half space solution models and with zero depth. Increase in depth will leave a cut on the surface (hyperboloid), which become hyperbola when this cut (hyperboloid) become parallel to the axis of symmetry. The ability of Hypolines in event localization depends on the handling and displaying the uncertainties. Like other classical approaches it also considers area of hypolines crossing like classical approach (matrix inversion), but unlike classical approach, its values are determined by jackknifing (Joswig, 2006).

For the location of discrete events, the hypocenter related information is broken down into small graphical location constraints, which help in location of small events in a joint, average

erroneous space. This form of outliers-resistant statistics is referred to as Jackknifing and it has a central role in the identification of nano events (Joswig, 2008). This scheme is a variation of the most common, "leave one out" jackknife where  $N$  observations are subdivided into  $N$  samples of size  $N-1$ . Here we perform a "leave out  $k$ " operation with  $N-k$  being the dimension of the statistics, i.e., matching the number of parameters to be determined (Table 1) (Joswig, 2006; 2008).

The concept of HypoLine, that is present in SonoSuit, is the distinction of NM over other methods. The iterative nature of this program allowed a real time monitoring. A single pick in the event space can change the obtained results like hypocenter, time of origin of the event and magnitude. The same iterative scheme can be applied to intrinsic parameters, such as velocities and thicknesses of the layers or magnitude-distance correction. The purpose is to test the possible combinations among the different phases for the same event, due to the low SNR, with the intrinsic parameters for the solution and arrive at a plausible solution (Joswig, 2008).

#### **2.2.1.5. NANOSEISMICSUITE**

There are two main module HypoLine and SonoView, of the NanoseismicSuite software ([www.nanoseismic.net](http://www.nanoseismic.net)), developed by the Institute of Geophysics of the Stuttgart University. SonoView helps in screening the recorded data by the super-sonogram operator, i.e. a specific spectrogram with noise adaptation, muting and pre-whitening function and a special color palette that facilitates visual detection of seismic events (Sick et al., 2015).

In this Java based user interface all the processing steps of the NM can be performed easily. This software uses a graphical approach. Phases are determined iteratively and results are updated in real time in the solution space. Locations are computed with a combination of array and network processing with the following information: P arrival times,  $t_S-t_P$  time differences from the two central 3C's as well as array beams from the two mini-arrays. P and S onsets are determined interactively. Event detection is carried out with sonograms (Joswig 1990, 1995) which enhances the display of signal energy close to the noise threshold by auto-adaptive, non-linear filtering.

#### **2.2.1.6. SIGNAL NOMENCLATURE**

The frequency contents, duration and amplitude are the three basic attributes on which entire nomenclature of nano signals is based. The attenuative characteristics of the site that affect these

attributes have an important role in signal classifications (Walter et al., 2012). In Figure 5 collapse and failure signals are shown, it is clear that collapse and failure signals can be identified by sonogram screening.

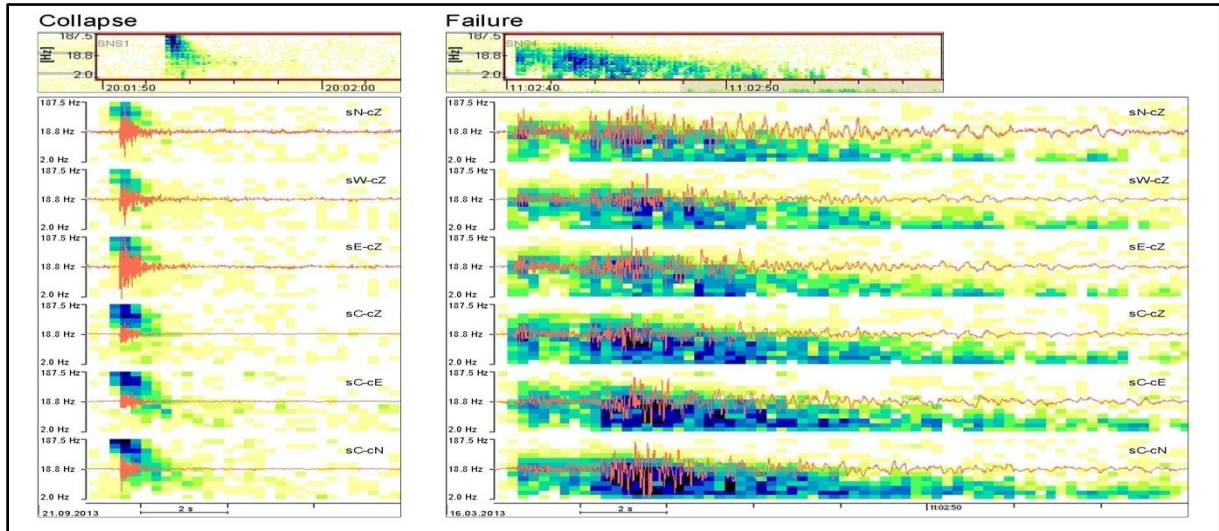


Figure 5 Sonogram with waveform of collapse and failure events (Fiorucci et al., 2017).

### 2.2.1.7 EVENT LOCATION

Events are localized in HypoLine by network and array processing (Joswig, 2006). In array processing backazimuth is calculated while in network tS -tP spheres and tP-tP hyperboloids of mini-array are determined where the accuracy of event location is dependent on the number of stations used and it can be optimized using hyperboloids of three small arrays (Häge & Joswig 2009). Event localization can be explained as an absolute location of homogeneous half space and a relative event as described below.

#### 2.2.1.7.1 ABSOLUTE LOCATION

This event localization can be exemplified by considering a homogeneous half space below the surface where the sensors lie. The required information is derived from the time difference ( $t_{p1} - t_{p2}$ ) of the P wave arrivals at two different sensors, result is a semi-hyperboloid which is converted to a hyperbola on intersection with a plane parallel to the surface at depth as shown in Figure 6a. Imagine a seismic source S and two sensors S1 and S2 on the surface of earth. If  $t_1$  is the time taken by the wave emitted at S to reach sensor S1 and  $t_2$  is the time taken by wave from S2 to reach second sensor S1, then the distance between two sources can be determined by Equation (2). In Equation (2) an infinite combination of FS1 and FS2 is used which results

in the constant  $\Delta t \cdot v$  ( $v$  is the propagation velocity of the wave). The equation (2) is a mathematical presentation of a case where two receivers lie at the foci of hyperbolae as shown in Figure 6.

$$F1S1 - FS2 = \Delta t \cdot v \quad (2)$$

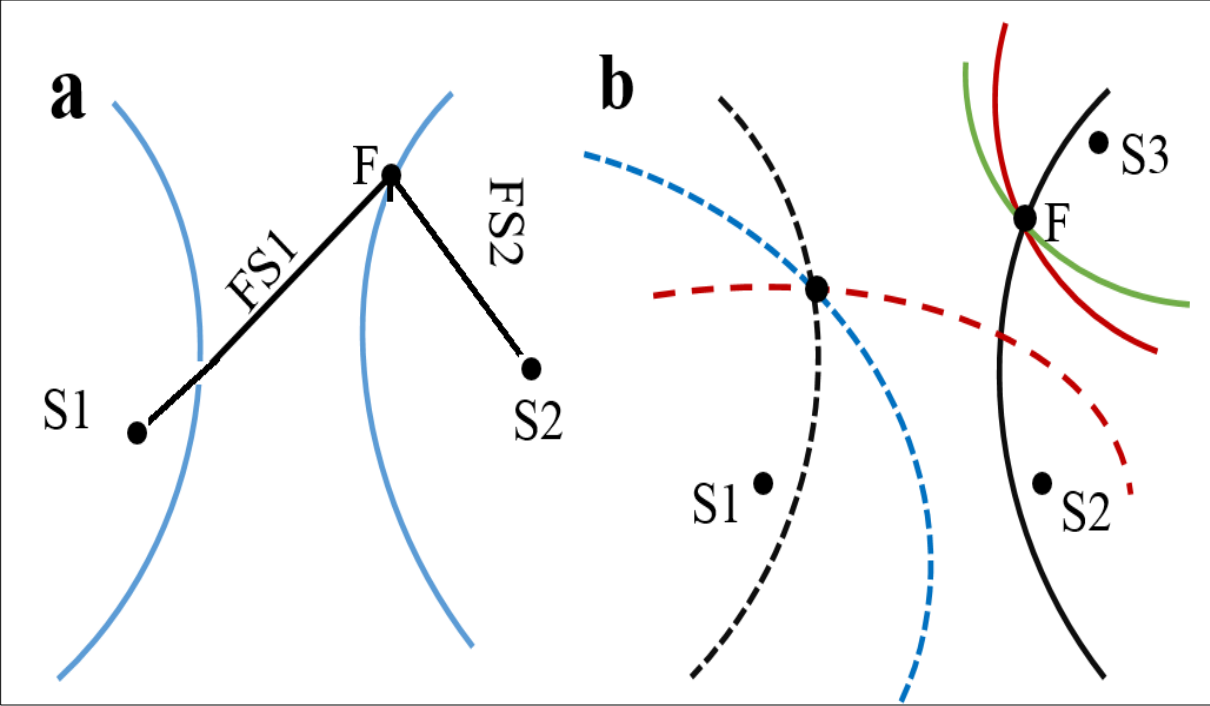


Figure 6 (a) Hyperbolae with two sensors at the foci and a signal solution (source location). (b) Intersection of three hyperbolae obtained from the distance of source and sensors. Dotted and solid lines are the initial and final solutions, respectively (Modified after Silva, 2010).

Three sensors S1, S2, S3 are shown for the source location. Their hyperbolae intersect twice which are represented by dotted and solid lines as initial and final solutions, respectively (Figure 6). The arrival times of P-waves decide the fate of hyperbolae for the solution (contentious lines or dotted lines). Then, for a solution in space 3-D ( $x, y, z$ ),  $x$  and  $y$  are the epicenters and  $z$  is the hypocenter, with only two receivers which leads to more unknowns and result will be underdetermined system (Figure 6). The hyperbolae intersection points are determined by the difference in distance between source and receiver. At the beginning, there are two points of intersections (dotted lines) but later depending on the time sequence in which wave strike the receivers there will be a single intersection (solid lines). Hence proved that we need at least three receivers that all intersect at a single point which is called as triple point and it's the solution.

Now let us consider a case where we have four sensors for the acquisition, here four intersection points are found  $P_1 = f(t_1, t_2, t_3)$ ,  $P_2 = f(t_1, t_2, t_4)$ ,  $P_3 = f(t_1, t_3, t_4)$  and  $P_4 = f(t_2, t_3, t_4)$ . There are four respective solutions in this case. Four triple points are visualized in HypoLine that creates a spread based on the phases then the hypocenter is localized.

$$P = f(t_1, t_2, t_3) \quad (3)$$

Hyperboloids are calculated by  $t_P - t_P$  of different stations, whereby  $t_1, t_2$  and  $t_3$  are P onsets at S1, S2 and S3, respectively. For instance, hyperboloid  $t_{13}$  for stations S1 and S3 is calculated by  $t_{13} = t_1 - t_3$  (Häge & Jowsig 2009). Generally, the number of hyperbolae H is given by Equation (4), where N is the number of sensors and k is an integer ranging from 1 to N-1. The number of triple points T (solutions) is given by Equation (5), Table 1 shows the triple point number (T) and (H) as a function of the number of sensors (N) used (Joswig, 2008).

$$H = \sum_{K=1}^{N-1} K = \frac{N!}{(N-2)! 2!} \quad (4)$$

$$T = \sum_{K=1}^{N-2} K(N-1-k) = \frac{N!}{(N-3)! 3!} \quad (5)$$

Table 1 Number of hyperbolae and triple points as a function of the number of receivers (Joswig, 2008)

N	3	4	5	6	7	8	9	10	11	12
H	3	6	10	15	21	28	36	45	55	66
T	1	4	10	20	35	56	81	120	165	220

Angle of incident of the wave with sensor is another information obtained from the analysis. In HypoLine this can be obtained either by triaxial receiver or by beam-forming analysis (Joswig, 2006). In the first case, the vector information is derived by the wave recorded at three directions. The second method is based on the time difference of same wave recorded at two receivers. Consider a plane wavefront in two dimensions where  $t_1$  and  $t_2$  are the times when this wave reaches the sensors S1 and S2, respectively. The distance of wavefront is  $v \cdot \Delta t$  where,  $\Delta t = t_2 - t_1$ . The propagation velocity is equal to true velocity only in the direction where sensors align (Figure 7b), in all other directions its value is smaller (apparent velocity) as shown

in Figure 7. This particular direction is the direction of event. As the distance between sensors is small (max. 100m) in NM, therefore the waves emitted are considered as flat (Figure 7). This assumption is used in beamforming method. In the case where wavefront is traveling in all directions, the recorded velocity will be apparent velocity and is determined by Equation (6) it can also be written as Equation (7) in terms of slowness. Where ‘ $\alpha$ ’ is the propagation velocity of the wave and ‘ $i$ ’ the angle of incidence of the wave with sensor. In this way all the information required for the NM event analysis is done.

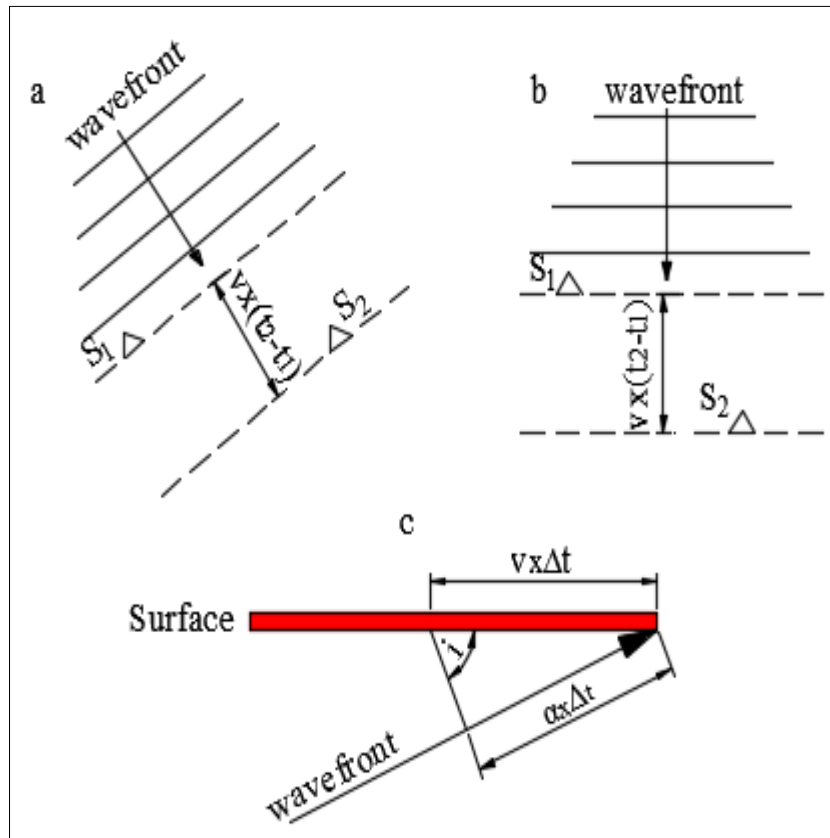


Figure 7 (a) Wavefront incident on sensor S1 at time t1, after a time  $\Delta t = t_2 - t_1$  on sensor S2 at angle. (b) Here wavefront incident perpendicularly. (c) Velocity wavefront  $\alpha$  incident on the earth's surface at an angle  $i$ .

$$v = \frac{\alpha}{\sin i} \quad (6)$$

$$v = \frac{1}{p} \quad (7)$$

### 2.2.1.7.2. RELATIVE LOCATION

Relative location is the location of an event from the main event with least location error. It works only if the distance between sensors will be less than the distance of an event from sensor. The events are so located have greater accuracy which here depends on a situation where time residue at the middle is because of variation in propagation velocities of P and S waves. This time difference is calculated and then the locations of other events are corrected by using obtained information and it is done manually by the observer in HypoLine. It can be elaborated by considering a simple case where we have only three stations (Figure 8) this simple approximation will facilitate the understanding. The location obtained by intersection of tS–tP spheres and hyperboloids (tS–tP circles and hyperbolae in 2-D space) is considered as an absolute. Green ‘×’ marks the hypocenter. Using the location method (intersections of hyperbolae) for each pair of sensors (S1-S2, S1-S3 and S2-S3), the difference of arrival time of the P wave of the secondary event, relative to the main event is calculated by using Equation (8).

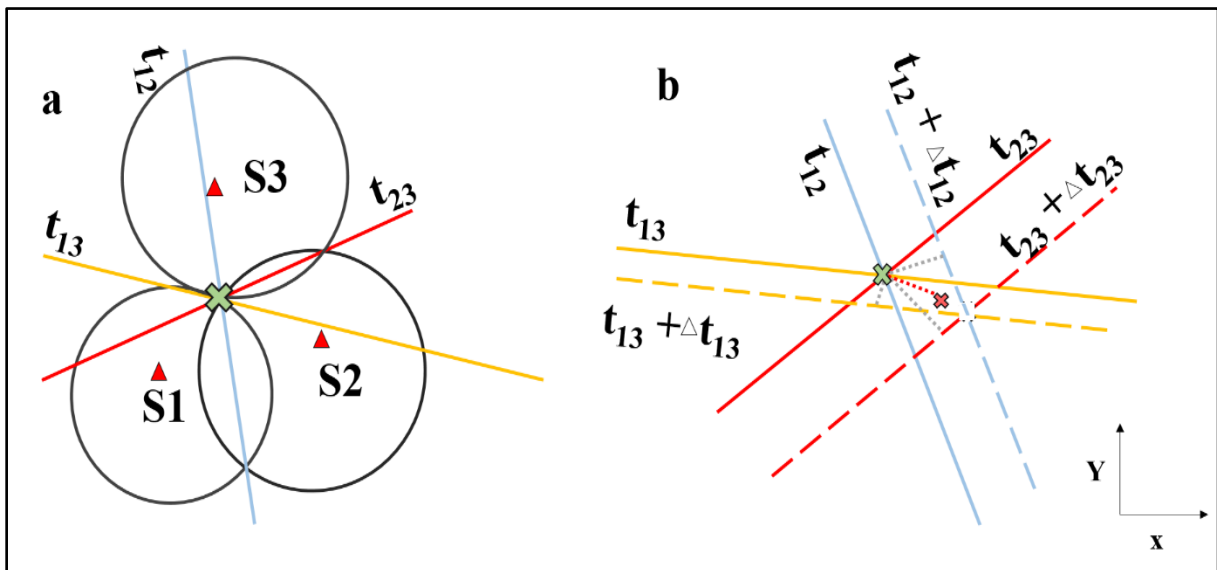


Figure 8 Principle procedure of event location with network processing including data from three stations. Sketch in (a) shows the intersection of a horizontal plane at depth. Sketch in (b) is a zoom window of (a) (Häge & Joswig, 2009).

$$\Delta tE12(\text{relative}) = \Delta tM12 + \Delta tM12 - \Delta tE12(\text{absolute})$$

$$\Delta tE13(\text{relative}) = \Delta tM13 + \Delta tM13 - \Delta tE13(\text{absolute})$$

$$\Delta tE23(\text{relative}) = \Delta tM23 + \Delta tM23 - \Delta tE23(\text{absolute})(8)$$

Where, ‘E’ and ‘M’ are main and secondary events, respectively.

#### **2.2.1.8. MAGNITUDE**

Magnitude of an event in NM is determined by the Wood-Anderson simulation (Häge & Joswig, 2009). The maximum and minimum amplitude values of the recorded waveforms can be determined easily. The magnitude values are shown as magnitude-distance correction curves and is calculated by Equation (9), where A refers to the maximum amplitude, at the station site, and R is the attenuation factor of the signal that travels from the source to the receiver. This magnitude distance corrections were proposed by Joswig (2006) and used in the Hypoline program.

$$M = \log(A) + \log(R) \quad (9)$$

#### **2.2.1.9 LIMITATIONS**

Although Nanoseismic Monitoring (NM) is a new very promising technique, this technique has different limitations that should be considered before its implementation. In the case of the location of events, it is not possible to get an error associated with this location due to the fact that the procedure is based on a geometric formulation. This requires implementing a code that considers at least one model of small-scale velocities. It is also required that the characterization of the seismic source, that is, to obtain the tensor moment to determine the orientation of the fractures. The future studies will prove these assumptions.

The application of the technique of NM is also limited by the level of background noise. Special care must be taken when the experiments are conducted in urban areas or when there is an intense industrial activity, as is the case of the mining areas (Fiorucci et al., 2016).

It is necessary to perform different experiments for different subsurface conditions, due to the fact that the environmental intrinsic attenuation can affect the results, both in the time domain and the frequency domain. For example, in the case of saturated clays with high coefficients of Poisson, the seismic signals are attenuated in high frequencies, and it would be difficult to obtain well-defined arrival times. Similarly, in media with high speeds may be difficult to identify the phase differences between the primary and secondary arrivals.

## **2.3. OTHER GEOPHYSICAL TECHNIQUES**

### **2.3.1. ELECTRICAL RESISTIVITY METHOD**

The electrical resistivity method is one of the most adopted geophysical methods in near surface investigations. It is based on measuring the electrical potentials between one electrode pair while transmitting a direct current between another electrode pair. Geoelectrical data are commonly expressed as apparent resistivities (Equation 10)

$$\rho_a = KI/\Delta V \quad (10),$$

where ‘ $\Delta V$ ’ is the measured potential, ‘ $I$ ’ the transmitted current, and ‘ $K$ ’ the geometrical factor. Electrical resistivity survey can be carried out in an area by three possible ways based of the arrangement of electrodes: 1) a scheme where the electrodes are moved from mid-point is known as vertical electrical sounding (VES) 2) another approach where entire array of electrodes is moved with a constant electrode space is called profiling. The electrical resistivity tomography (ERT) or electrical resistivity imaging, here a large number of electrodes in combination of pairs are used as a circuit where ground acts as a resistor for the subsurface imaging. In these techniques, VES is considered to be an attractive choice especially, in situations where the target is 1-D variations such is the case with groundwater studies. However, the 1-D assumption inhibits its use for the analysis where 2-D variations, lateral as well as vertical in the subsurface are expected as the case of the occurrence of landslide. The choice of an appropriate electrodes array is based on target depth, lateral resolution and level of noise in the area (Jongmans & Garambois, 2007). Wubda et al. (2017) provided a detailed review of electrical resistivity method.

### **2.3.2. GROUND PENETRATION RADAR**

Ground Penetration Radar (GPR) is a geophysical technique in which subsurface image is obtained by passing electromagnetic waves of various frequencies through the earth. These energies are radiated from the antenna, which either absorbed or reflected back form the underlying material properties like fractures, moistures and clay contents. The energy reflected by the surface discontinuities is received by the receiver, which helps in subsurface image construction. The amplitude of radar pulse is an important attribute because it can carry information about the ground. After time to depth conversion these amplitudes help in mapping

the subsurface discontinuities (both physical and chemical). Higher the contrast at the interface of these discontinuities higher the amplitudes and vice versa. Detailed description of the theory and application for landslide can found in the works of Su et al. (2017) and Singh et al. (2018).

### **2.3.3. GEODETIC MONITORING**

Digital photogrammetry, which is dependent on triangulation, is of three types based on the techniques used for the image acquisition as Unmanned Ariel Vehicle (UAV), Short Range and Satellite. Photos of the same scene taken at different angles called rays, are mathematically converted into three-dimensional coordinates used in the analysis. From these photos high resolution digital elevation models (DEM) are constructed. These DEMs taken at different time scales are compared, in this way, the onset and growth of fissures and cracks on the surface of deforming slope are observed (Rothmund et al., 2017). The commonly adopted processing steps are 1) key features identification; 2) their matches in different photos; 3) camera pose identification; 4) point cloud generation and its densification and 5) orthomosaic/DEM generation.

The UAV-based remote sensing is not new and had been applied to many studies in the past. The developments in the field of Red Green Blue (RGB) cameras and UAV vehicles have made these applications more attractive (Menegoni et al., 2018). The first high resolution DEM were generated from photos taken by a helicopter in 2005. The most adopted UAV systems (vehicles, motorized paragliders balloons, kites, and blimps) are suffered from the influence of air currents and restrict their usages over high elevated areas such as alpines. So quad-rotor systems appeared as an alternative better option (Niethammer et al., 2010). UAV based methodology is mainly composed of two phases: the first one is the UAV mission planning and execution, while the latter is the image processing. There are two types of error associated with the drone survey quantitative and qualitative. For earth-slides the more attention is paid to the qualitative error which is usually checked by comparing the dimensions of ground truth mark and its dimension on the drone photographs. In order to minimize these errors and to avoid partial overlapping of images, proper planning of photogrammetry survey is required. The survey planning can be executed in available software by providing following information relevant to flight as altitude Above Ground Level (AGL), the photo camera parameters (CCD size, focal length, size pixel, etc.), output parameters of the orthophoto (ground resolution, GSD-Ground Sampling Distance). Along with theses parameters a georeferenced image (Google Earth™) of the study area is also used in mission planning. Based on the provided information the software will mark the way

points on this image through which UAV must pass during flight (Torrero et al., 2015). After data acquisition all the images are processed by using photogrammetric softwares. Starting from structure from motion algorithm, which as a result it provides camera parameters relative to 3-D locations in the images provided as an input. Then a dense point cloud is generated. Then from the time-lapse orthophotographs Digital Terrain Models (DTM) the location the landslide superficial features such as the presence of rock stones, vegetable patches are compared in this way the movement in landslide are determined. These measurements are performed manually within a GIS environment. The maximum deviation and the mean error are also quantified (Niethammer et al., 2010).

In Terrestrial Laser Scanning (TLS), a beam of laser light is used for the analysis of targeted material. Time-lapse scanning can provide the high-resolution pictures of the landslide can be compared for the deformational rates of the landslide at different environmental conditions. The processing of landslide data is divided into two phases the preliminary treatment of the laser data; the analysis on point cloud. The preliminary treatment constitutes of noise reduction (filtering), the point clouds generation and referencing. This leads to a noise-free point cloud, which helps in the second stage of processing. In the second part of the data processing, the surface model of the objects is formed by using a different set of operations, starting from point cloud.

## **2.4. APPLICATIONS**

### **2.4.1. APPLICATIONS OF NM**

Applications of NM comprise aftershock surveys for natural and man-made seismic sources, active fault mapping, sinkhole activity, monitoring of volcanic and induced seismicity associated with landslide, hydraulic fracturing, and engineering structures under stress (Joswig & Wust-Bloch, 2002).

#### **2.4.1.1. LANDSLIDE MONITORING**

Evolutionary failure process leads to large scale deformation which cast huge damages to live, material and properties of the countries through the globe. It is very difficult to mitigate the effects of these hazardous because of non-linearity of multiple causing factors (Walter et al., 2011). This multiplicity stressed the need of deploying geophysical instruments on these

unstable slopes. Different studies have been carried out in the past for the analysis landslide dynamics. One of these efforts is the development of NM which was applied to Heumoses slope, Austria (Walter et al., 2011). This slope was creeping in nature and was resolved into discrete rupture episodes on the basis of seismic rupture signals. The spatial distribution of fractures was concentrated in parts of the slope with higher deformational rates at the surface. The temporal occurrence well correlated with rainfall events and reinforced the assumption of a rainfall-triggered slope movement. Same technique was applied for the detection of impact signals at Super-Sauze mudslide in the southern French Alps. Where waveform and sonogram analysis were applied to discriminate the variety of events and on the basis of the spatial distribution of their epicenters, a mechanical phenomenon was associated with each type of the signal. Authors concluded that the slide obviously relieves stress continuously, but extensive rainfall could trigger stronger material failure processes (Walter & Joswig, 2009).

However, monitoring results at two LS, Huemose and Super-Sourse in Europe showed the contradictory results. In one slope the concentrations of slidequake/stress-relief were maximum at the low displacement rates while at other these concentrations and displacement rates aligned well. This problem was solved later by Walter & Joswig, (2012) using NM the authors concluded that these contradictory results were because of different relief topographies overlaying the bedrock. The bedrock influenced the stress mechanism.

In the case of Mudslide at Super Sauze, the events recorded by NM were divided into three categories based on author's hypothesis. First type of the signals was concentrated in portions of the slope that had maximum movement so these signals were linked to the fracturing in the moving mass. The second type of events was populated near the free boundaries of the material so they were linked to the scratching and grinding of the material. Data acquisition phase was consisting of 10 days recording with 4 SNS. Data was collected in continues mode with sampling rate of 400. First the shorts were used in order to determine the true velocity model. The data processing was done with HypoLine software as described above. The recorded material failure signals vary in duration, amplitude, frequency contents and their sonogram patterns, on the basis of these characteristics along with the site effects on the signals help authors in signal nomenclature.

The precursory stress relief signal ( $-0.5 > ML < 0.4$ ) associated with rock mass failure was studied at Huemose slope some 5 km away from the Alps by using relative and master event localization approaches. Avalanche as well as fracture signals where observed with their

relatively large epicenter distances. The metrological factors were tested for the possible source mechanism detection but unfortunately, it was not resolved by the authors.

Table 2 F-t signatures and principal characteristics of seismic events induced by creeping LS dynamics (Vouillamoz, 2015)

Signal type	Time duration	Energy content& phases	Max. peak to peak amplitudes and local magnitudes	Source location	Numb. of recording seismometers	Number of events (weekly basis)
Rockfall and Avalanche (SS) Rock bearing faces	Few sec- 20 min (single vs. multiple events)	High frequency noise band (up to 130 Hz): falling fine grained material Broadband spikes: falling blocks. No phase identified	50-500 nm s-1: weak events recorded by a few stations only 1500 nm s-1: strong events recorded by complete network	Estimated by back azimuth	8-16	Up to 100's
Fracture (SS & HS) Rock bearing faces	≈ 2 sec	P phase: 50-100 Hz S phase: 10-70 Hz	≥ 1000 nm s-1 ML ≤ -0.5	Standard location procedure	4-20	1's – 10's
Slide quake (SS & HS) Within the LS body	SS: 2 – 5 sec HS: 0.5 – 4 sec	SS: P phase: 10-80 Hz Later phases: 5-30 Hz HS: P phase: 10-120 Hz Later phases: 10-70 Hz	40-2000 nm s-1 SS: -3.2 ≤ ML ≤ -1.3 HS: -2.2 ≤ ML ≤ -0.7 Corresponds to fracture length of some meters	Standard location Procedure SS: zone of highest displ rate (11 m y-1) directly linked to bedrock topography. HS: zone of rel. lower displ. rate (0-5 cm y-1) directly linked to bedrock topography	4-12	SS: 10's Clustered HS: 1's Clustered
ETS-like Within the LS body	2-20 sec	≈150 Hz No phase identified	Just above noise level with enormous attenuation at higher recording distances	Estimation by back azimuth or closest recording station	4-8	10's-100's Clustered

#### **2.4.1.2. MONITORING OF GRAVITY-INDUCED SLOPE**

NM was applied recently to a rock slope in noisy environment. The installation of SNS was consisted of accelerometers and was divided into permanent and temporary networks. About 1300 events were detected with permanent SNS, then these events were divided into failures and collapse events based on their sonogram patterns (Figure 4). Then an index was developed based on the occurrence of these microseismic events and it would be used as a potential for alter. The recoded microseismic events were in good agreement with the evolutionary geological model of the ongoing gravitational slope deformation. Based on the potential use of NM authors had recognized collapse and failure stages of slope deformation as well as localization and magnitude estimation were done based on the physical parameters (frequency content, time duration and PGA) of the recorded signals. The concentration of so determined hypocenters agreed with the presence of deformational features on the rock slope (Fiorucci et al., 2016; 2017).

#### **2.4.1.3. STRUCTURAL HEALTH MONITORING**

Prefailure brittle impulsive signals emitted in response to applied stress where analyzed in three stages at Carverns in chalk. Wast-Bloch and Tsesarsky, (2013) carried a study in which the waveform, associated with structural health, was characterized by Nanoseismic Monitoring. The study was carried out in three states, 1) complete characterization of signal in time frequency and space domains in a laboratory scaled experiment. 2) These signals determined by NM were calibrated with the lab scale experiment result. 3) In third and last stage the reliability of pre-failure and failure signals were tested with the modelled stress distributions in the Carverns which showed good correlation with the concentration of microfractures determined by NM. The combined analysis was done with a marble plate subjected to four-point bending tests. The impulsive signals associated with stress accumulation in marble plate (mm) were classified as Quake ( $0.5 \geq t \geq 0.2$  s), Spike ( $< 0.05$  s), Puff ( $0.3 \geq t \geq 0.1$  s) and Tremor ( $> 0.3$  s) on the basis of full wave characterization. The events were linked to source processes by this controlled experiment setup. Results were compared with other techniques like acoustics. Beit Guvrin National Park (Israel) was then monitoring by a series of campaigns in order to understand the prefailure and postfailure mechanisms in real field (natural) conditions. Four SNS were deployed to understand its prefailure dynamics by NM. Signal

detection was done by comparing them similar studies from the past and on site manual events simulations. The detected event magnitude ( $-2.4 \geq ML \geq -3.8$ ) was found similar to the signals emitted by the sandstone cliff (Wust-Bloch, 2009). Authors did not find sharp differences in the event duration of these sites.

#### **2.4.1.4. CLIFF EROSION MONITORING**

Another important functionality of NM was observed in the seismic analyses of an unstable cliff at Mediterranean Sea. The erosion of banks by the accumulation of tidal energy is a continuous threat to structures and population at the sea shore. A dense network of SNS was deployed. The continuous six hours recording gave the authors so many spiky nanoseismic signals associated with the cliff material deformation. Spatial distributions of maximum recorded amplitudes of nano signals gave rise to respective spatial distributions of deformational stresses in the cliff. Atypical event decay with time is because of post collapse stress accumulation that led to the appearance of tensile cracks (few cm) on the surface of cliff. This study has also strengthened the potential applicability of NM for the detection and identification of the pre-collapse signals emitted by unstable cliff before total collapse.

#### **2.4.1.5. PRE-COLLAPSE IDENTIFICATION OF SINKHOLES**

NM was applied to identify sinkholes before their collapse in Israel (Wust-Bloch & Joswig, 2006). Thus, the low energy events can be identified and located before total collapse with NM in unconsolidated layer media. Because of the absence of prior knowledge, authors performed many simulating experiments to calibrate their results. Waveform analysis was performed by sonogram which categorized the signal into two events as impact in dry and impact on liquids. HypoLine (software) was successfully used to locate individual sinkhole events by just a few, low SNR seismograms, and  $M_L$  scale was calibrated to very low magnitudes, estimated from their source energy. It is now possible to monitor subsurface material failures before sinkhole collapse since the discrimination of impact signals on the basis of their frequency content is indicative of the maturity of the cavitation process.

#### **2.4.1.6. HYDRAULIC FRACTURING**

The fractures are created in the rock mass in response to pressured fluids injection. This technique is being used to create permeable mass in the rock volume that increases the oil recovery by providing permeable mass for the fluid migration. These fractures generate microseismic signals. Location of these microseismic events is important in reservoir stimulation. Microseismic is a famous technique which is used for analysis of hydraulic fractures, an expensive technique and is also rely on high SNR. Silva, (2010) applied NM for the recording and localization of microseismic events in response to injecting fluid as a part of her master's thesis. The events were separated by sonograms analysis and their localization was done by HypoLines. In that study field tests with controlled sources were made at various distances from the sensors and were localized by NM. In a second stage, perforation shots in an oilfield were monitored. One perforation shot was located with slant distances of 861 m and magnitude  $-2.4 M_L$ . Based on results author reached a conclusion that the method has potential to be used for the monitoring of hydrofracture.

#### **2.4.1.7. ACTIVE FAULT MAPPING**

The microseismicity associated with the active faults in Spain along with its relationship with regional catalog was studied for the very first time by Häge & Joswig, 2009. Data was acquired by one SNS over the period of two nights at two different locations of Crevillente Fault Zone (CFZ). The magnitude threshold achieved during this campaign was  $M_L = -2.6$ . Gutenberg-Richter relationship was used to know the occurrence of smaller events from larger earthquakes. However, this relationship was extrapolated by few researchers in order to determine larger events from smaller one. The analysis of the frequency-magnitude distributions showed a good approximation among the amounts of recorded events with those of extracted from local catalogs.

#### **2.4.1.8. JOINT APPLICATIONS**

The nonlinear interaction of multiple triggering factors has increased the vulnerability of models dealing with landslide because of uncertainty involved in the determination of these parameters. In these conditions, the single use of traditional models can produce erroneous results and joint analysis are suggested. Keeping it in mind the two high resolution techniques, NM and Unmanned Aerial Vehicles (UAV) based imaging of slope were combined by Walter et

al. (2009). The slope displacement analysis was done by comparing the stones, rocks and vegetation present in the photographs taken at different times. At Super-Sauze the fracture and scratch signals were localized by the combine use of UAV and NM. In these campaigns the resolution of 1-10 cm per pixels was achieved with a flight height of 10-100 meters by a specially designed quad-rotor vehicle. This resolution per pixel is essential to identify the fractures. Some of the signals were detected by clear onset phases on which the standard seismological processes were done. These detected signals have 2-3 second duration, frequency range 10-80 Hz and peak to peak amplitude value varies from 40 to 400 nm/s. Impulsive signals associated with brittle deformation were recorded by 10 days recording campaigns with SNS. The signals were then processed by Hypoline as described by Jowsig, 2008. For the detection of these signals they must be recorded at least at two different stations. The estimated detection threshold for these events is  $M_L = -2.6$  at a slant distance of 140 m. The upper few meters surface of slope that was dried out in summers because of shear resistance was the home for the generation of both fractures and scratches. At Huemose slopes which provide greater slope movements a joint study was carried out by Walter et al. (2012). In that study, the slidequakes generated in response to stress relief mechanism were analyzed and these events were mapped with a combined use of NM reflection and refraction seismic. Authors concluded that the generations of slidequakes were related positively to the rainfall intensity. Nano seismic findings were supported by the existence of fissure patterns at the slope surface which could be observed by UAV-based remote sensing of the slope surface (Walter et al., 2009).

#### **2.4.2. APPLICATIONS OF GEOPHYSICS TO LANDSLIDE DYNAMICS**

The effects of rainfall induced pore-pressure and water conditions (stiffness variations) on the dynamics of landslides were discussed in previous studies (Walter et al., 2011; Vouillamoz et al., 2018) where Nanoseismic Monitoring was used for the analysis of landslide dynamics. The landslide dynamics was studied in terms of the detection and localization of weak energy signals, referred to as slide quakes, released because of rainfall induced brittle failure in the landslide mass (Got et al., 2010; Bottelin et al., 2017). However, this mechanism of micro seismic emission from the clayey landslide received criticism. Under these conditions the ANb techniques are used, where the properties in the ambient noise wave-field are analyzed and linked with the material deformation inside the landslide body.

In the case of rainfall, the cracks/pores of the landslide material are filled with water compared to cracks with air so the velocities are expected to increase. The S waves do not pass through

fluids while velocity of P waves increased when travel through water. These fluid dependent variations in both S and P wave velocities alter the velocity of surface waves which can be theoretically quantified in terms of  $dV/V$  calculated from ANI.

Same is the case with rise in pore-pressure because of rainfall water can lead to reduction in shear strength of the porous medium by counteracting normal stress (Saar and Manga, 2003). A small increase in applied stress to a porous medium near to its critical value, can provoke a failure (Saar & Manga, 2003), which can again identified by the time-lapse changes in the velocity of surface wave using ANI. Therefore, the relative time-lapse changes in surface wave velocities obtained from ANI can help in the quantification of rainfall induced changes in the landslide mass such as rheology and rigidity (Mainsant et al., 2012a) and pore-pressure induced stresses.

The relative velocity changes are measured using ambient noise interferometry. These seismic velocity changes are used in the determination of time-invariant (i.e. geometry, sliding surface location) and time-changing (i.e. saturation, mechanical properties, rheology) landslide features. The prominent ambient noise studies are Mainsant et al., 2012a; Voisin et al., 2016; Harba and Pilecki, 2017. In spite of providing interrelated information of hydrology (watertable fluctuations) and related dynamics of landslide, the seismic noise can also be used in groundwater management studied (Fores et al., 2018).

The geophysical techniques would distinguish determination of time-invariant (i.e. geometry, sliding surface location) and time-changing (i.e. saturation, mechanical properties, and rheology) features (Yalcinkaya et al., 2016). The same techniques have been applied in many studies to achieve various goals, possible applications include seasonal landslides, dams, volcanoes monitoring, reservoir characterization, earthquake relocation, stress monitoring in mining and rock physics.

#### **2.4.2.1. TIME-LAPSE LANDSLIDE MONITORING**

Theoretically, there are three main reasons for velocity change, stress changes (Nur, 1971), fluid saturation (O'Connell & Budiansky, 1974), fluid pore-pressure (Brenquier, 2014) and damage within the material (Lockner, 1977). The movement of two blocks over each other may possibly be triggered by the water table fluctuations. The sensitivity of seismic waves to the moisture

induced mechanical changes, can be used for the evolution of the rigidity (rheology) of landslide slope (Mainsant et al., 2012a).

The anomalous change (two or three-fold decrease) in the shear wave velocity, calculated by ANI is observed before the occurrence of a landslide (Mainsant et al., 2012). These changes in S-wave were correlated with the sacrificial displacement rates. In another study under controlled conditions were carried out by Mainsant et al. (2012b), where the changes in S-wave velocity were linked with the changes in rheology of landslide and according to Harba & Pilecki, (2017), the rheological changes are the basic cause of many landslides in clayey formations. It is concluded from these studies that S-wave velocity can be used for landslide monitoring.

Another application of geophysical techniques is the determination of landslide slip surface. However, deeper slip surface can be determined by ambient seismic noise, where active seismic is not suitable (Renalier et al., 2010a; Yalcinkaya et al., 2016). Dispersion curves of lower frequency (3Hz) were used for the deeper slip surface depth estimation. The lateral and vertical variations in calculated S-wave velocity may be possibly related with the landslide dynamics. The authors used ambient noise cross-correlation for the 3D S-wave model of the clayey landslide (Renalier et al., 2010b). In order to record Rayleigh wave Green functions vertical components were cross-correlated, which give rise to group velocity dispersion curves at frequency range of 1.7-5.0 Hz. From the inversion of these dispersion curves, 3D S-wave velocity model of landslide was derived.

The seasonal variations in S-wave velocity over landslide were calculated using ambient noise interferometry. The so derived geometry had a good correlation with the available engineering geological cross-sections. The possible use of high frequency noise as a tool for the identification of rheological changes in the geological material was discussed. A decrease in S-wave velocity was related to the increase in water contents and decrease in material strength. These findings can be used in designing landslide early warning system (Harba & Pilecki, 2017).

Earth dams and levees (EDL) have greater importance in the flood protection, allocation of fresh water and availability of energy worldwide. The internal erosion is a process that effects these structure greatly (Planès et al., 2016). In a lab-scale experiment of Canal Embankment failure experiment has checked the suitability of time-lapse monitoring. The acquisition system was consisted of 4 Hz 10 geophones Then CCFs were calculated at each frequency band. At each frequency band the apparent group velocity and baseline group velocity (hammer impact)

are compared. At low frequency the wind turbine was found to be the dominant source of noise. Time-lapse changes were monitored by stretching technique between reference and current Green function. This study shows that, the monitoring of changes in stress related with mining, radioactive waste disposal sites and the fault zone is very essential along with landslides and ANI can be successfully applied to achieve these objectives with the modest hardware requirements.

#### **2.4.2.2. GEOPHYSICS FOR LANDSLIDE SITE CHARACTERIZATION**

The electrical resistivity tomography applications are landslide reconnaissance and can be of 2D and 3D for the analysis of complex landslide structures. However, very recent times there are 4D monitoring techniques are applied as well. For that purpose, a permanent array of electrodes are installed on the landslides that provide imaging of landslide mass at various time-scales can be validated against remote sensing data or by self-potential monitoring systems in the case of hydrological studies (Méric et al., 2007).

The applications of GPR in various fields such as geology, geomorphology, glaciology, environmental science, engineering-geology, hydrological studies has increased drastically. This GPR utility hype is mainly because of following advantages offered by the GPR 1) its high resolution, ranges from a few cm to a few m; 2) its wide range of penetration depth in resistive materials; 3) its sensitivity to dielectric, electric and magnetic contrasts and particularly to water content, and; 4) its light instrumentation (Jongmans & Garambois, 2007). The other essential applications of GPR in landslides are, mapping the depth of bedrocks (Bichler et al., 2004), pattern characterization of subsurface fractures (Deparis et al., 2008) and estimating the layering of buried structures (Lissak et al., 2015). GPR applications in the case of natural hazard assessments are: rockslide characterizations (Heincke et al., 2005), quick clay sites (Sauvin et al., 2013) and unstable permafrost (Maurer & Hauck, 2007) (Malehmir et al., 2016).

In TLS technique target object is illuminated by laser light, can be used for high resolution topographic map generations that are utilized in a wide range of applications. The cost-based specification varies with application object and size of the targeted area. It is the most accurate method used for the calculation of DEM and has an advantage of vegetation removal over its counterpart photogrammetry. Along with other geophysical techniques TLS was applied for the reactivation of an ancient landslide by Burda et al. (2013).

A very interesting application that combines passive (seismic noise interferometry) and active (P and surface wave refraction) to characterize the subsoil structure of landslide, was carried out by Cárdenas et al. (2016). These authors applied the seismic interferometry to determine the lateral variation of S-wave velocity in the subsoil structure of a rock mass. ANI method quantifies the elastic properties and their distribution in the slope the cross-correlation 4560 pairs of receivers. After that, they build a 3D model of S-wave velocity (seismo-stratigraphy) with tomographic images ranging from 4 up to 24 Hz. The results are corroborated by the soil structure derived active seismic refraction methods.

### **2.4.3. SUITABILITY OF APPLIED TECHNIQUES**

The severe drawbacks of geophysical techniques mainly due to the complexity of geology in landslide slopes can be minimized by combining their results with the information obtained from geological, engineering-geology and remote sensing data.

Under non-ideal scenarios the determination of impulse response by ANI method become challenging. This becomes even worse if target is noise based tomography. In the case of time lapse monitoring the problem is not so hard to solve. If the array of sensors is in line with the direction of incoming noise wave-field the apparent velocities are considered as true velocities (Planès et al., 2016; 2017). The noise sources should be stationary which seldom happen in the natural scale experiments; these assumptions (non-stationary noise source and white noise etc.) of ANI never met in real world (Planès et al., 2016). Fractures at the surface do not allow the propagation of Rayleigh waves and are attenuated at short distances. In order to record these waves a dense network of sensors is required which increase the cost of experiments many folds. Therefore, the applications of ANI and other passive surface wave based techniques at higher frequencies are not recommend in the case of landslides. Autocorrelation has suffered a limitation based on the ambiguity of the types of waves. It is not clear whether these waves are surface or body which made unclear which part of subsurface was observed.

HVSR technique is based on the 1D assumption, i.e. the material changes only with depth and there is no changes occur in lateral directions, which again not a case with landslide where the changes are expected to occur in both directions. It is very difficult to remove transient ambient noise from the records that make results of this technique unreliable. Depth limitation, presence of fractures at the surface, can cause problem in the propagation surface waves. All surface wave based techniques are affected by the presence of fractures that is usually the case with

landslides studies. The correct peak identification becoming challenging in the case of low subsurface impedance contrast as well as in the case the appearance of two peaks on HVSR curve.

In MASW the frequency dependent variation in phase velocity of surface waves in a layered media are used for the inversion. The nonlinearity and the nonuniqueness of the inversion of surface waves (Rayleigh and Love) can cause misinterpretation of the inversion results (Malehmir et al., 2016). So joint inversions are recommended (e.g. f-k and HVSR curves and MASW and HVSR).

High attenuation of electromagnetic waves under certain subsurface conditions such as, groundwater or soil salinity, degree of saturation, proportion of clay contents reduces the depth of penetration drastically making GPR technique unsuitable under these conditions (Lissak et al., 2015). However, there are severe limitations associated with the use of GPR in the investigations of landslides mainly because of 1) signal attenuation in high conductive formations that limit its application in soil landslides or when water saturation is higher; 2) heterogeneities created by the fractures and cracks cause signal diffractions that decreases the penetration depth (Jongmans & Garambois, 2007).

In spite of underrepresented advantages the high costs of terrestrial laser scanner made it almost impossible sometimes to be used especially for the scientists of developing countries. TL can be used for small and mediate scales however significant capital costs, training, and specialized equipment (Chesley et al., 2017). However, the high precision DEM calculated from photogrammetry are preferred over TLS which take longer acquisition time (Rieke-Zapp et al., 2001).

The emissions of microseismic signals from earth-slides is up to now questionable; in the case of clayey landslide there are absence of brittle material so the energy is not released in the case of collapse. However, sometimes the signals recorded are related with the soil mechanics. Usually these techniques are better described based on ground truth provided by other complementary techniques such as remote sensing of the landslide surface and extensometer data that can significantly increase their reliabilities.

## 2.5. APPLIED METHODOLOGY

The landslide studies carried out in Brazil until now are of three broad categories as 1) Index based susceptibility mapping, 2) Geomorphological analysis and 3) Soil geotechnical parametric estimation by in-situ testing. According to the best of author's current knowledge, no study dedicated to the application of ambient noise based geophysical techniques for the understanding of dynamics of unstable slopes in the region. However, in the 1990s, landslide early warning system was deployed in Rio de Janeiro city which was based on the external dataset only like satellite imagery, Doppler radar (weather forecast) and automatic rain gauge network. In these systems, no attention was given to the pre-collapse dynamics of the slope, which made questionable the effectiveness of the system.

Few studies have applied the concept of saturated hydraulic conductivity ( $K_{sat}$ ) variations at different depth. These variations in  $K_{sat}$  with depths built pore pressures that lead to the reactivation of slip surface or generate new slip surface after intense rainfalls. The different scarps of landslides of 1967 were selected for such type of analysis, the  $K_{sat}$  values were taken with Guelph Permeameter at various depths in order to see their effects on rainfall-induced stress in the landslide masses. Spatial models for shallow landslides were also applied at different sites (Gomes et al., 2013).

In this thesis, the methodology is broadly divided into two parts, landslide site characterization and its dynamic analysis. The dynamic analysis is further divided into two analysis as, (1) monitoring based of changes produced in the ambient noise field due to the dynamic changes in the soil (time-lapse ambient noise interferometry and horizontal to vertical spectral ratio) and (2) based on emitted microseismicity (nanoseismic monitoring). The applications of these methodologies are carried out at controlled and natural experiments.

Geophysical landslide site characterization is done by applying Multi-Channel Analysis of Surface Waves (MASW), Electrical Resistivity Tomography (ERT) and Horizontal to Vertical Spectral Ratio (HVSr) methods. In MASW subsurface shear wave velocity is obtained by the inversion of Rayleigh wave dispersion curve (phase velocity vs frequency) while ERT and GPR make use of the geoelectrical and geomagnetic informations of the substratum, respectively and the best fit model between the observed and measured values provide the subsurface stratigraphy. Data acquisitions at a landslide in a small Ribeirão Contagem fluvial valley was done using 14 Hz geophones and 2D resistivity profiles using dipole-dipole array configuration.

Resultant slip surface and permeable paths were identified well on the modeled resistivity sections, while a three layered 2D shear wave velocity stratigraphic section is obtained from MASW where a continuous increasing rigidity trend and a decrease in velocity at landslide scarp are observed.

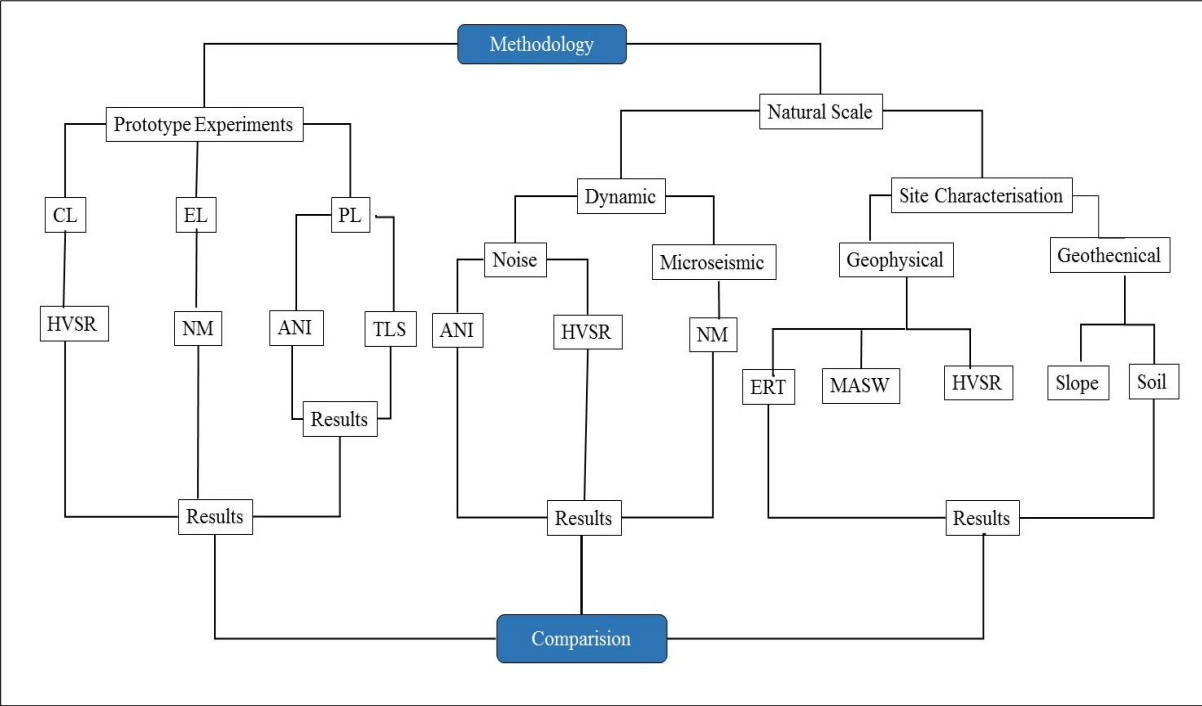


Figure 9 Methodological workflow explaining the stepwise application of the techniques along with their objectives.

Dynamic analysis is carried out where the modifications in ambient noise (HVSr and ANI) due to changes in soil conditions (microfractures and degree of saturation) are observed. A typological analysis (nanoseismic) of the microseismic signals released in response to changes in the soil of the study area and prototype experiment are also included in the dynamic analysis. Workflow of adopted methodologies are shown in Figure 9.

**2.5.1. SOBRADINHO LANDSLIDE**

The Ribeirão Contagem watershed is 146 km<sup>2</sup> extended and it is located in the northern part of the Federal District of Brazil in the Sobradinho administrative unit. The Maranhão River is the main tributary of the watershed that flows in the north and northeast directions. The drainage and channel densities of the watershed are 5.7 km/km<sup>2</sup> and 32.9 channels/km<sup>2</sup> (Ferreira & Uagoda, 2015). The climate in the area is semi-humid tropical with a rainy summer and dry

winter. The mean annual precipitation in the area is of 1,442.5 mm and it is mainly related to rainfalls.

The selected slope is located in Federal District near cow and horse farm in a small vicinity naming '*Rua do Matto*' (Figure 10). This landslide is E-W trending rototranslational earthslide (Varnes, 1978). The landslide is approximately 150 m long and about 70 m wide. Along with the main scarp at the top of the landslide mass, there is a small scarp in the middle which is created by a 2 m height normal fault originated by the release effect of the Capetinga River which cut the slope at its bottom. The river erosion is mainly related to rainfall in the surrounding areas which is quite high during the rainy season. The main observed cultural activities that may be the possible sources of ambient noise are village's activities at the south (*Rua do Matto*).

#### **2.5.1.1. GEOLOGY AND GEOTECHNICAL PARAMETERS**

The Federal District covers the eastern part of the Tocantins Province. The Brasiliano orogenic event (end of Neoproterozoic, some 570 Ma) that is ranked into five deformational phases, due which the Lithostructural changes occurred in the past (Campos, 2004). Towards San Francisco craton this cycle is characterized as compressive tectonics, which presents first of these four stages with folds and ductile-brittle faults that made both dome formation (the Brasilia, the Pípiripau and Sobradinho domes) as well as structural basin creation (Freitas-Silva and Campos, 1998). The geology of DF has been revised and updated in the form of new geological map at 1: 100,000 scale (Freitas-Silva and Campos, 1998). On this new map, four lithological boundaries were distinguished: (i) Paranoá (metasedimentary rocks), Canastra (phyllites), (ii) Araxá (schists), (iii) Bambuí (clayed metasilites rolled, clay and metasilites banks) and (iv) Groups and soil or waste shallow colluvial deposits (pedimentary type). These lithological units are present in reverse successions where the younger litho-structural unit lies above the older ones. The geological setting of the aforementioned succession is mainly related to thrust faulting (Freitas-Silva & Campos 1998).

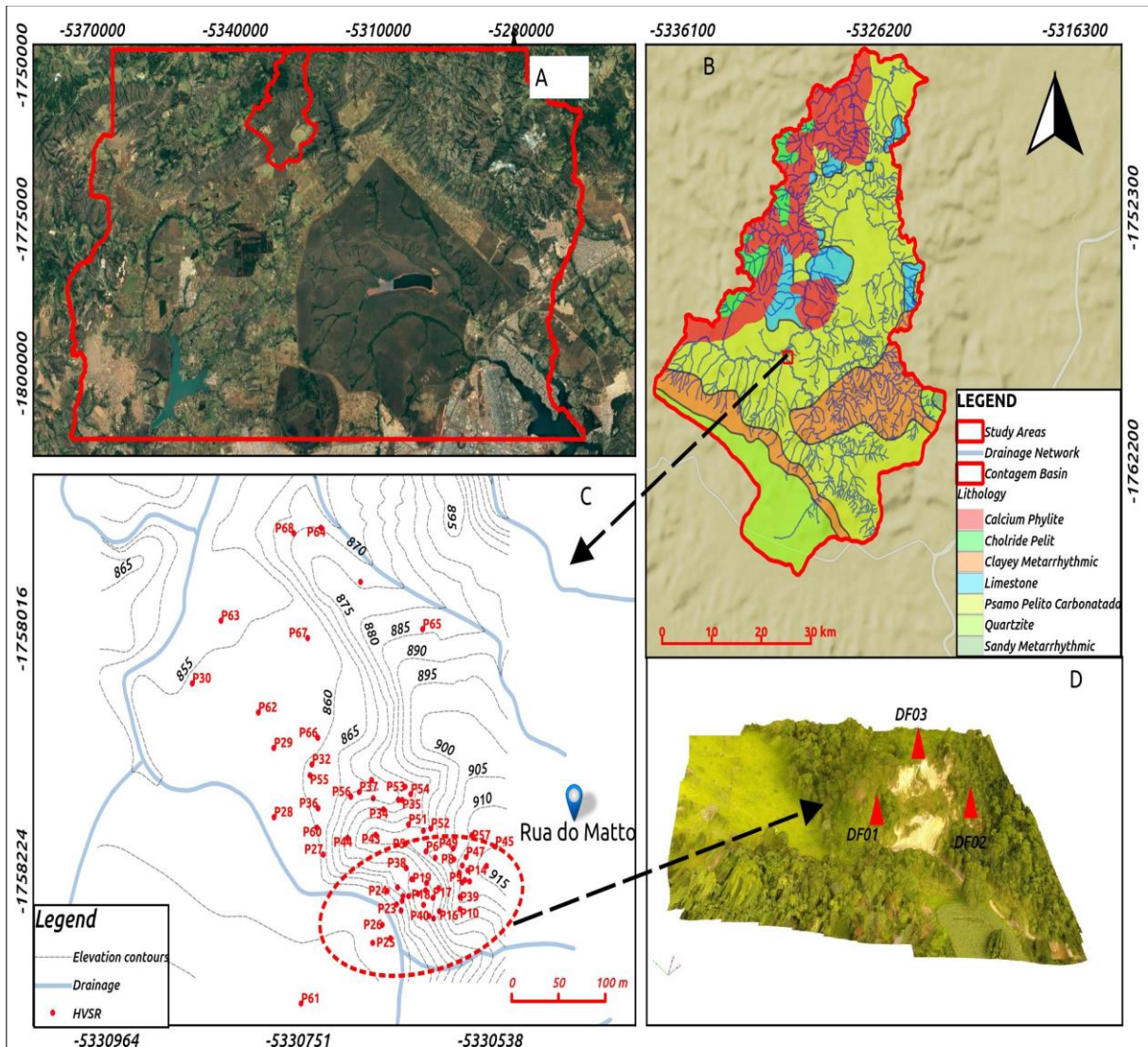


Figure 10 (A) Location of Ribeirão Contagem watershed on Federal District map, (B) its geology, (C) Sobradinho landslide along with HVSr measuring points (red dots), red dashed ellipse is the landslide boundary and (D) zoomed landslide image with triangular array used for time lapse monitoring

On the slope of the Fazenda Buraco, a small portion of the PPC unit emerges, with the carbonate pellet (Figure 11A). The rocks that make up this unit were strongly influenced by background paleogeography, marking the final deposition of the Paranoá Basin. The weathering of these deposits occurred when then come in contact with environmental agents as shown in Figure 11B. Figure 11A and B are photos taken at the drainage margin, showing the contact between the alluvial and colluvial materials, the alluvial having lateral continuity ranging from 30 to 100m from the drainage bed.

In the drainage bed it is possible to observe that the finer grained alluvial material, well selected grains, secondary minerals and low humidity, is superimposed on the alluvial deposits that are composed of poorly selected grains (ranging from medium sand to gravel with decimetric boulders), composed mainly of quartz and with high moisture content due to the water table, these characteristics are shown in Figure 11. In general, the deposits in the channel of the Ribeirão counting are distinguished in:

- Landslide debris due to recent rotational failure mechanism;
- fluvial deposits on recent riverbanks;
- alluvial fan deposits;
- colluvial;
- alluvial.

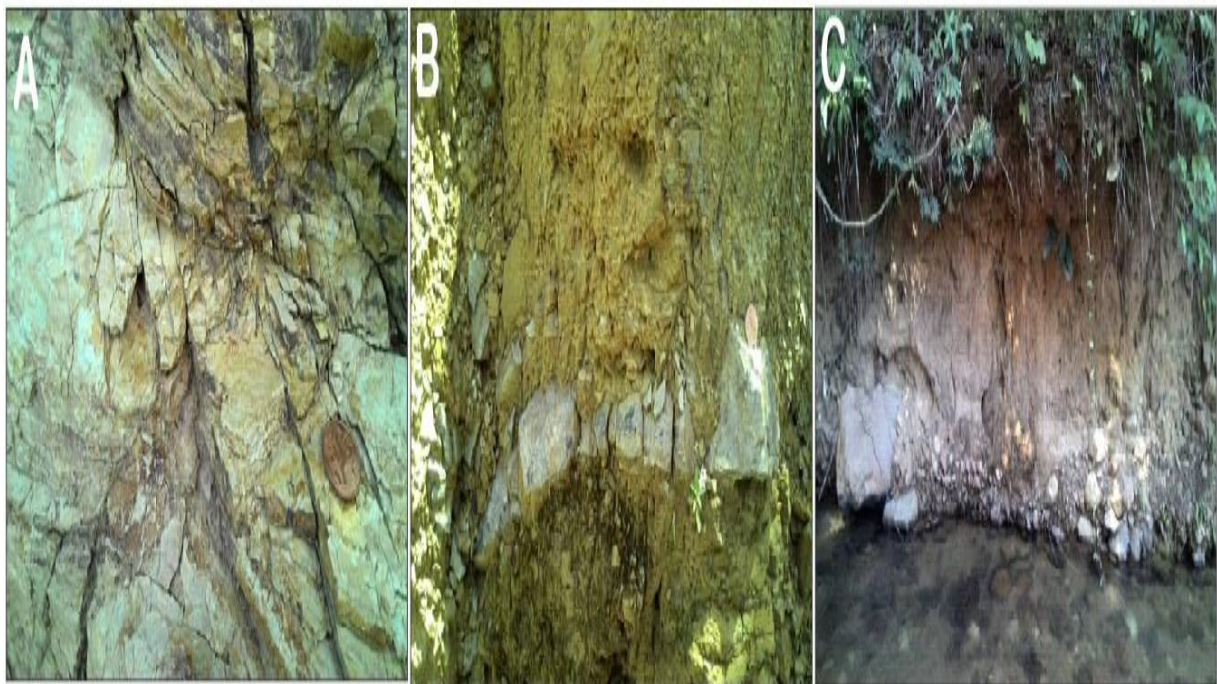


Figure 11 (A) Outcrops of rocks in the higher elevation areas, with a low degree of weathering. B) Saprolite with fragments of quartzite with micaceous minerals. C) Profile photo with alluvial deposit superimposed on the alluvium

The studied area is geologically composed of meta-sedimentary rocks of Proterozoic age that were deformed during the Brasiliano Cycle (650 M) covered by a thick weathering mantle (Zoby, 1999). The Sobradinho Unit, of Votorantim Cimentos Brazil, is located in the Ribeirão Contagem Basin, in which low-grade metamorphic sediments of the Paranoá and Canastra groups occur. The Federal District, more specifically its north-central portion, is in the domain

of the Tocantins Structural Province, in the Brasília Dobramentos Range; where rocks are attributed to the Canastra, Paranoá, Araxá and Bambuí groups of Proterozoic ages (Canastra and Paranoá groups ~1,100 million years old and Araxá and Bambuí groups ~700 million years old). The geology of area consists of Paranoá group (metasedimentary rocks).

## **2.5.2. FIELD SCALED EXPERIMENT**

The optimization of microfracture detectability by HVSR is done by a controlled scaled experiment that was carried out in the experimental field of University of Brasilia, Brazil. In order to minimize the effects of transients (traffic, machinery and anthropogenic activities) the experiment was conducted during the Christmas holidays. A pile of 12 m deep and 0.8 m in diameter was subjected to normal loading until the soil failure took place according to Brazilian standards. The load was kept of rising after every 30 minutes interval. The HVSR technique is applied to each 30 minute long ambient noise record. The loading mechanism consists of a hydraulic jack which applies the load on the top of the pile by pushing oil inside it. This loading mechanism was supported by the two reaction piles of 8m in depth, in order to sustain the reaction of the ground in response to applied load (Figure 12).

### **2.5.2.1. NORMAL SLOPE EXPERIMENT**

A two meters wide and 1.5 meters deep excavation was dig in the experimental field of Department of Civil and Environmental Engineering, University of Brasilia, Brasilia, Brazil. Recording took place on a Wednesday (21/02/2018) night between 22:00h-02:00h when no transients were present because of local human noise and traffic. This excavation is a prototype experiment that is analogous to the normal slope in tropical clay. The seismic acquisition system consists of three seismometers, Ref-Tek-130 data-loggers and GPS locks. The data was recorded at sampling rate of 1000 sample/second. The sensors were time synchronized by GPS locks.

The objective of this experiment is to check the response of Brazilian soil under different loading conditions. Which is achieved by vertical load applied on one flank of this slope. This loading will receive a reaction from the ground. Consequently, the loading mechanism becomes unstable. This problem is solved by contraction of reaction piles/shallow foundations based on the calculation of soil parameters (taken from previous works) of the experimental site.

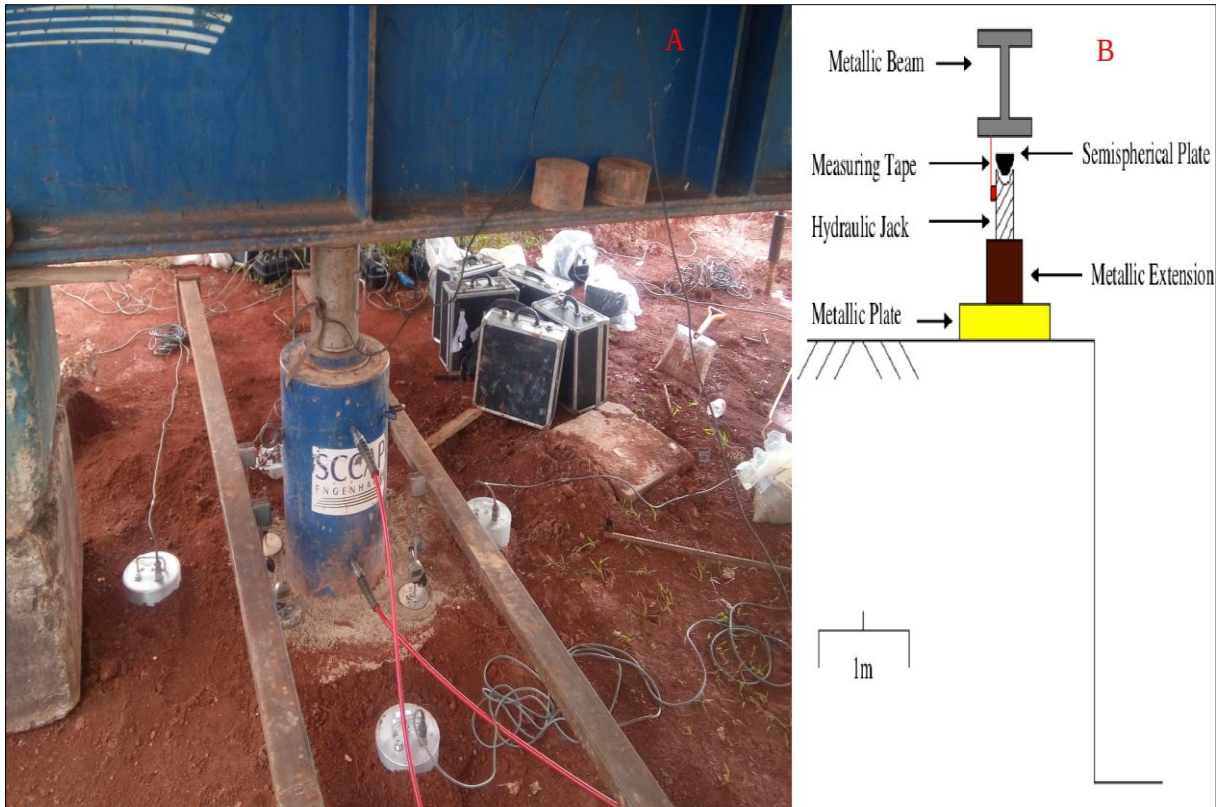


Figure 12 Prototype field experiment (compressional test) in the University of Brasilia. Position of the seismometers (A) as well as loading mechanism (B) are shown.

In order avoid the background seismic noise, the following loading mechanism was set in place (Figure 12): 1) Two reinforced concrete piles (reaction piles), 0.8m diameter and 12m deep piles. 2) On the top-level surface of each pile vertical stress was applied. 3) On top of the piles a rigid, two double T shaped metallic beams were placed supported by the concrete blocks stands, restricting its movement. 4) Below the metallic beam and in between two consecutive piles a soil area of 1m<sup>2</sup> was leveled. 6) This formed the base for the installation of a hydraulic jack, which was in turn connected to a manually operated oil pump. By increasing the oil pressure the hydraulic jack was pushed against the metallic beam and the soil surface, thus increasing the load on the crown of normal slope. 7) Attached to the hydraulic jack and the metallic beam there were four extensometers for the monitoring the vertical displacement of the slope crown from four sides. All parts of the loading mechanism were leveled to ensure that the load was applied vertically. In this way the loading mechanism itself and would have comprised a health and safety hazard.

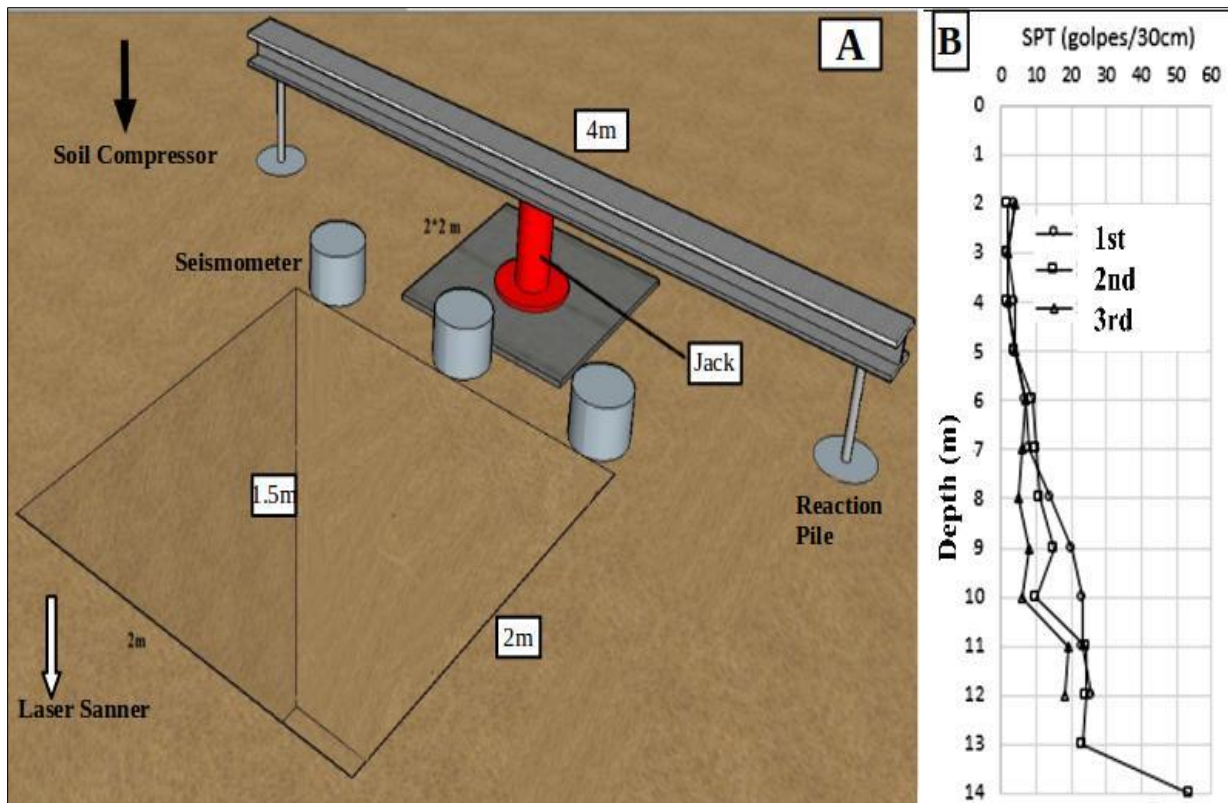


Figure 13 Experimental setup dimension of excavation, reaction piles, positions of seismometers, location of artificial source of ambient noise and presentation of loading mechanism.

### 2.5.2.2. EXPERIMENT ON EXPANDER BODY PILE

The Expander Body (EB) pile technology has been used successfully to increase the pile toe capacity of bored piles in loose to dense soils (Arce & Herrera, 2016). However, in the present study the pull out test on EB pile is used as a mechanism that leads to soil fractures. How these fractures are produced lie beyond the scope of the present study. The experimental site was chosen to be in the city of Brasilia (Brazil). Measurements took place on a Wednesday (21/02/2018) between 10:00h-14:00h. Following pull out test mechanism was set in place. Two concrete blocks were set in place, above these blocks placed two steel rods (Figure 14). A load cell is placed above the rods. A hydraulic jack is attached to this load cell. This formed the base for applying pulling force on the EB pile by a manually operated oil pump. Attached to the hydraulic jack there were two smaller metallic rods on which four extensometers were installed for the monitoring of vertical displacement of the pile during the experiment (Figure 14). The objective of this experiment was to control the exogenous processes and to record the failure

mechanics of tropical soil. In this way, all tremors are because of endogenic (failure mechanics) processes throughout the experiment.

The seismic acquisition system consists of four short period (2 Hz) seismometers, Ref-Tek-130 data-loggers and GPS locks, deployed in the form of mini-array having 30 m aperture. Mini-arrays or system navigation system (SNS) are deployed by using three nails at these nails angles are measured using a magnetic compass. Same mechanism of mini-array installation is adopted for both experiments. The data was recorded at sampling rate 1000 sample/second at prototype field experiment and 250 sample/second for the natural scale experiment. In both experiments the recording system remained same.

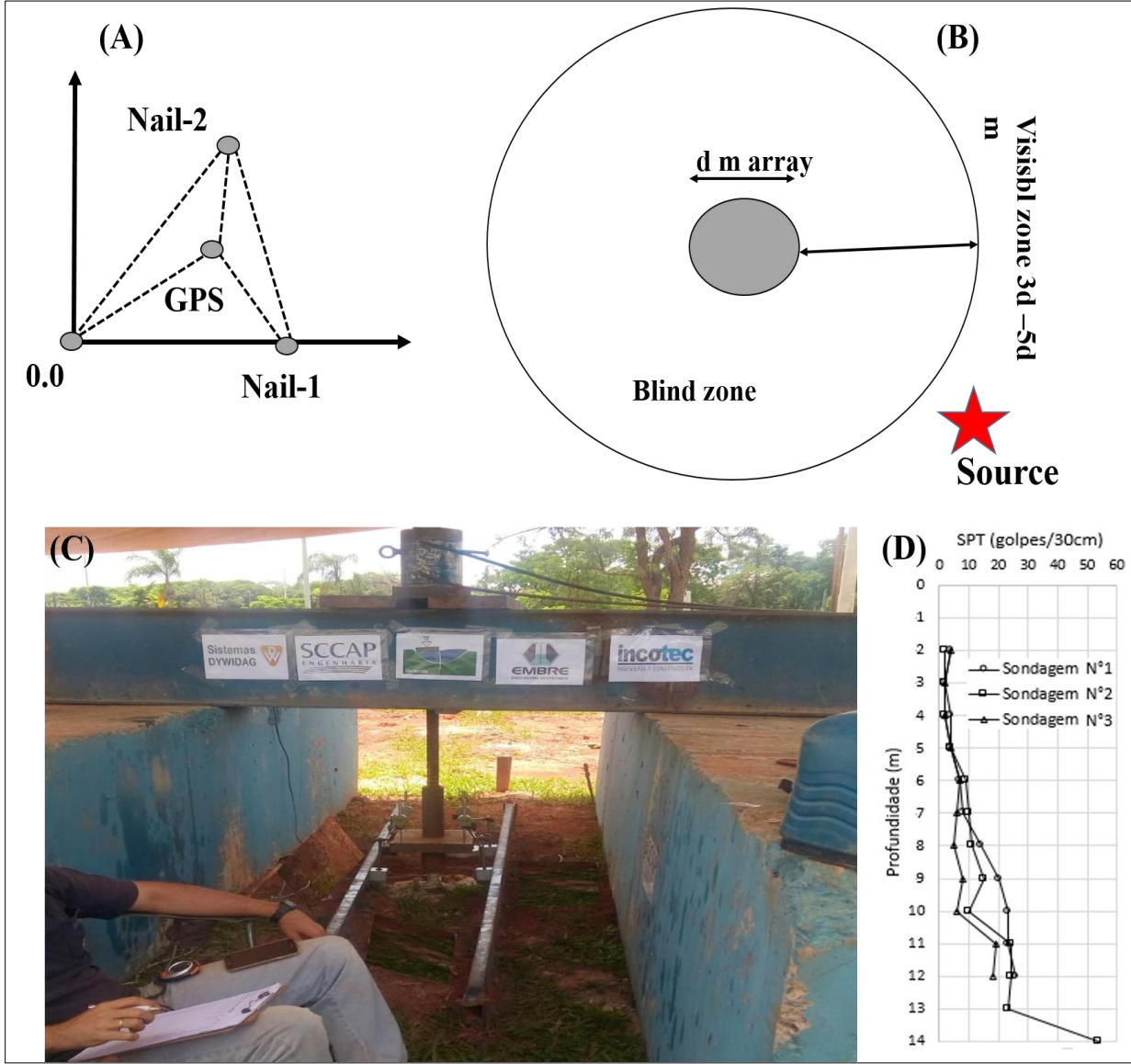


Figure 14 (A) Mini-array configuration (B) its blind zone (Personal communication, Salvatore Martino) (C) Mechanism used for extraction test on expendable body pile and (D) SPT-N profile of the soil of the experimental site.

## 2.6. DATA ACQUISITION AND PROCESSING

### 2.6.1. ERT AND MASW

The field equipment for MASW survey are a source (impulsive) of seismic energy (usually a hammer and a plate), two or more receivers and a computer based acquisition system. According to Stark et al. (2013) the source of seismic energy must generate energy at a large range of frequencies, so that different zones of dispersion curve can be analyzed. The layers in substratum having different impedance contrast lead to the dispersion of Rayleigh waves that means its propagation speed changes (phase velocity) and is calculated (function of frequency) from dispersion curve (Stark et al., 2013).

Table 3 MASW and ERT acquisition parameters

<b>Parameters/ MASW</b>	<b>Settings</b>	<b>Parameters/ ERT</b>	<b>Settings</b>
Configuration	Linear	Configuration	Dipole-Dipole
Geophones interval	2 m and 5 m	Electrode interval	5m and 8m
Number of geophones	36, 48 geophones	Number of electrodes	36
Geophone type	14 Hz (Vertical)	Electrodes type	metal
Nearest offset	Presented in Figure 4	Not apply	Not apply
Source equipment	8 kg sledgehammer	Source of current	12 V battery
Sample rate	0.5 milliseconds	Not apply	Not apply
Record length	2, 1 second	Record length	Not apply
Stacking limit	10,15 stacking	Not apply	Not apply

Survey planning for the MASW and ERT were done using Google earth. The data were acquired along three profiles in the study area in such orientations so the projected area can be covered (Figure 15). The multi-channel Geode (Geometrics Inc.) seismograph along with 14 Hz geophones were used for the data acquisition. The seismic source used was a hammer with 8 kg, struck against a metal plate placed on the ground. Energy generation at each point was repeated (5 and 15) times and stacked in this way the signal to noise ratio was improved (Akpan et al., 2015). The positions of the source for each line were from the first geophone is shown in Figure 15. A total of three seismic sections were acquired, with 95 (L1), 48 (L2) and 70 (L3) meters in length. The longitudinal profile (L1), along with resistivity profile ERT-1, passes

parallel throughout the length of the landslide. The profile L3 along with ERT-2 run perpendicular to the landslide and their small portions touch the landslide scarp at the top (Figure 15). The profile L2 is taken on alluvial deposits lie behind the landslide, its end passes through the alluvial colluvial material (grain size variations) interface presented in previous geotechnical studies (Braga et al., 2018). The acquired MASW data was processed and interpreted with ZondST2D (<http://zond-geo.com/english/zond-software/seismic-tomography/zondst2d/>) software, (in a version demo), which help us to derivate shear wave velocity from the dispersion curves. The data processing phase can be divided into three steps (i) raw data is filtered for the analyzable range of Rayleigh waves frequencies (ii) develop phase velocity dispersion curve and (iii) then finally Vs profiles are obtained from the inversion. The record is domain transferred where the surface waves appeared as high energy branches, the frequency appears as a function of wavenumber, wavelength, slowness or phase velocity, that make the picking of high energy (amplitude) events easy. For domain transfer, the data is decomposed into individual frequency components that is achieved by Fast Fourier Transfer (FFT) after that amplitude normalization is applied to these decomposed components.

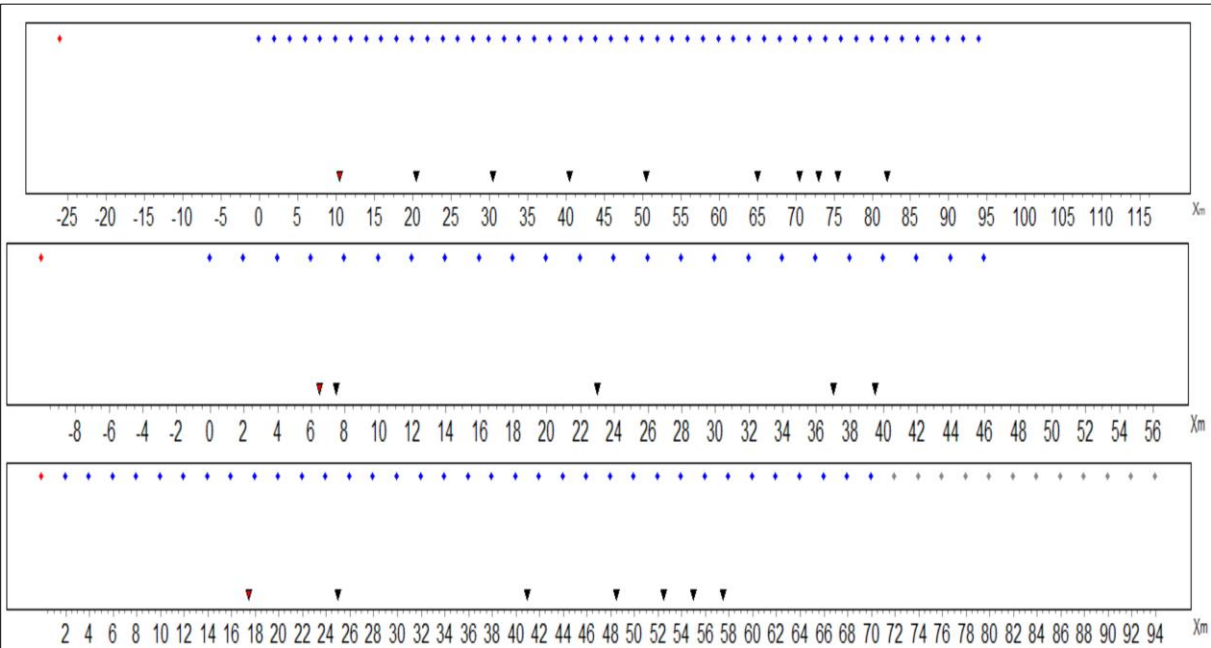


Figure 15 MASW acquisition geometry at three profiles (top to bottom L1, L2 and L3) Inverted triangles are the source portions while blue dots are the positions of geophones.

For a certain phase velocity range, a necessary amount of phase shift is calculated in this way the delay time generated by the sensors offset can be compensated. This procedure is repeated for all the individual components of different frequencies are results are summed to a total

energy. This summed energy patterns in frequency vs phase velocity space resents dispersion curves. On the dispersion curve, the energy behavior appears as multi branches in the case of multi-modal dispersion (Sauvin et al., 2016). Unprocessed data of MASW and ERT are shown in Figure (16).

A single channel acquisition system of Iris Syscal DC resistivity system with a 5m and 8m electrode separation of dipole-dipole array at parallel (ERT-1) and perpendicular (ERT-2) to the landslide was used for the collection of the DC resistivity data (Figure 15). The acquisition and geometric parameters were provided to resistivity meter before going to the field and after that, it works automatically and takes measurements along several electrodes connected with a multicore cable.

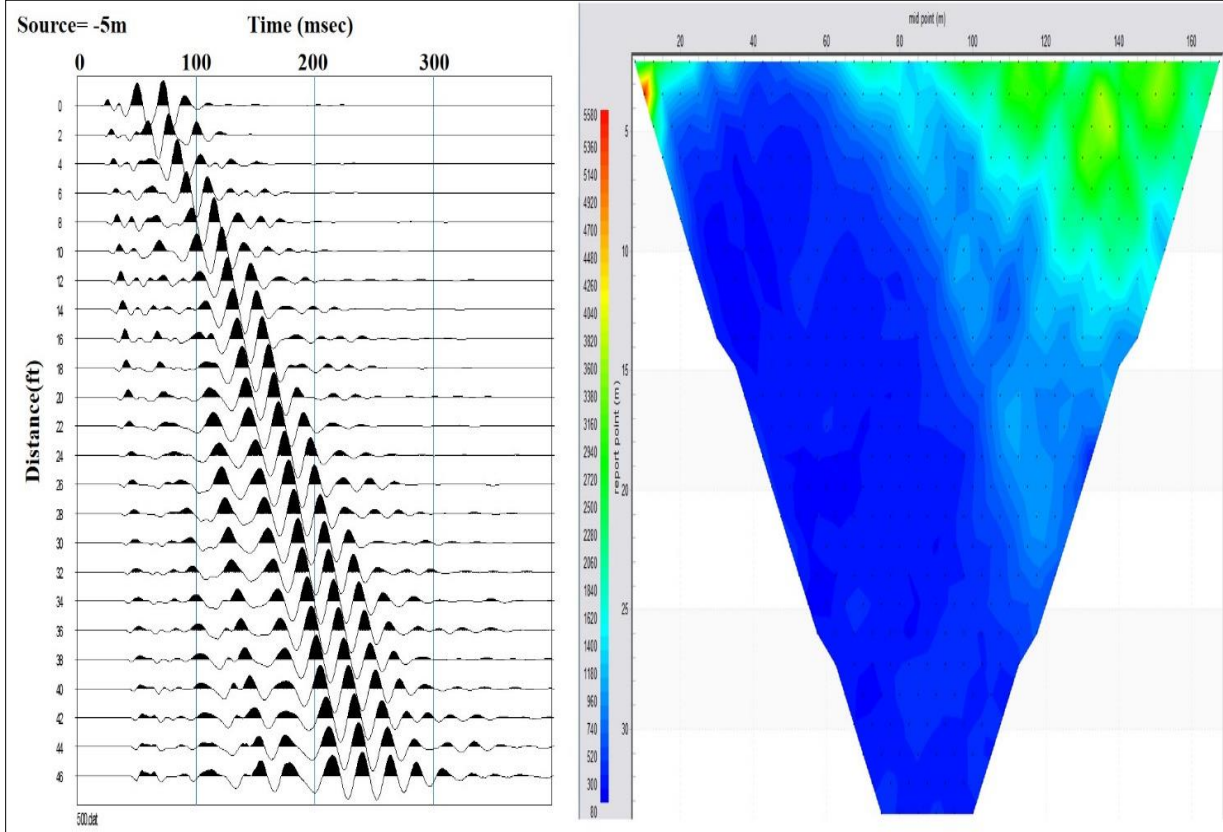


Figure 16 (A) Seismogram of the profile L2 and apparent resistivity values at profile ERT-2 are shown.

The signal to noise ratio was improved by pouring salt water at each electrode during acquisition and muting bad data points from the record during the preliminary data scanning step in the Prosys II software. After editing, the data was saved in a new file format compatible with RESIS2DINV of Geotomo Software (Loke, 2004), where the inversion of resistivity data

is performed. In this software, a best fit earth model is generated from the apparent resistivity values. For that cell based resistivity calculation is made through the application of smoothness-constrained least-squares inversion method (Sasaki, 1992) that search for an idealized model for the resistivity distribution in the subsurface and its best fit with the calculated measured resistivity values (Colangelo et al., 2008). In this method, the subsurface is divided into rectangular blocks each representing single measuring point (Lapenna et al., 2005).

The root mean square error (RMS) provides the discrepancy between measured and calculated values. Data were acquired using Sorcel L-4A-3D short period seismometers having natural frequency response of 2Hz. The records were performed in a continuous mode and at sampling rate of 250 sample per second (SPS) with DAS-130 RefTek data loggers. Time and positions are provided by the GPS-130 locks.

The first goal was to mark the boundary of Sobradinho landslide, the number of single station measurements were taken both inside and outside the landslide mass (Figure 10). These campaigns were done during 2016, 2017 and 2018.

For detecting seasonal variations in the seismic repose of the landslide mass, three sensors were installed on the Sobradinho landslide in a triangular geometry. In order to understand properly the effects of superficial deformation and effects of river erosion, these sensors cover northern, eastern and southern parts of landslide. The continuous data for the seasonal impact evaluation was divided into three acquisition campaigns (1) dry period from Julian day 308 to 311 of 2016, (2) intermediate from Julian day 101 to 105 of 2017 and (3) saturated period (say) from Julian day 344 to 350 of 2017.

### **2.6.2. AMBIENT NOISE INTERFEROMETRY PROCESSING**

The processing work-flows of noise interferometry vary from application to application. However, most commonly adopted processing schemes after preprocessing, are autocorrelation, cross-correlation or deconvolution that retrieved green functions from ambient seismic noise at a variety of temporal resolution (Czarny et al., 2016 and references there in). In first step the data originally recorded in REFTEK format is convert into SAC format to be used in further ambient noise analysis. Then the hourly records are merged into 24 hours records (natural scale). The ambient noise analysis is carried out in two stages as before the cross-correlation (preprocessing) and cross-correlation. The events of relatively higher amplitude effects the

results of ANI, the coherent source signal desired for ANI are provided by the signals of low amplitude. Therefore, the effects of high energy events are muted from the records and is achieved in pre-processing (Bensen et al., 2007).

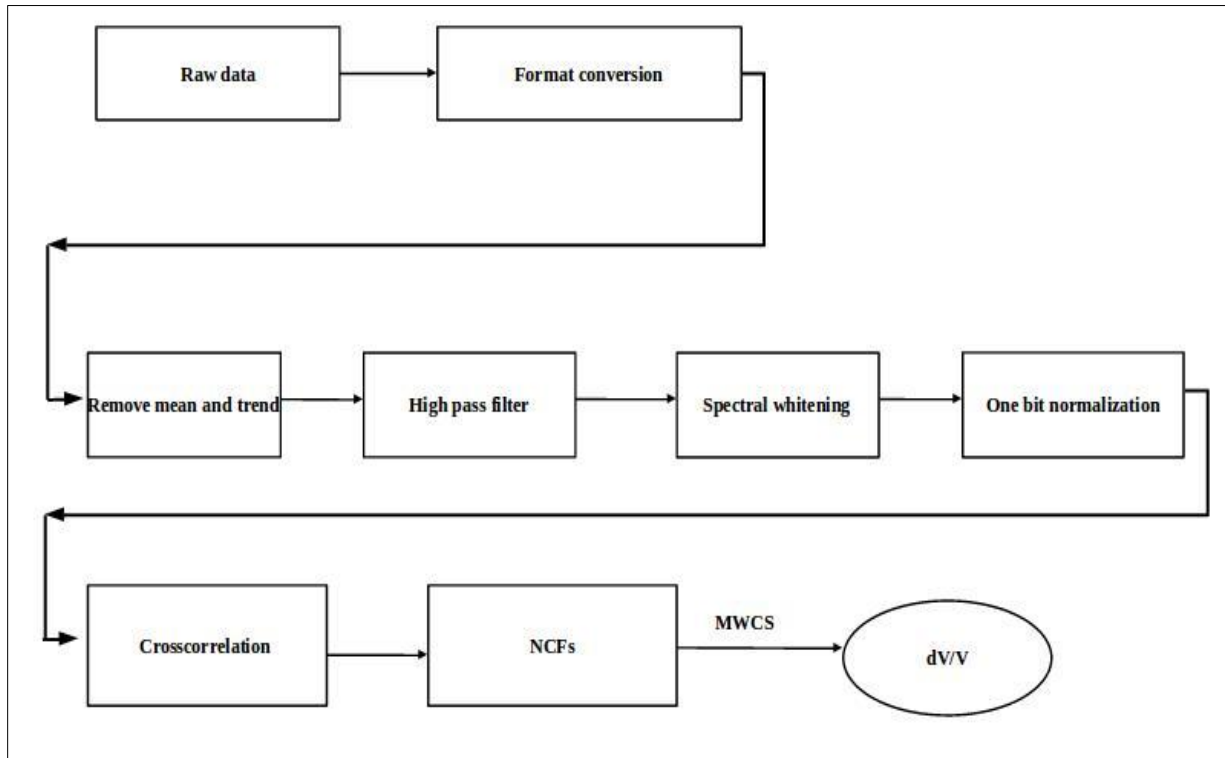


Figure 17 Ambient noise processing work-flow starting from Raw data and ends in the estimation of changes in relative velocity ( $dV/V$ ).

Following processing steps were carried out in pre-processing (Figure 17):

1. The mean and trend are removed from the data.
2. The data are high pass filtered.
3. Spectral whitening (flattening) is applied to reduce the effects of highly energetic frequencies in the records.
4. In order to further down-weight the contribution of high-energy arrivals which could obscure the lower amplitude ambient noise signal, a "one-bit" normalization is applied (Stehly et al., 2007): each data point is replaced with either a 1 or -1, depending on its sign, thereby removing amplitude information from the records completely. One-bit normalization is achieved by dividing each 24h record by their absolute value (Jonsdottir, 2018). A small segment of raw and preprocessed data is shown in Figure 18.

Same data acquisition system is used as for both experiments but in prototype normal slope experiment linear sensor array and an artificial source of surface wave placed at 30 m away from the sensor PL01 were used. The noise source lies in line with sensors array (Figure 1). Signals are studied in the frequency band of 2-24 Hz and 2-148 Hz at natural and normal slope experiment, respectively.

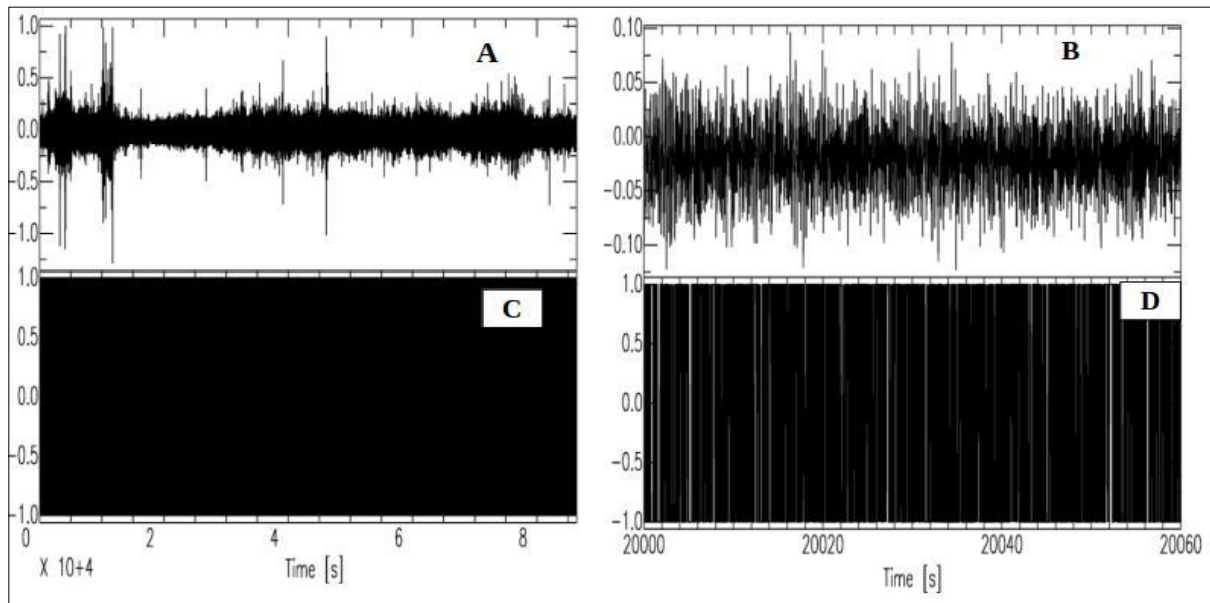


Figure 18 One hour record of ambient noise (A). Unprocessed trace is displayed after normalization (C). A segment of 30 sec around a transient event (B). Units in the figure are arbitrary.

### 2.6.2.1. COMPUTATION OF CROSS-CORRELATION FUNCTIONS

Cross-correlation functions (CCFs) of continuous waveforms of ambient noise are called correlograms. Correlograms are sensitive to velocity changes and can therefore be used to detect small velocity changes. Those can be used to infer stress changes or other changes of state that affect velocity. The cross-correlation of the random wavefield recorded at different positions in a free space, synthesizes theoretically the seismic energy at one locations if there had been an impulsive sources present at other location. This mechanism is true for any medium and response is given in terms of green function. It gives the effects of medium (between two sensors) on impulsive source using travel time and waveform information of all the phases (Wapenaar, 2004). The cross-correlation operation measures the wave similarity at different locations using travel time lag ( $\tau$ ) between the sensors. The cross-correlation of two signals  $a$  and  $b$ ,  $C_{a,b}$ , is a function of time lag, and is commonly defined as:

$$C_{a,b}(\tau) = \int u(t, a)u(t-\tau, b) dt \quad (1)$$

Where integration is performed over the length of the records, and  $u$  is the amplitude of a signal as a function of time. From (1),  $C_{a,b}$  is maximum when the sum of the products ‘ $u(t, a) \times u(t-\tau, b)$ ’ is at a maximum, meaning that  $a$  and  $b$  are most similar when  $b$  is shifted by that amount relative to  $a$  (Jonsdottir, 2018).

Table 4 The parameters used for  $dV/V$  estimation at normal slope as well as at landslide experiments.

Parameter Name	Description	Values Normal Slope	Sobradinho Landslide
analysis_duration	Duration of the analysis [s]	3 HRS	UTIL DAYS
cc_sampling_rate	Sampling rate for the cross-correlation [s]	(DELTA=0.001)	(DELTA=1.600000e-02)
resampling_method	Resampling method	SAC COMMAND	NONE
preprocess_lowpass	Preprocessing low-pass value [Hz]	80-112	2-24 Hz
preprocess_highpass	Preprocessing high-pass value [Hz]	112-150 Hz	2-24 Hz
maxlag	Maximum lag time [s]	0.6s	0.5 s
corr_duration	Data windows to correlate [s]	STACK 2s windows each 300s (5 min)	STACK 10s windows each 1800s (30 min)
overlap	Amount of overlap between data windows	0	0
windsorizing	Windsorizing at N times RMS	NONE	NONE
whitening	Whiten traces before cross-correlation	YES	YES
stack_method	Stacking method	SIMPLE	SIMPLE, SAC
components_to_compute	Components	Z	Z

In ANI cross correction is a central step that provides the travel times of seismic phases between two sensors. The signals recorded represent the same wave-field shifted in time that it takes to reach from one sensor to the second. Therefore the cross-correlation function contains a peak which corresponds to the travel time of wave-field between sensors.

After preprocessing the records were cross-correlated over an appropriate window length and results are stacked (Table 4). This computational step has a paramount importance in ANI. In order to retrieve Rayleigh wave whose particle motion is confined to vertical-radial plane, the cross-correlation at vertical (Z) component is computed first. The cross-correlations of all pair of stations (DF01 to DF02) for ZZ (vertical components), RR (radial components) and TT (transverse components) were obtained (Figure 3). The reverse interstation paths are not computed so that the cross-correlation order DF01-DF02 is performed but DF02-DF01 is not.

The late arrival or coda part of the correlogram can provide detailed information about the medium than the direct arrival. It is a scattered part of the wave-field that hits the medium several times travel a longer path and is rich in information (Fores et al., 2018).

#### **2.6.2.2. MOVING-WINDOW CROSS-SPECTRAL (MWCS) TECHNIQUE**

The MWCS was proposed by Poupinet et al. (1984) and was applied for the calculation of crustal velocities from micro earthquakes. The detailed description of method can be found in Clarke et al. (2011). It is the most adopted method for the calculation of changes in velocity in frequency domain.

The MWCS method is applied to the preprocessed reference (long term) and current CCFs which is divided into small window segments at different lag times. These segments are cosine tapered and mean adjusted and Fourier transformation is applied for calculation in frequency domain.

The phase differences between the two waveforms are used to estimate the time delays ( $dt$ ) between the two windowed cross-correlations and velocity of seismic propagation is assumed perturbed uniformly in the area in this way the time shift become constant and phases of cross spectrum will be linear (Clarke et al., 2011). Weighted linear regression is applied to bestfit the individual measurements and local time shift of cross-correlations ( $CCF_{ref}$  and  $CCF_{cur}$ ) is calculated from the slope. The CCFs coherences are the weights factor in regression.

### **3. RESULTS AND DISCUSSIONS**

#### **3.1. SITE CHARACTERIZATION**

##### **3.1.1. MASW AND ERT**

The fundamental and first higher mode (bimodal propagation) of Rayleigh waves are observed over the dispersion curves calculated over the three profiles (L1, L2, and L3). However, only fundamental mode of dispersion curve is used in the inversion because of the initial model cannot be well constrained from the stratigraphic information. It is also evident from the Figure 19 that after a certain frequency value, the phase velocity decreases with increase in frequency. White dots show the phase velocities interpreted at selected frequencies for the fundamental (used in the inversion) and first higher modes.

The inversion results are presented on 2D plots as contours of shear wave velocity (Figure 20). Results presented here have demonstrated that there are three layers over a homogeneous half space. The sections of 3 layers is considered with the only fundamental mode of dispersion curves, due to the stratigraphic profile of the area, which suggests a joint yellow to reddish clay, after joint Clay and Saprolite clayed, so transitional contact is the semispace. The densities are 1.2, 1.6 and 2 kg/cm<sup>3</sup>. The inversion starts with 300 m/s and ends at 700 m/s.

Shear wave velocities of layers obtained at profile L2 let us obtain a three layered subsoil model (260, 400 and 700 m/s), with the substratum at 20 m depth. These layers present a quite homogeneous layering in the subsurface. This profile runs over the area of alluvial deposit and these homogeneous layers prove the absence of structural disturbances in the strata up to 20 m depth. It is not possible to get subsurface information beyond this depth because of the total length of the profile. It is the rule of thumb that depth of investigation is half of the profile length. For the alluvium thickness estimation profiles with a large spread are recommended. However, it is interesting to note that a depth dependent variability of shear wave velocity keeps on rising with depth that shows the increase in rigidity with depth. This is due to the presence of less stiff clay than the overlying alluvial gravel. The upper layer has low seismic velocities and is quite homogeneous over the observed site. For example at the middle of profile L2, the velocity of the three layers as 280 m/s, 490 m/s and 520 m/s, respectively.

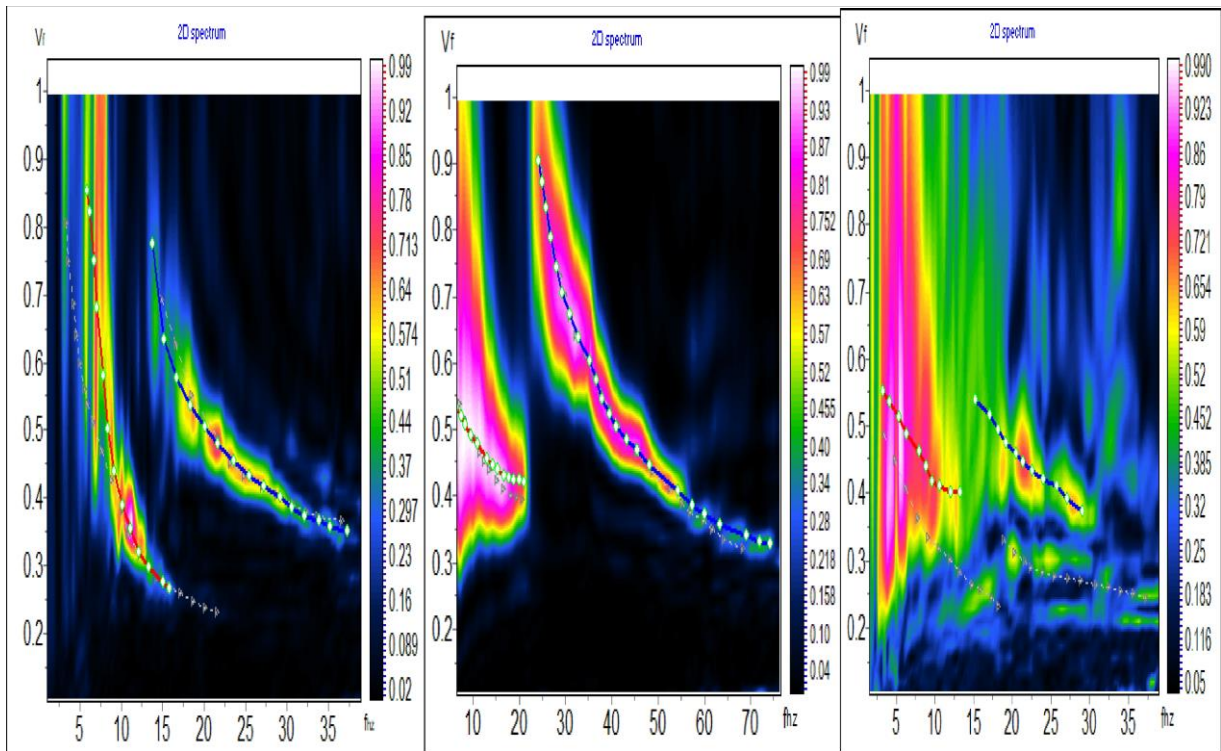


Figure 19 Velocity spectrum (Velocity vs Frequency) along with interpreted dispersion curves (solid lines) over three profiles (from left to right L1, L2, and L3). The color scale presents amplitude values.

At profile L3 that run parallel with the landslide body, following surface velocity layers are delineated on 2D shear wave velocity section with  $V_s$  values as 160 to 440 m/sec, 330 to 540 m/sec and 440 to 660 m/sec, respectively. The persistent depth dependent rise in the  $V_s$  is maintained here, however between distances 42 to 56, the region where profile passes through landslide scarp (crest), greater disturbance in subsurface layers are observed which may possibly be linked with the material deformation created by the onset of the landslide in the past.

The profile L1 that touched the landslide scarp at 65 to 80 m length show greater variations in the shear wave velocity over the landslide, where a decrease in the velocities of upper two layers is observed. Along with this decrease, there is an increase in velocity of the third layer, which may possibly be linked with the landslide slip surface.

These high values of  $V_s$  show that material is relatively stable in its dry state, however any change in soil stiffness created by the rainfall water can lead to the reactivation of landslide at the aforementioned impedance contrasts. From these layers it is difficult to identify landslide

limits. However, profile L3 shows large variations in Vs at the geophones lie at the landslide zone.

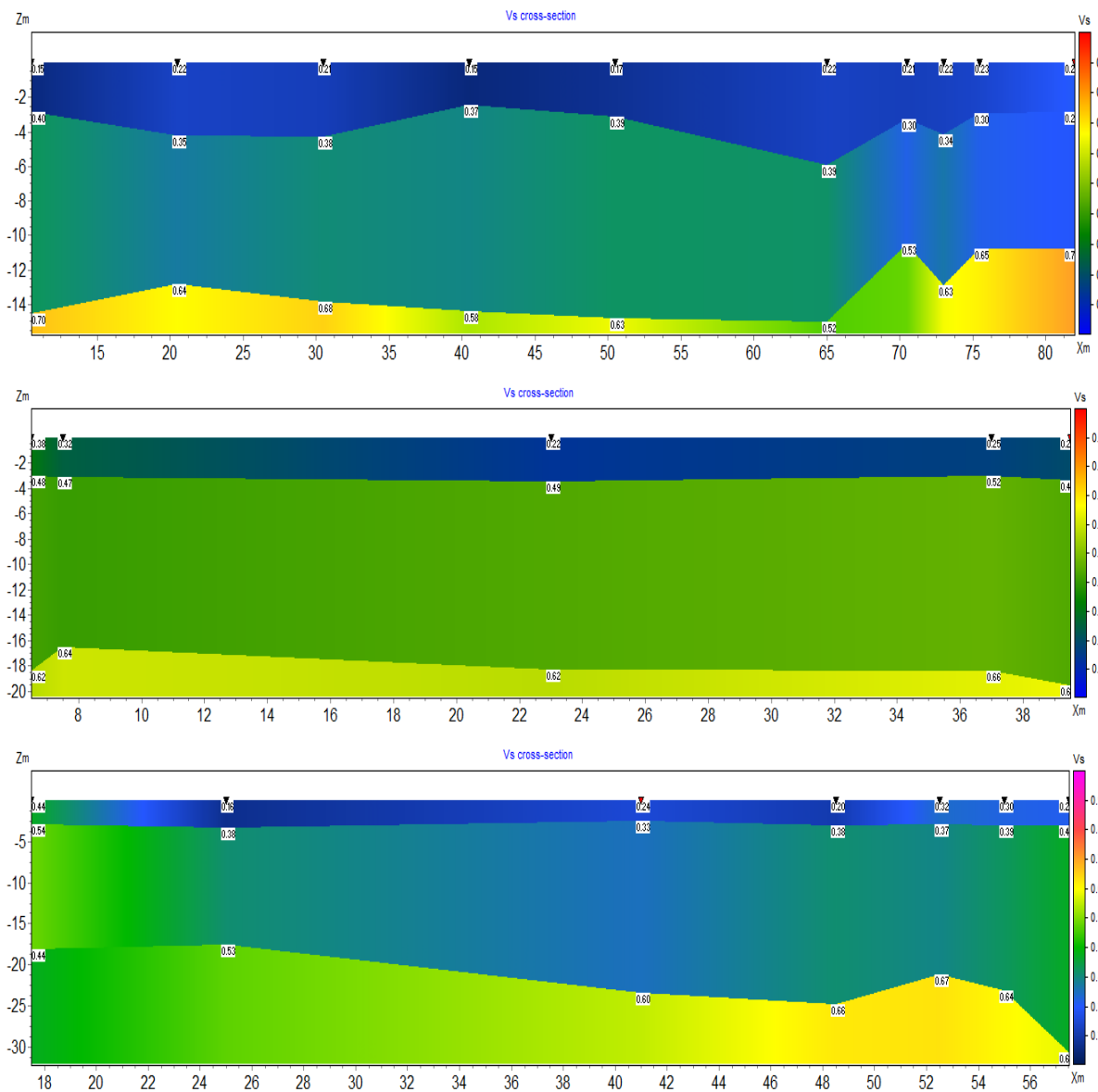


Figure 20 Results of MASW a 2D shear wave velocity profile of the area (L1 to L3 top to bottom). Color bars are the Vs velocities in km/sec

### 3.1.2. ELECTRICAL RESISTIVITY TOMOGRAPHY

Results of ERT profiles over Sobradinho landslide are plotted as apparent resistivity values at the top, best fit model in the middle and inverted resistivity (true resistivity) at the bottom. An apparent resistivity section is calculated from software and is compared with field apparent resistivity values. Then by comparison of these apparent resistivity values at a RMS error of 3.8 % the best fit resistivity model of substratum is obtained (Figure 21). At the beginning of

the profile above landslide scarp, low resistivity values are found that are related with disturbed material because of the presence of landslide which is also evident from the MASW analysis. As we move away from the landslide scarp over undisturbed material, different resistivity values are observed (Figure 21).

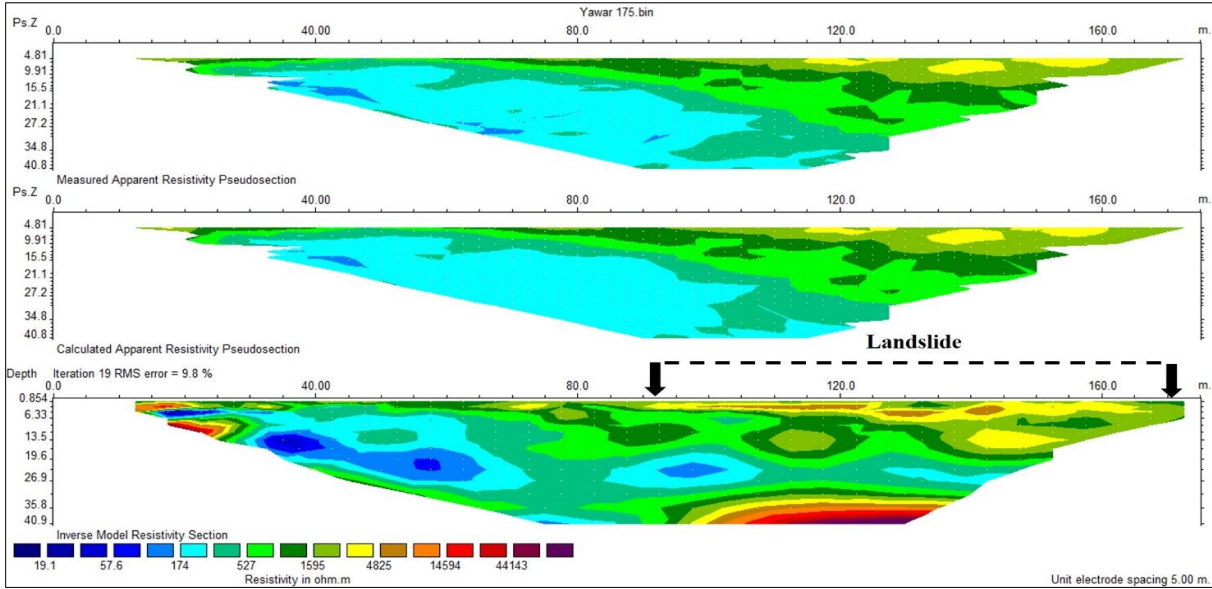


Figure 21 Inversion results of electrical resistivity tomography at Sobradinho landslide. The black dotted line shows landslide area which is zoomed in Figure 22.

On inverted resistivity section three materials are identified as upper high resistive, intermediate and lower resistivity. In zoomed image of the profile (Figure 22) that covers the landslide body, a continuous contrast between conductive and resistive materials is observed which could be associated with the presence of a sliding surface. The small scale discontinuities of intermediate resistivity materials are also delineated on the section. It is evident from resistivity values that the area consists of relatively coarse grained material, which may provide the pathways for the rainfall infiltrating water that may build pore water pressure in the landslide mass, a possible cause (trigger) of the reactivation of landslide in the case of some future extreme rainfall events. At the bottom, very low resistivity values are found that may possibly be related with fine grained water bearing strata (water table).

At the beginning of profile (away from landslide) a low resistivity zone is present (Figure 22) which could be linked with the presence of fine grain material having large amount water (possibly water table). However, the lateral extent and depth limit is not possible to analysis because of the shorter length of profile and because of the absence of the availability of any

bore hole near landslide area. The continuous resistivity material at the top throughout the landslide extent may possibly be linked with the presence of dry, disturb and coarser grain material.

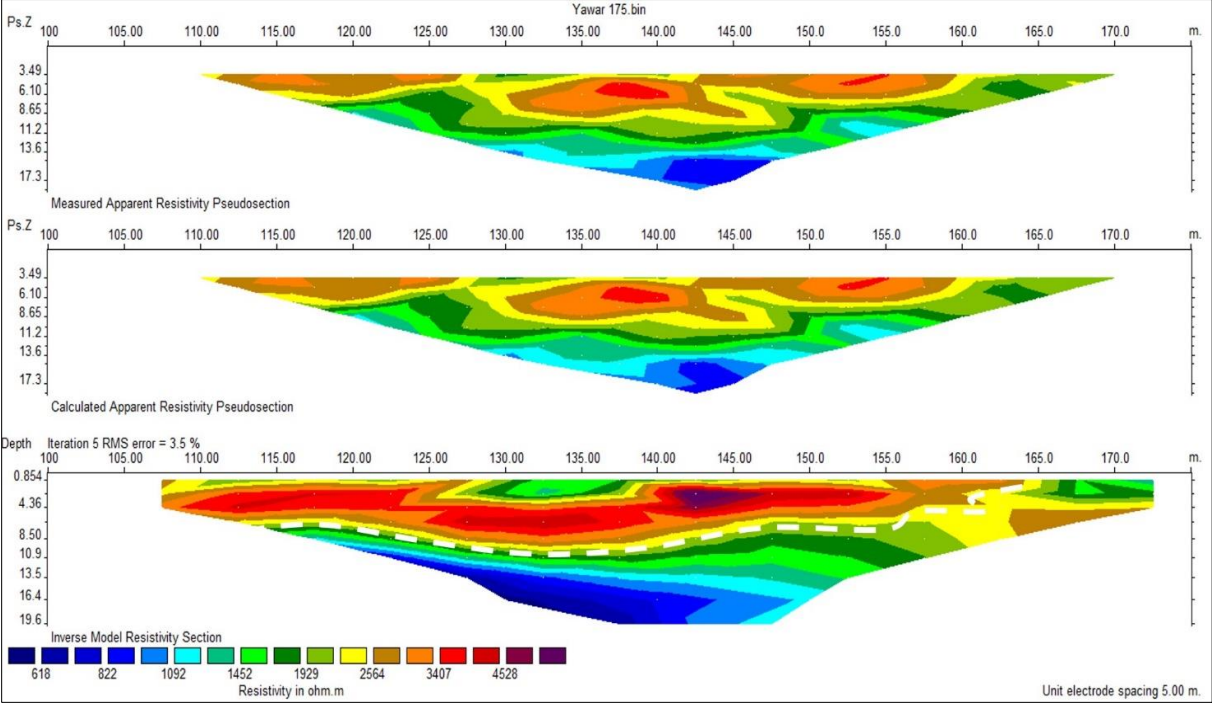


Figure 22 Zoomed image of the profile shown in Figure 21, which shows the subsurface structure of the landslide

On the profile that runs parallel with landslide provides information at greater depth. The upper high resistivity dry disturbed clay is also observed along the longitudinal direction which was also found at vertical profile. This zone is also present at the central portion of landslide at greater depth (17-26 m). In topsoil of landslide body, the resistivity is relatively high because of the presence of fine, deformed and dry martial. At the bottom of landslide very low resistivity values are found that are possibly related with the fine grained material having a large amount of soil moisture or because of the presence of water table. The high resistivity material at 35 m depth highlights the presence of the Saprolite layer. At a distance of 80 m from the origin of the profile, it is also possible to see the presence of another vertical discontinuity. The contrast between conductive and resistive material could be associated with the presence of a sliding surface. Inverted resistivity contours of the longitudinal profile are shown in Figure 23.

It is interesting to note that results of inversion model at the location where it passes through alluvial plain show horizontal continuity in resistivity variations (Figure 23). These results are

consistent with the shear wave velocity section obtained from MASW at profile L2 (Figure 7). This high resistivity material layer is consistent throughout the entire length of the profile L2 (280m), this validates results of previously held assumption that the sediments at the alluvial plain were deposited by the Captinga River (Braga et al., 2018). From this study, it is assumed that these sediments are the results of the erosion at the top. However, the consistency of this layer is broken at the landslide where a small discontinuities filled with high resistivity material are identified. This may possibly be related with the landslide activity. These permeable zones at the longitudinal boundary of landslide may possibly provide the pathways for the rainfall infiltration water to reach the landslide that may build static pore pressure a threat to the reactivation of shallow clay-rich Brazilian landslide under extreme rainfall event.

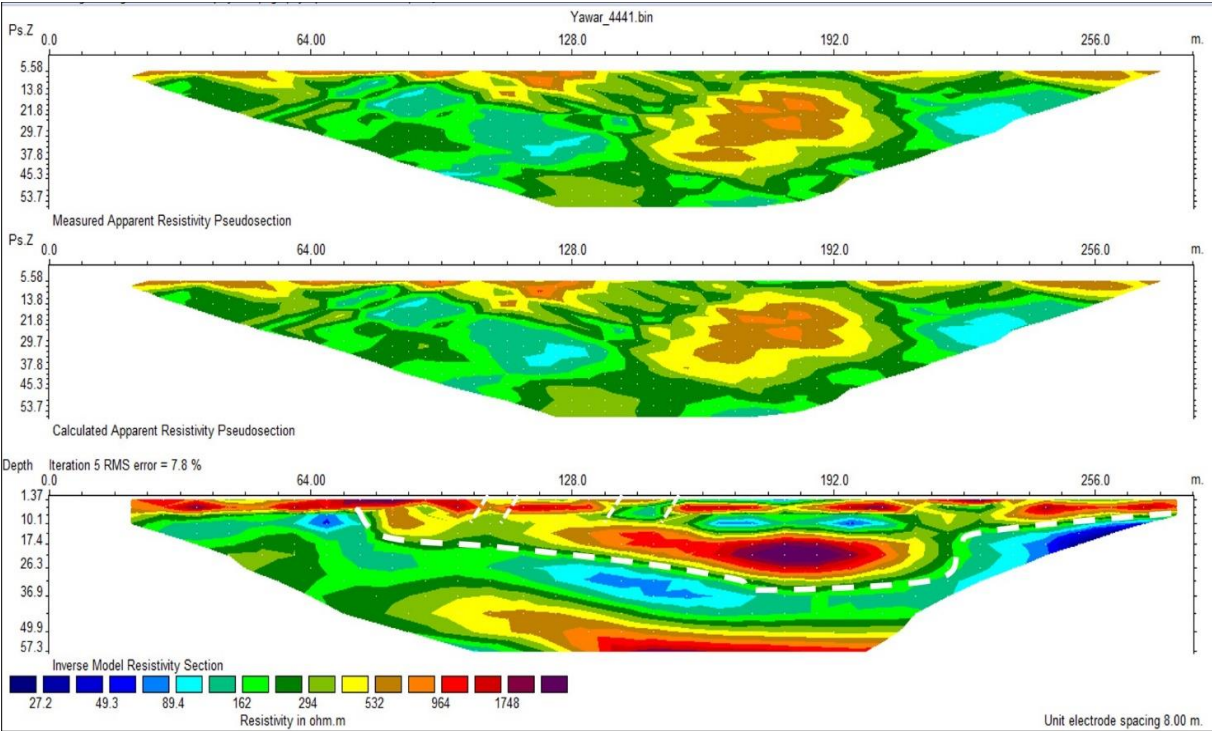


Figure 23 Longitudinal profile of length 280m taken along the landslide.

### 3.2. NOISE CHARACTERIZATION

#### 3.2.1. SPD AND PDF

An example of 1-d-long records from station S1 reveals large temporal variations of the seismic noise (Figure 24). The time-frequency series can be divided into three main phases (A, B, C) based on noise energy: phase A corresponds to low frequency (less than 2 Hz), phase B to the intermediate frequency range 2-10 Hz, and phase C a high frequency (greater than 10 Hz) noise. Second band (B) is observed at frequency range 2-10 Hz where the energy of noise fluctuates

greatly. Noise characteristics of band B show clear variations with the day-night periodicity and can be linked with the cultural activities near the site. The main observed cultural activities are workers at the farm, working of electrical motor, activities of cows in the farm, mining activities (workers, rockfall, trucks) and villages (Rua da Matto) near the experimental site. These estimations are poor at frequencies less than 2 Hz due to sensor's natural response. At frequencies, larger than 10 Hz results are noisy.

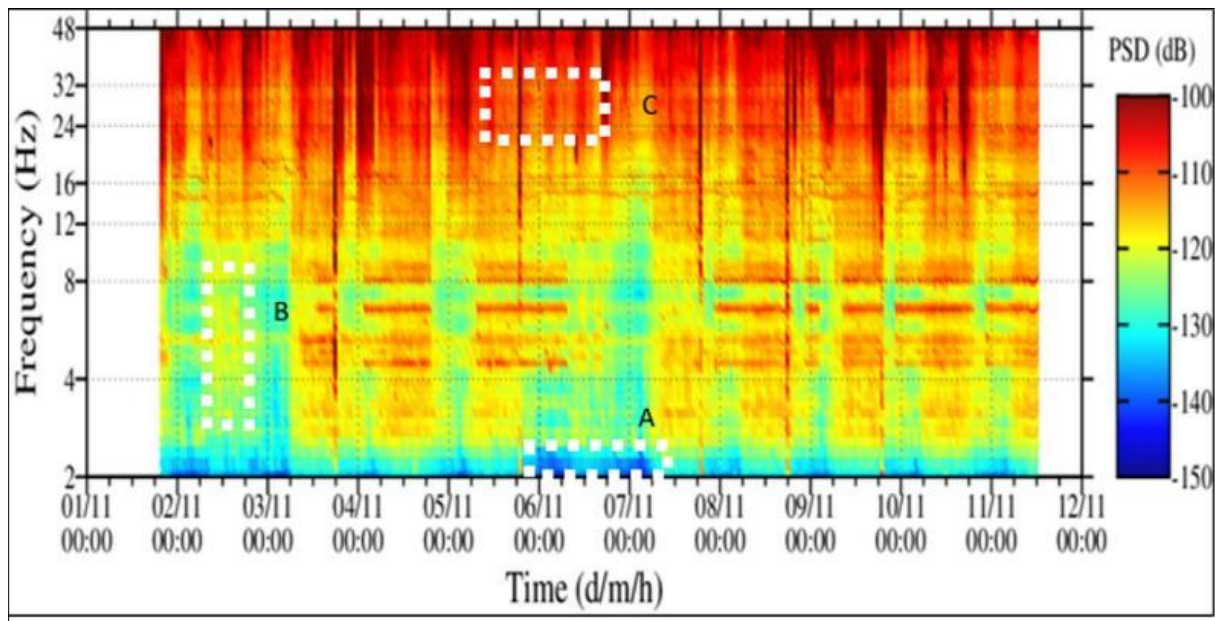


Figure 24 Time-frequency plot of PSD variations for S1. Color bar presents energy levels in decibels [dB] relative to the velocity ( $10 \log_{10} [(m/s)^2 / Hz]$ ). Dashed white squares indicate different phases of noise energy.

The PDFs are calculated from PSDs and then Peterson's New High Noise Model (NHNM) and New Low Noise Model (NLNM) have been plotted for comparison (Figure 25). Results showed that PSD of vertical components are different from zeros as well as they lie well between Peterson curves. We observe that the noise below 12 Hz is continuously being generated. According to Peterson, (1993) the noise level should be at least 20 dB less than NHNM at a frequency range of 1 to 20 Hz. There are very little variations on the noise recorded at E-W and N-S components which are because of tilting of sensors and are related to installation problem as well as some meteorological factors like wind and rainfall effects. The first peak of micrometer is related to sensor's natural frequency response. The second peak is observed above 2 Hz on the statistical model of environmental noise where energy levels with high probabilities are observed that never reach the NHNM. The noise at S8 has high energy than

S1 while probability decreases at higher frequencies. The noise probabilities of both stations never reach NHNM (Figure 25).

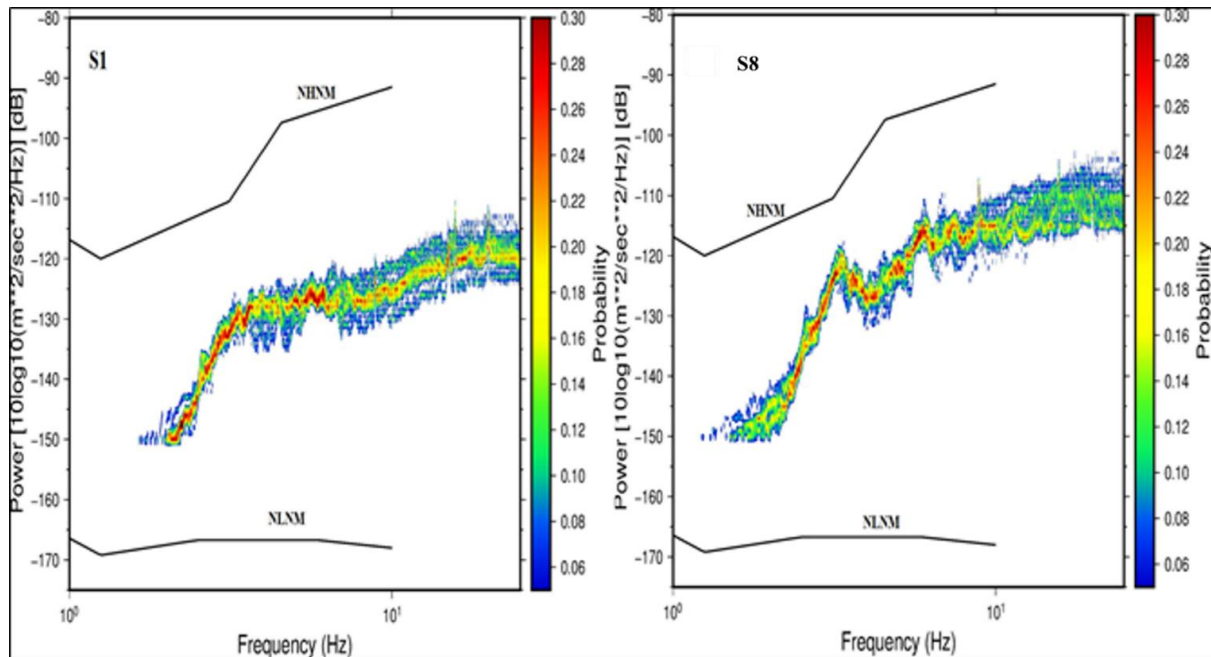


Figure 25 PDF of vertical component of S1 (inside) and S8 (outside) the Sobradinho landslide.

### 3.2.2. FREQUENCY-WAVENUMBER

In order to explore the incoming field wave, we applied f-k analysis to the seismic array in 5 seconds time windows on one hour long seismic noise. In Figure 26 we observe that ambient noise between 2.5 and 3.5 Hz having velocities close to 1700 m/s, however, around 4 Hz it is not possible to define a velocity continuity. Between 4 and 16 Hz velocity values vary between 500 and 1500 m/s, but these values do not decrease as a function of the frequency, indicating the absence of surface waves. These waves are attenuated while passing through a highly deformed material (tropical clay) of mass movement. We observe that between 5 and 16 Hz the incoming wave-field arrive at 260 degrees. At 260 degree the prominent sources of noise are farm and village Rua do Matto. We observe that east-west (E-W) components show a more stable behavior for phase velocity value; higher values at low frequencies and lower values at high frequencies. Backazimuth values are interesting between 4 and 8 Hz, which arrives from 260 degrees of azimuth.

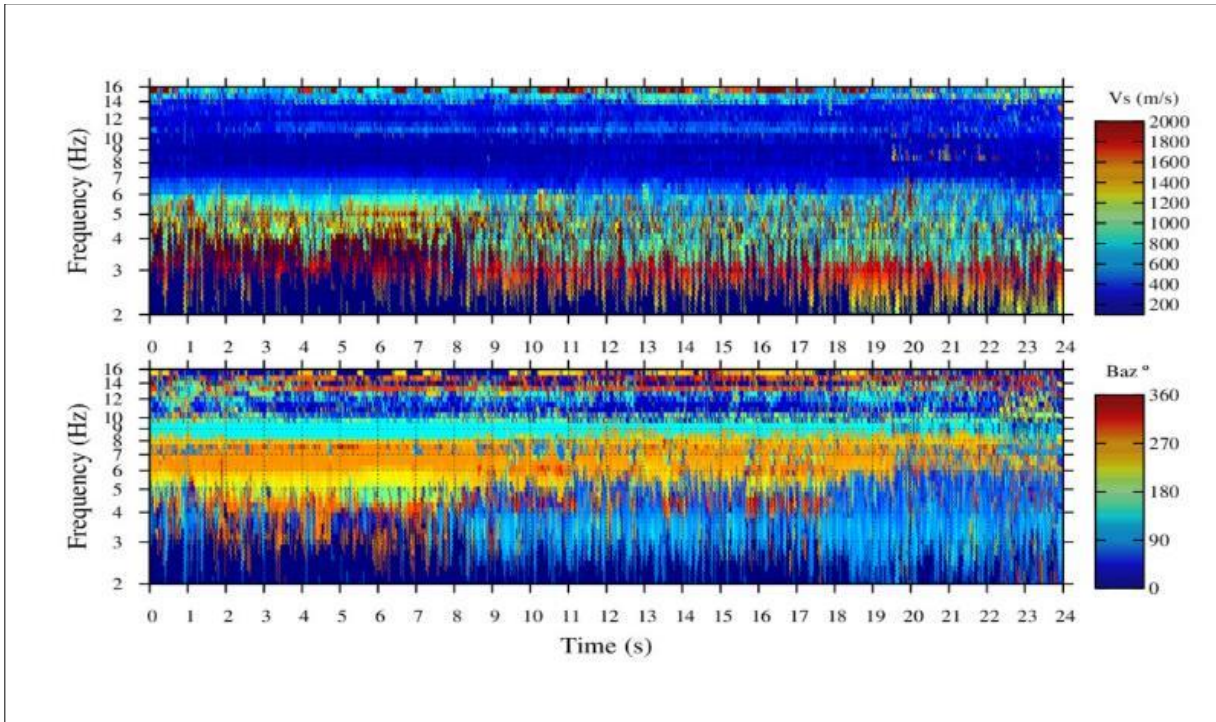


Figure 26 The f-k analysis of E-W component, results as a function of the velocity (top), and results as a function of the backazimuth (bottom).

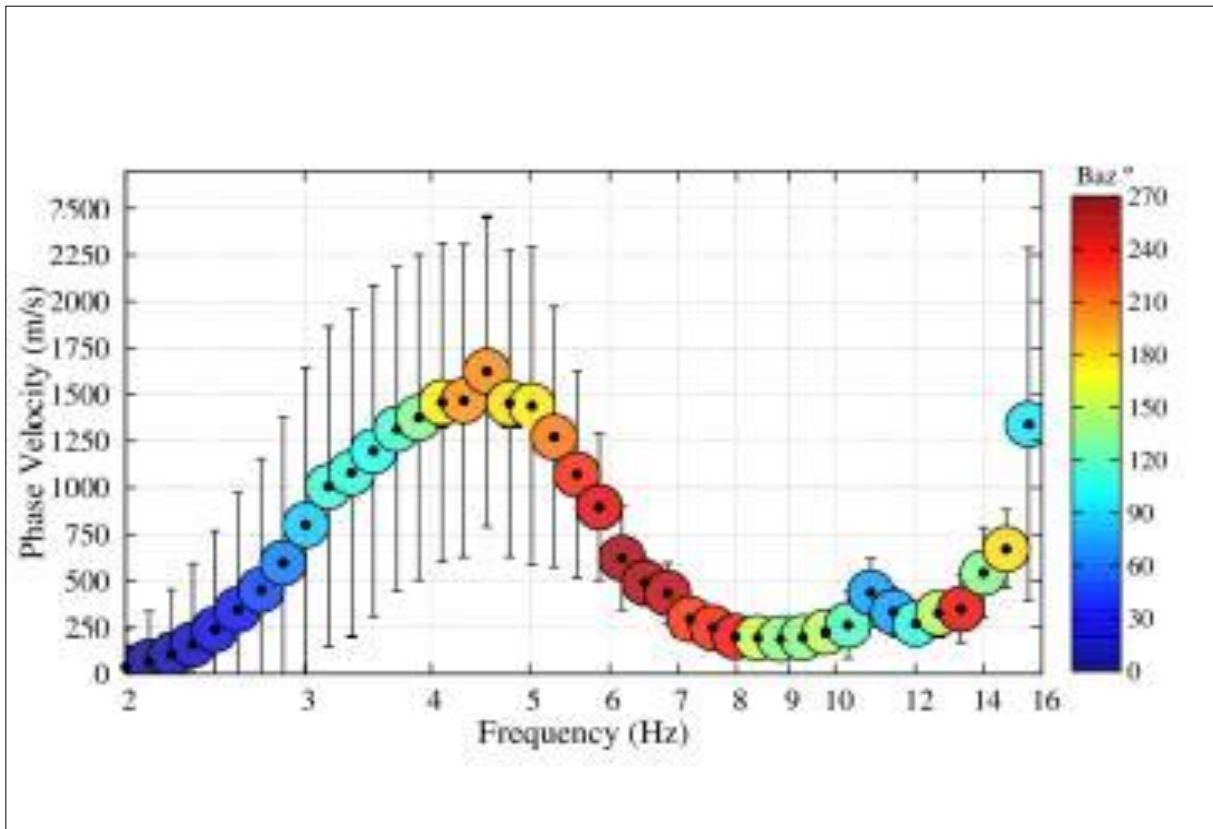


Figure 27 Dispersion of recorded noise wave field of Julian day 307. After 7 Hz there are little variations in phase velocity of wave with frequency.

In Figure 27 average velocity values along 1 hr time windows for each frequency are given. A large dispersion is observed before 5 Hz. Between 5 to 16 Hz the incoming wavefield comes from 260 degrees, but is not possible to obtain a dispersion curve. So the dispersion characteristics (phase velocity vs frequency) of surface become invisible after 6 Hz. Below 2 Hz there is no data of frequency response of the seismometers. The result indicates that incoming noise wave could compose of body waves at frequencies greater than 7 Hz.

### **3.3. JOINT INVERSION**

In Sobradinho landslide, the geology of the area is not changing much. HVSR spectral ratios at eight stations exhibit the same form and the site frequency is 2 Hz with relative amplification of 7, indicating that under these stations the subsoil structures are very similar. Figure 28 shows a common HVSR ratio where we can see a well define curve that could be related to ellipticity of surface waves. The peak shows that basement lies at relatively greater depth. The fundamental Rayleigh mode associated with the profiles of Figure 29 is very close to the experimental one and is good in common frequency range. If this is the case, the subsoil structure represents a potential landslide risk.

In order to establish a subsoil model that could explain the elastic characteristics related to soft soils, we have derived a dispersion curve by mean of f-k analysis using all array stations for the three ground motion components. For this, we use 5 seconds time windows along one hour of seismic noise. In Figure 29 phase velocities values of one hour time windows for frequency range (5-10 Hz) are given for E-W component. A large dispersion is observed between 5-6 Hz frequency ranges where the incoming wave-field comes from 260 degrees. At frequency of 5 Hz the phase velocity is 1400 m/s which is reduced to 200 m/s at 8 Hz. Below 2 Hz the information is not reliable because of the frequency response of the seismometers used for the analysis or small array aperture. Results for other components do not exhibit robust curves.

The curves of the spectral and dispersion ratios suggest that it is possible to carry out a joint inversion following HV-INV software guidelines. For the inversion, we start with a four-layered model of constant wave velocity, VS, VP, and density values. In the Figures 28 and 29 we have included the best fit to experimental curves after using several approximations. We can observe a reasonable fit between model and experimental results in all frequency range, which indicates that fundamental Rayleigh mode dominates the ambient seismic noise.

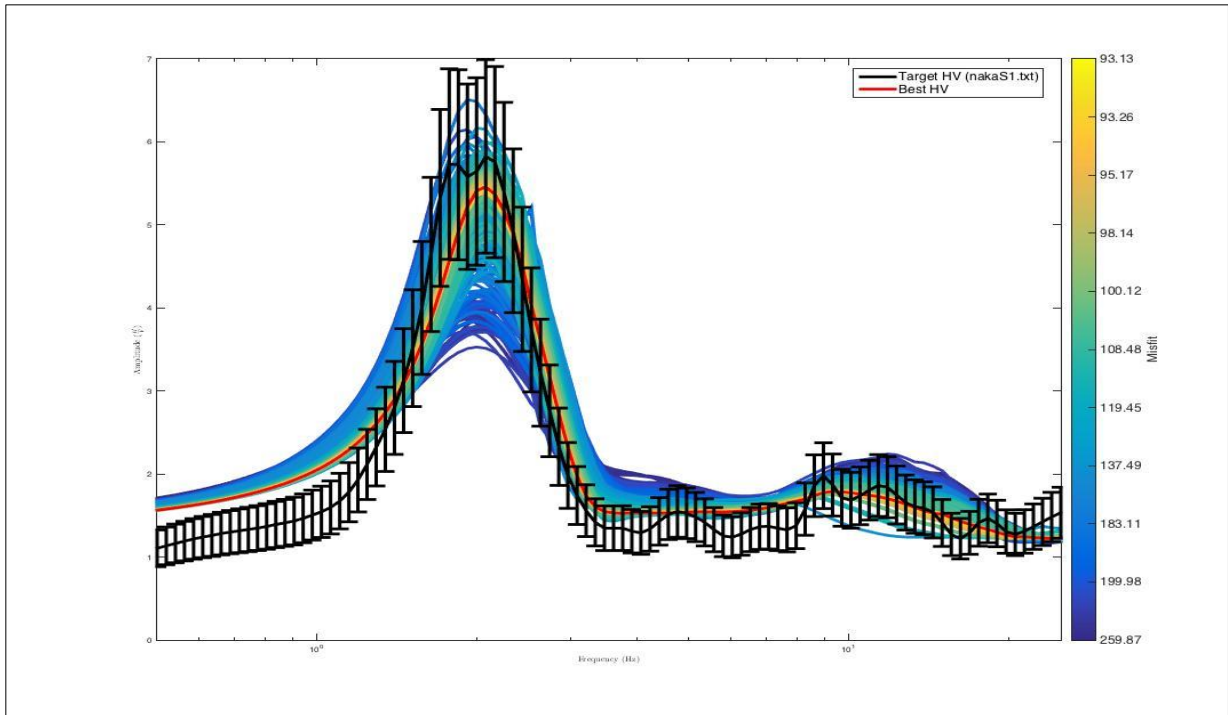


Figure 28 HVSR curve at S1 station (black line) and its standard deviation, and set of solutions (color lines) of joint inversion results. The best fit curve is the red color line. Bar scale color indicates the best misfit curves to experimental HVSR curve.

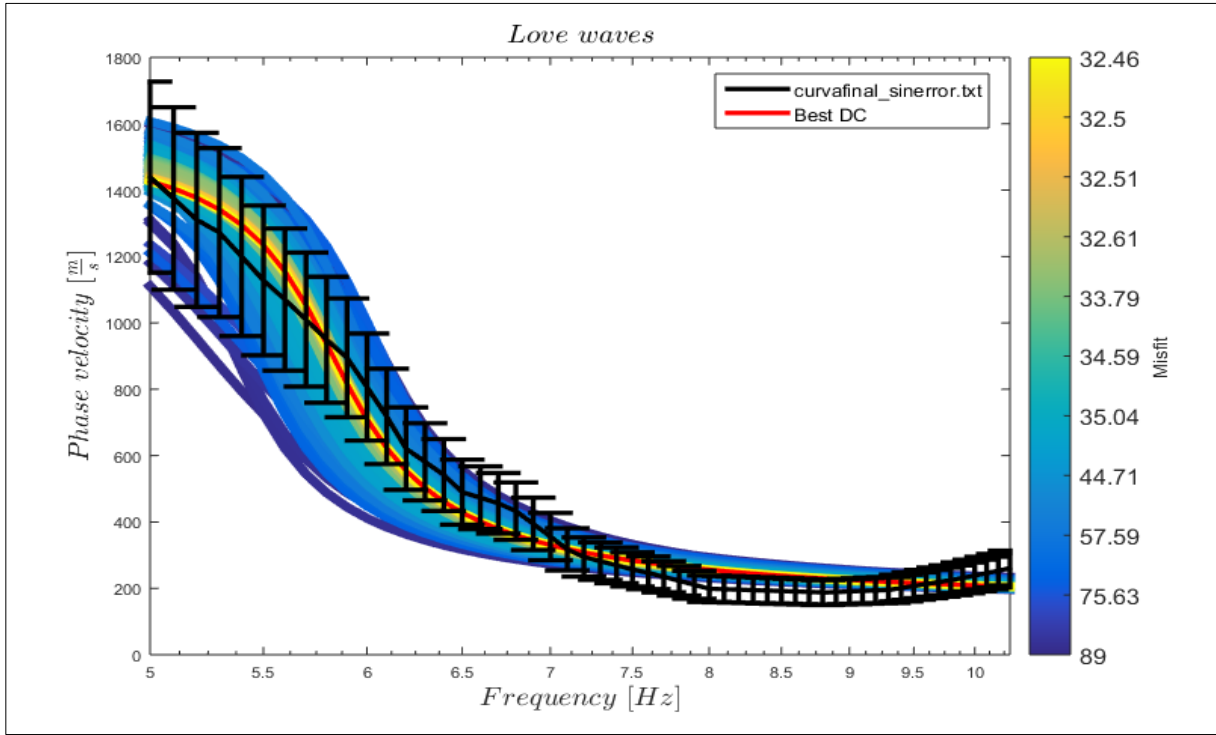


Figure 29 Set of solutions (color lines) of joint inversion results for f-k dispersion curve (black line). The bestfit curve is the red color line. Bar scale color indicates the best misfit curves to experimental HVSR curve.

In the Figure 30, we show a final model and besides  $V_s$  and  $V_p$  density structures are also resolved. These parameters are important in the interpretation of landslide characteristics. The interfaces (probable slip surfaces) lie at 7, 12 and 24 m depth. The depth of bedrock for  $V_s$  model is found at 24 m depth in the area (Figure 30). As slip surfaces may generate shear wave velocity contrasts. These layers have different rigidity values that give rise in the variations of observed seismic characteristics. The changes in rheology at these interfaces may results in the reactivation of landslide at the extinct slip surface or at a new slip surface developed at the other material interfaces.

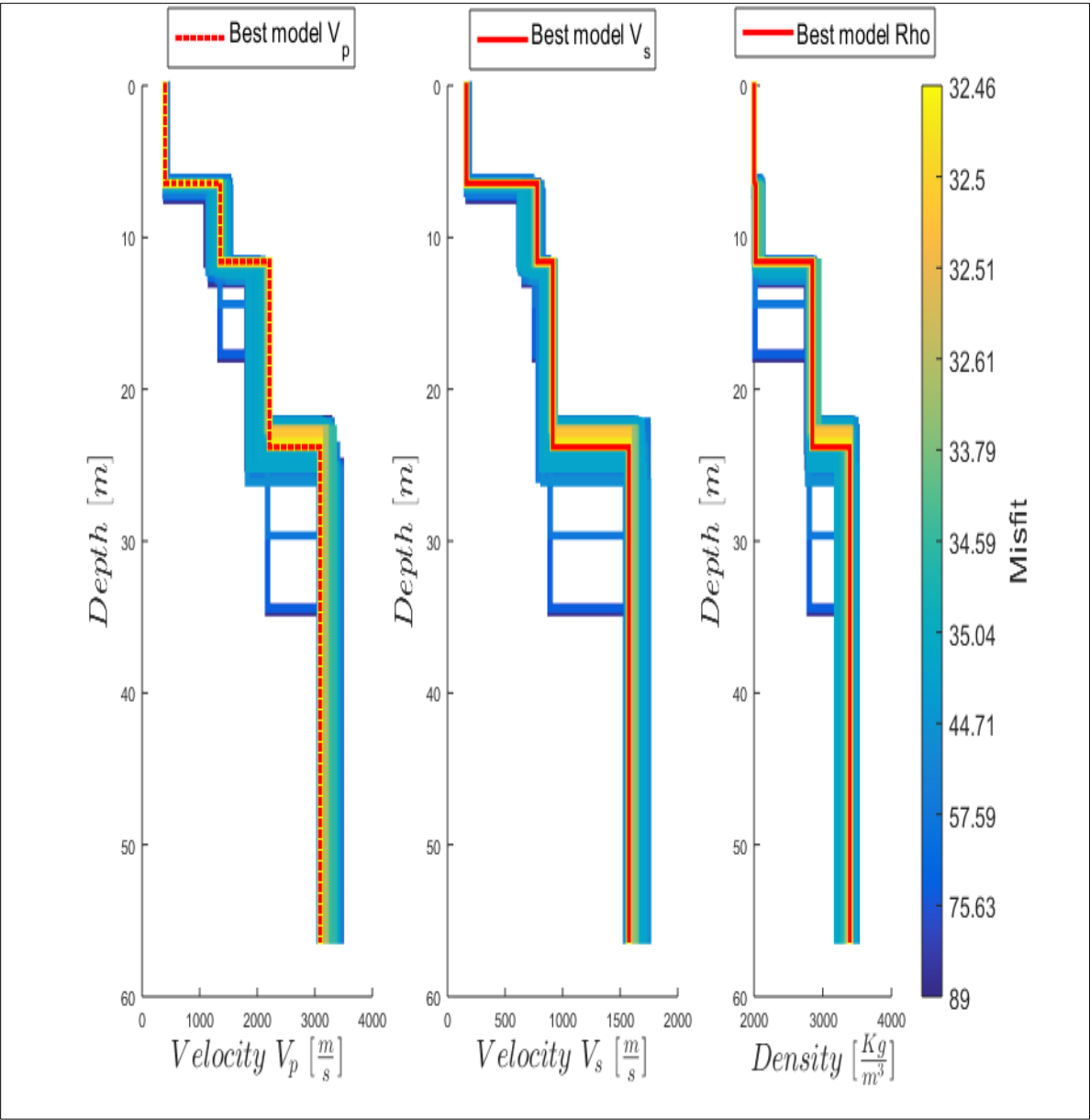


Figure 30 Set of solutions (color lines) of joint inversion results for final subsoil models. The bestfit curve is the red color line. Bar scale color indicates the misfit curves to experimental HVSR curve.

The following Vs based stratigraphic model (probable slip surfaces) is developed to explain the subsurface geophysical characteristics:

- An upper zone of highly fractured material with low seismic velocity (0 to 8 m depth)
- A middle zone with increased stiffness, from 8 to 12 m depth having a higher seismic velocities, which is another probable slip surface of landslide then a layered from 12 to 24 which is a stratigraphic interface between landslide mass and substratum. Through the inverted Vs velocity value are higher (at 8 m ~1000 m/s), they can generate a possibly shear surface for the occurrence of landslide.
- And bedrock corresponds to the elastic half-space.

### **3.4. HVSR**

#### **3.4.1. FIELD SCALE EXPERIMENT**

Results of prototype experiment show two peaks on HVSR curves, first at 5 Hz and second at 32 Hz. Both peaks show variations in their amplitudes with the increase of applied load however, in the present study only variations in secondary peak are considered (shallower). We assume that this peak is related with the depth that is less than 10m, which is more appropriate for the analysis of target depth (the region where tip of pile lies and stress is transferred to the soil). The first frequency peak is too deep to be used for any reliable interpretation according to the pile loading distributions in the subsurface as mentioned in geotechnical engineering literature. The prominent secondary peak between 30 and 35 Hz would be related to a large impedance contrast within the subsurface shallow layers indicating significant differences in compaction (because of microfractures) achieved with applied loading. Results show that with every rise in applied stress the amplitude of respective HVSR curve decrease a little (Figure 31).

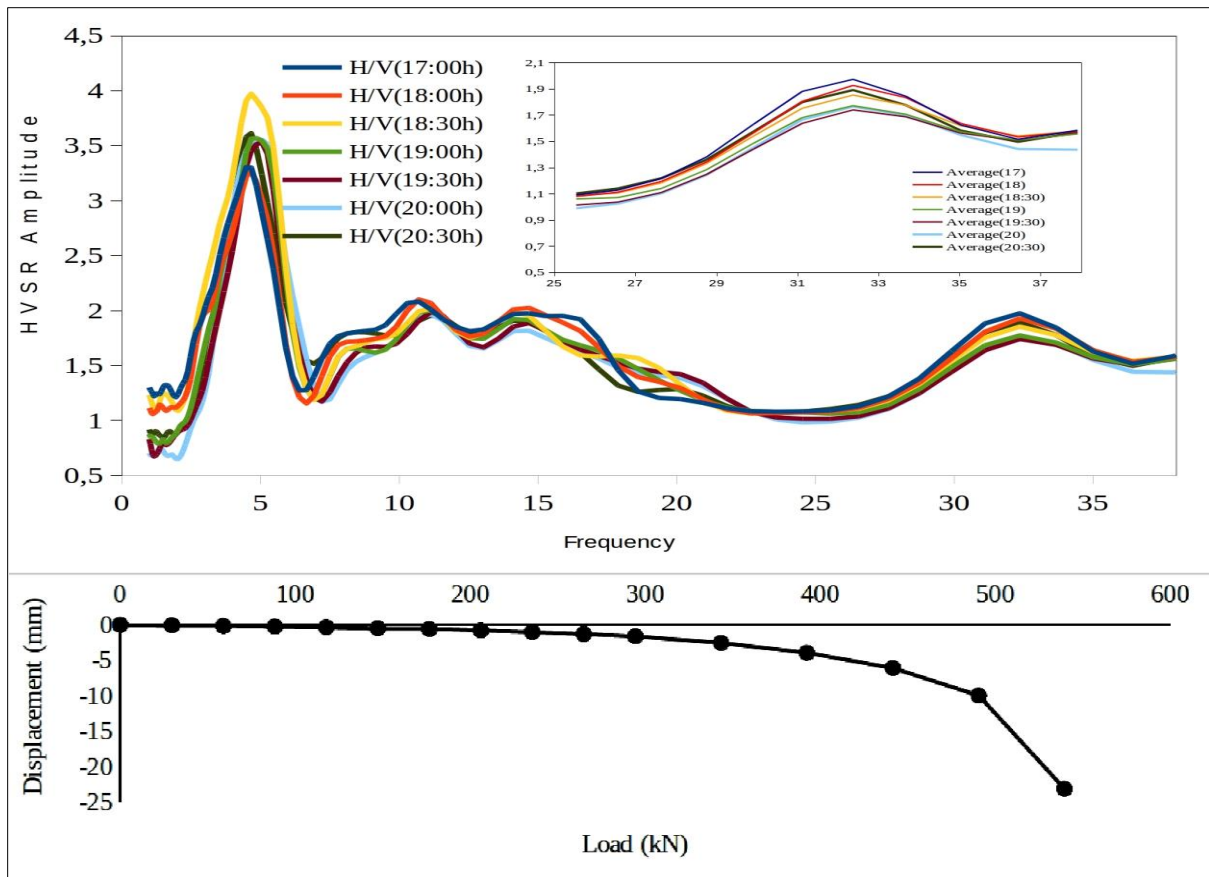


Figure 31 The HVSR curves produced at each loading episode. The Zoomed image second peak is shown in the box. The load displacement curve is also shown (below).

### 3.4.2. UBIQUITOUS FREQUENCY

This ubiquitous frequency is the frequency of Saprolite soft layer over the seismic bedrock and is independent of the landslide body and so is the same both inside as well as outside the landslide. It is also not affected by the seasonal variations (stiffness) produced by meteorological changes (degree of saturation). However, there are slight variations in peak amplitude (Figure 32 and 33) that can be linked with the seasonal variations in the stiffness at the slip surface. Previous studies have shown a direct link between the impedance contrasts and amplitude of HVSR curve, i.e. higher the impedance contrast (product of shear velocity and soil density) higher the amplitude (Stanko et al., 2017). One possible cause of higher amplitudes at one point and lesser at the other is because of the presence of ground cracks that provide permeable paths to rainfall infiltrating water and thus decreases the HVSR amplitude. This mechanism will reduce the shear wave velocity of propagation waves through reduced stiffness of landslide mass. As the amplitude of HVSR is a function of impedance contrast is the product of velocity and density (Stanko et al., 2017). The geometrical similarities of the curves reveal

that the frequencies present in each signal are similar. However, the stress variations that lead to reactivation of landslide in natural environmental conditions is very low as compared to the applied load in the prototype experiment.

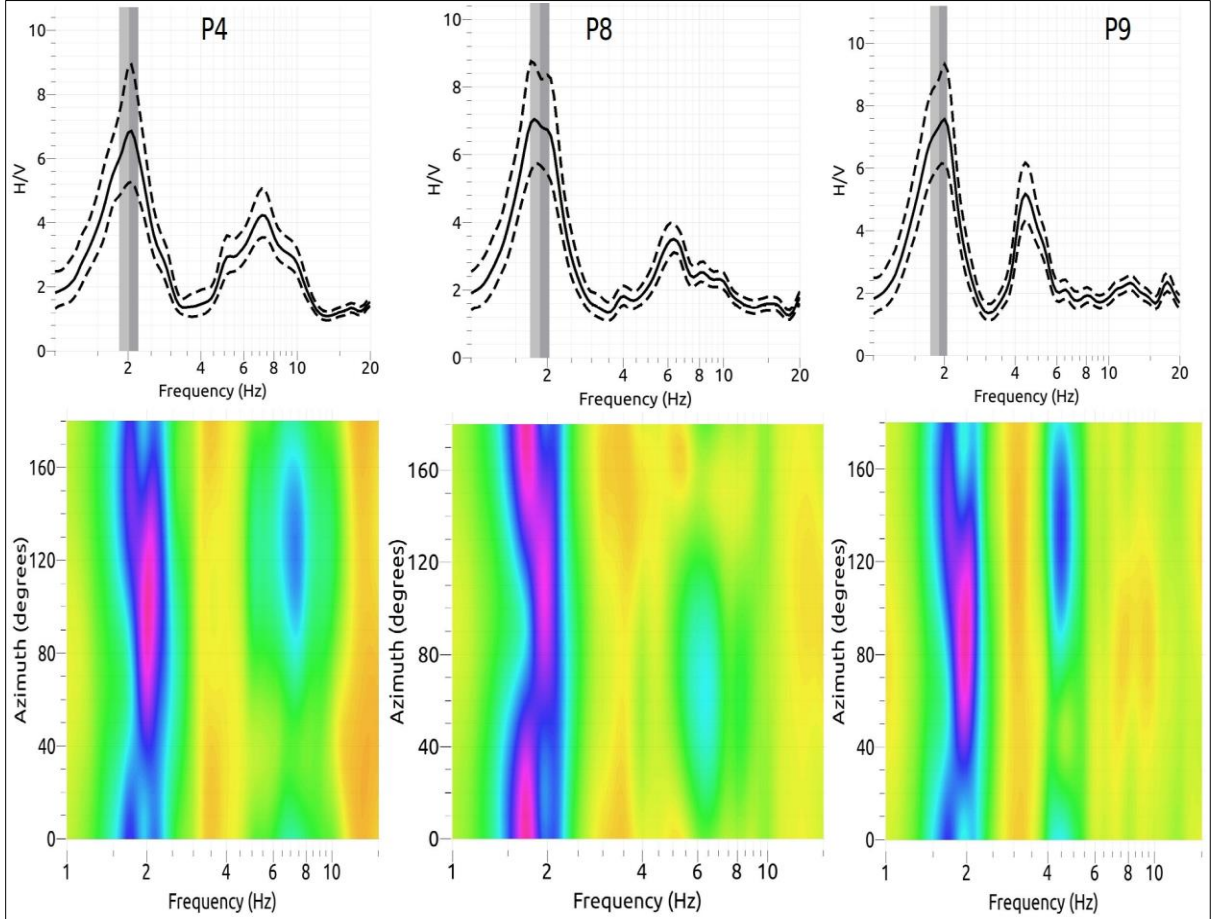


Figure 32 HVSR curves class A, peaks at 2 Hz and 4-6 Hz. The two dashed lines represent the HVSR standard deviation, while the gray areas represent the peak frequency standard deviation, which quantifies the experimental error associated with the average peak frequency value. Below is results of spectrum rotate at each point, y-axis is azimuth in degree and x-axis is the frequency.

The directional HVSR plot represents the projection of HVSR along different directions, from 0° to 180° in a clockwise direction. 0° stands for the north direction marked on seismometer and 180° stands for South (from 0° to 360° results are symmetric). The amplitude variations of the HVSR along with azimuth are found over the landslide mass mainly because of the presence of fractures and cracks that lead to trap seismic energy at a particular direction (azimuth). These are related with the surface alteration done by the erosional effects of underlying rivers while the sources of noise around the area were more or lesser uniform.

### **3.4.3. LANDSLIDE FREQUENCY**

There is not a single frequency which characterizes the landslide mass due to the presence of detached soil blocks mainly because of the seasonal erosion of the Capetinga River flowing at the bottom. Each soil block has its own degree of freedom and has different resonance frequency from these frequencies the time period of that particular soil block can be calculated as an inverse of frequency. The relative low amplitude is observed on the secondary peak mainly related with the presence of thin and soft soil cover (Stanko et al., 2017).

In Figure 32 and 33 along with a high amplitude stratigraphic peak, there are peaks at higher frequencies having low amplitudes which presumably indicate the presence of shallower velocity boundaries within the sediments that has also been observed in previous studies (Micromed, 2007; Gosar and Lenort, 2010). The amplitude of these side peaks is in most cases considerably lower than the amplitude of the main peak; only at station P5 and P11 the amplitudes are comparable to the stratigraphic peak. This confirms that impedance contrasts within sediments are much smaller compared to the contrast with the bedrock. One possible reason of this low amplitude of secondary peak may be the presence of coarse grains material (conglomerate) that reduces the impedance contrast of shallow depth layer. The presence of coarse grain material was also evident from the GPR profile taken at the base of landslide (Personal communication, Nunes). This has also been reported in previous studies (Gosar et al., 2010).

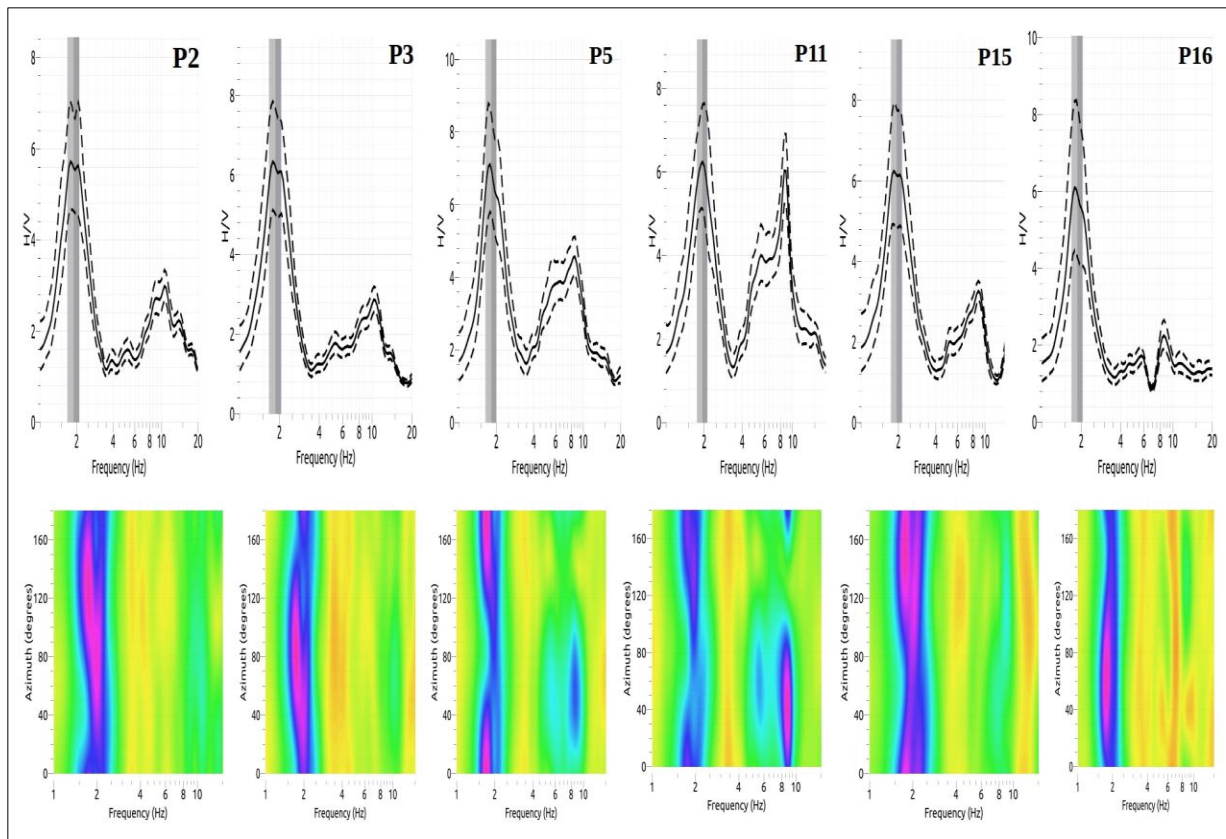


Figure 33 HVSR curves of class B, peaks at 2 Hz and 8-10 Hz. The two dashed lines represent the HVSR standard deviation, while the gray areas represent the peak frequency standard deviation, which quantifies the experimental error associated with the average peak frequency value. Below is the results of spectrum rotate at each point, y-axis is azimuth in degree and x-axis is the frequency.

### 3.4.4. FLAT HVSR

This class of HVSR curves lack any frequency peak according to reliability criteria of clear peak. There are two possible reasons for the absence of peak on HVSR curves (1) bedrock are exposed, (2) error in data acquisition. First row in the Figure 34 shows the problem of data recording while other three rows are observed in the areas behind landslide mass constituent of an alluvial geomorphological unit. At row three and four, higher frequency peaks started to appear (high standard deviation) as we move toward landslide. In the last row, the secondary peak also appears with very low amplitudes because of the presence of coarser grain material towards floodplain of river that lie behind the landslide. The effects of coarser grain material on HVSR amplitude was also associated with the results of Gospar et al. (2010).

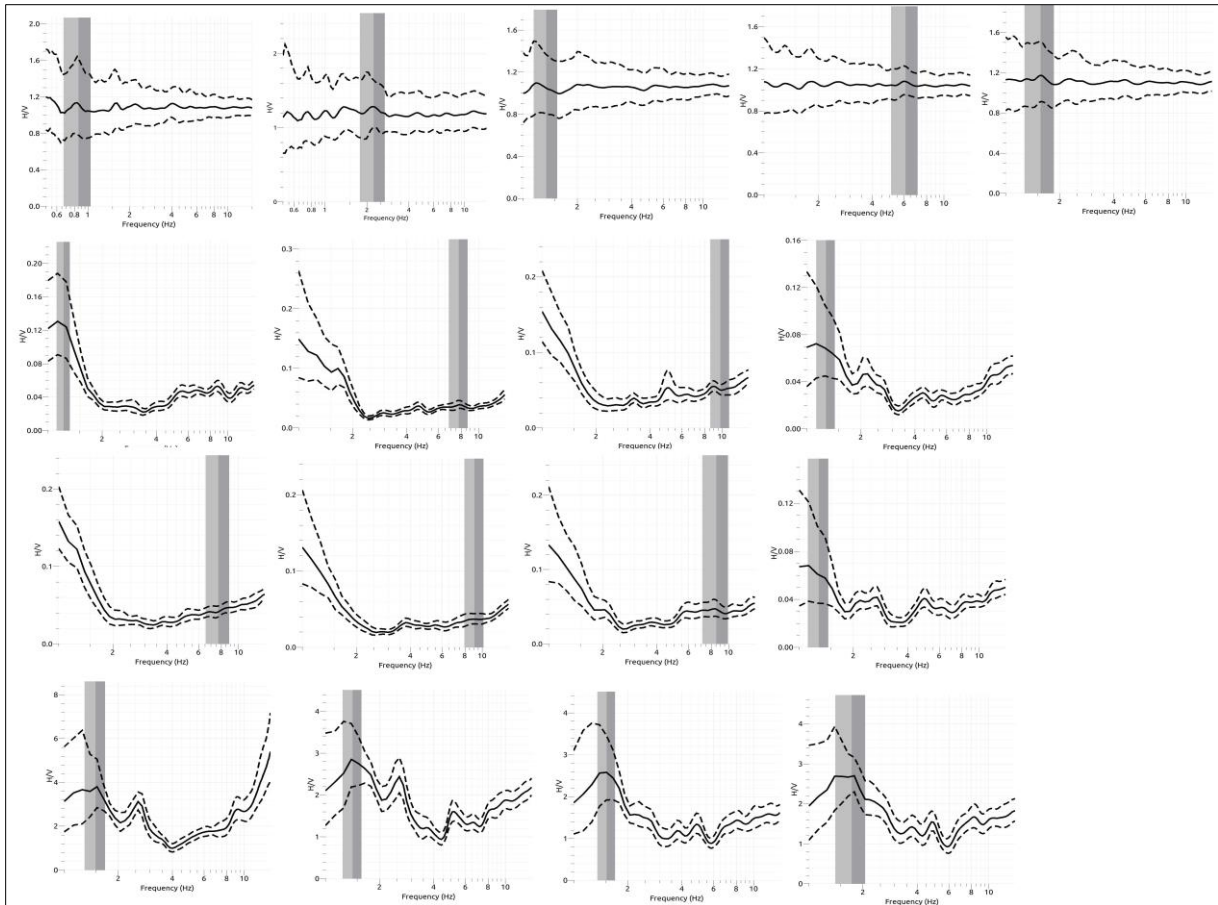


Figure 34 Class C, no peak/flat response of the strata on the HVSR curves. Dotted lines are HVSR standard deviation, while the gray areas represent the peak frequency standard deviation, which quantifies the experimental error associated with the average peak frequency value.

**3.4.5. SEASONAL ANALYSIS**

Three points were selected in the landslide mass (DF01, DF02 and DF03) for the observation of the seasonal impacts of the rainfall induced changes in the landslide mass. The entire acquisition period is divided into three periods based on the presence or absence of rainfall events. However, no attempt has been made for the quantification of the degree of saturation in the soil.

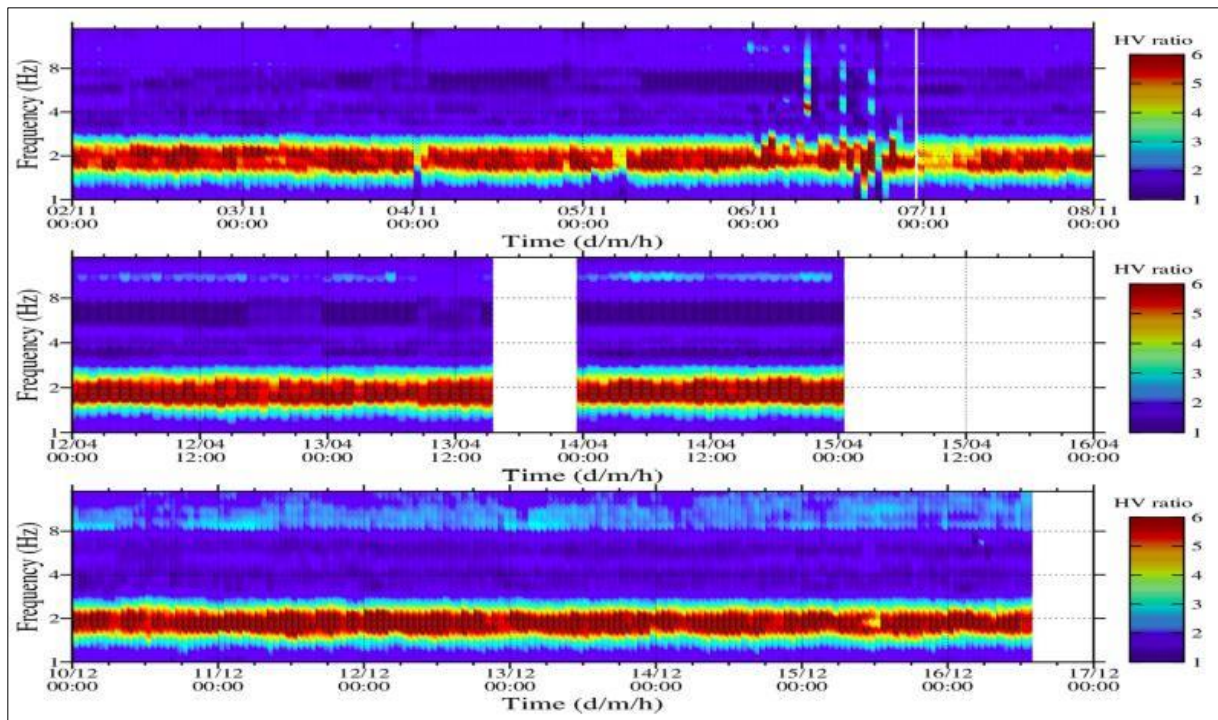


Figure 35 Seasonal response of HVSR curves recorded at triangular array of three sensors. Color presents HVSR amplitude. Station DF01, dry (top), intermediate (middle) and saturated (bottom).

At station DF01 no secondary peak was observed and only stratigraphic peak appears. This station was located at a stable place. The peak show no variations in response to meteorological changes. However, the value of the frequency peak is not changed in any case and the H/V amplitude is flattened under heavy rain (Chatelain et al., 2008).

The possible effects of rainfall infiltration are decrease in HVSR amplitude which may possibly be related with the rise in pore pressures in the soil because of the rainfall infiltrating water in the landslide mass. Along with pore pressure, the filtered water can possibly reduce the shear wave velocity through increasing degree of saturation and reduction in soil stiffness. These phenomena has intensely studied for the rainfall induced triggering of earthquakes and of landslide (Mainsaint et al., 2012; Harba & Pilecki, 2016). The ubiquitous and higher frequency peaks don't show any fluctuations in the amplitude in response to rainfall dependent degree of saturation (Figure 35 and 36). In our case, no prominent variations in the amplitude are observed mainly because the rainfall amounts during the recording period were not sufficient for the soil to reach a situation point. The soil of the regions is highly porous (55 %) and a large amount of water is required to produce changes in the state of the soil. In these conditions, the water will quickly move through the soil and saturate the areas with low elevation first. In the case of

Sobradinho landslide the rainfall water will return to the river because of its lower elevation (supported by the visual inspections at the site).

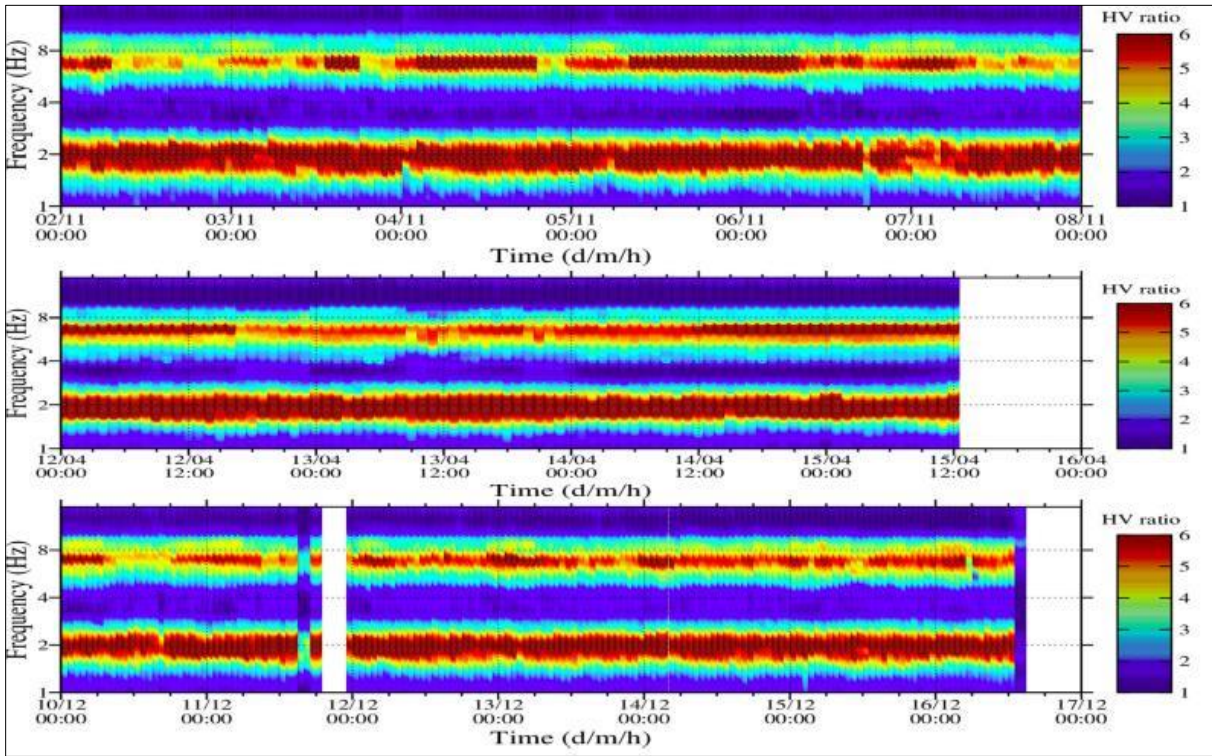


Figure 36 Seasonal response of HVSR curves recorded at triangular array of three sensors. Color presents HVSR amplitude. Station DF02, dry (top), intermediate (middle) and saturated (bottom).

**3.5. AMBIENT NOISE INTERFEROMETRY**

**3.5.1. CROSS-CORRELATION FUNCTION**

The cross-correlation functions for all station pairs have been computed. The pattern of correlation is complex and noisy at the natural scale experiment and the correlation functions are also not stable with the time. However, at prototype normal slope experiment the cross-correlation are good and less noisy (Figure 37). The stability of CCF over recording length shows the coherence over recording period and are symmetric because of the fixed position noise source (soil compressor), an important parameter for reliable velocity change estimation. If the sources were truly diffuse, and the wave-field dominated by surface waves, we would expect two symmetric wave packets at opposite time shifts, corresponding to intra-station surface waves. This is not the case if the source area was geographically small and there was no multipathing, we would expect to see an isolated wave packet at a time corresponding to the

difference in distance of the two stations from the source divided by an average wave velocity. Instead, several wave packages can be identified in the cross-correlation functions, distributed over a wide range of time shifts.

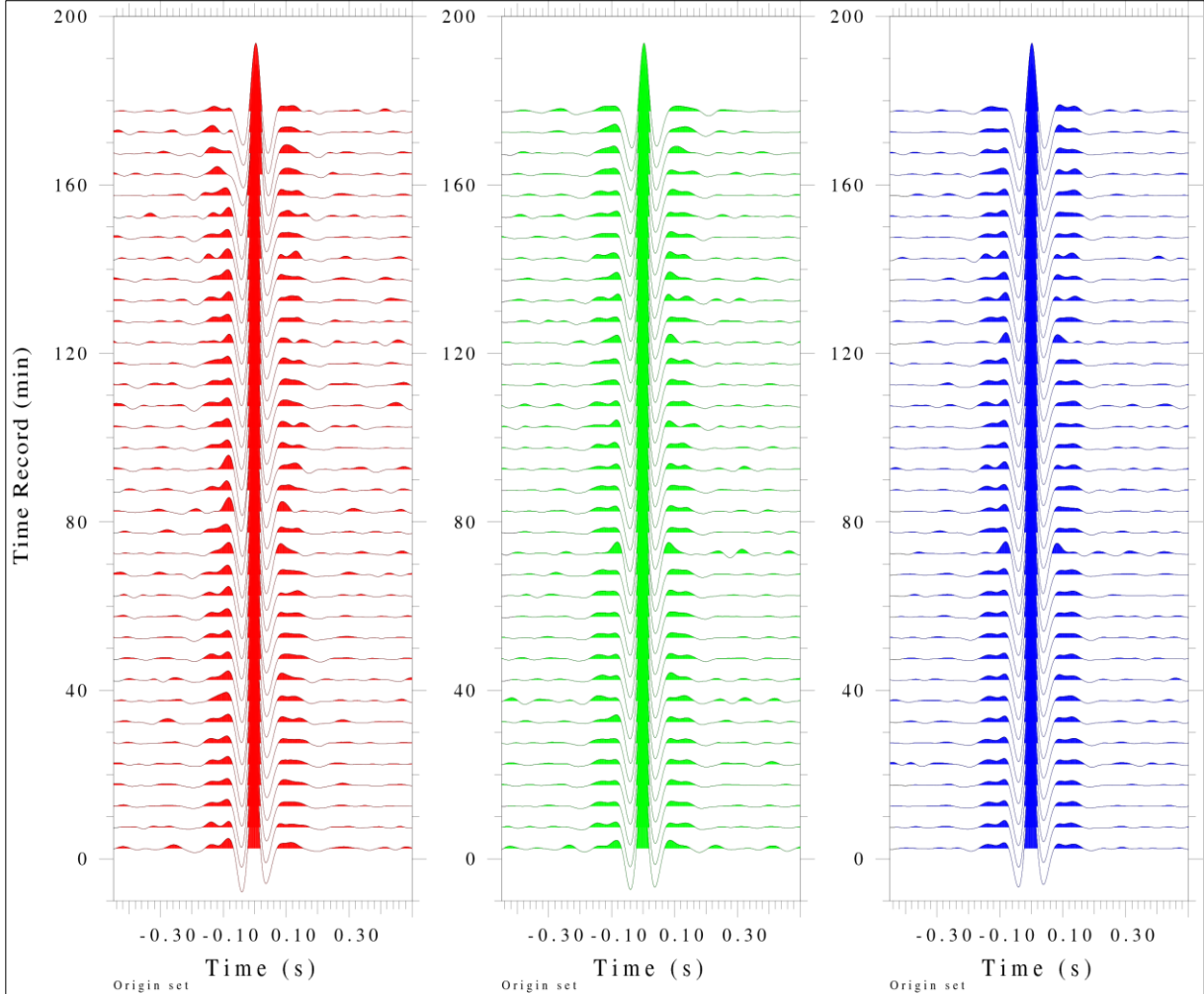


Figure 37 Cross-correlations traces of the prototype normal slope experiment (above), ZZ, RR and TT filtered between 6 and 16 Hz.

**3.5.2. PROTOTYPE EXPERIMENT**

The sensitivity of seismic with surface loads has been demonstrated in various previous studies (Taira & Brenguier, 2016). The increase in load leads to opening the cracks in the soil that lead to decrease in velocity. The load can also lead to increase in confining pressure and so closure the crack and decrease the seismic velocity (Hotovec-Ellis et al., 2014). These features of decreasing  $dV/V$  were observed in previous landslide monitoring studies (Mainsant et al., 2012).

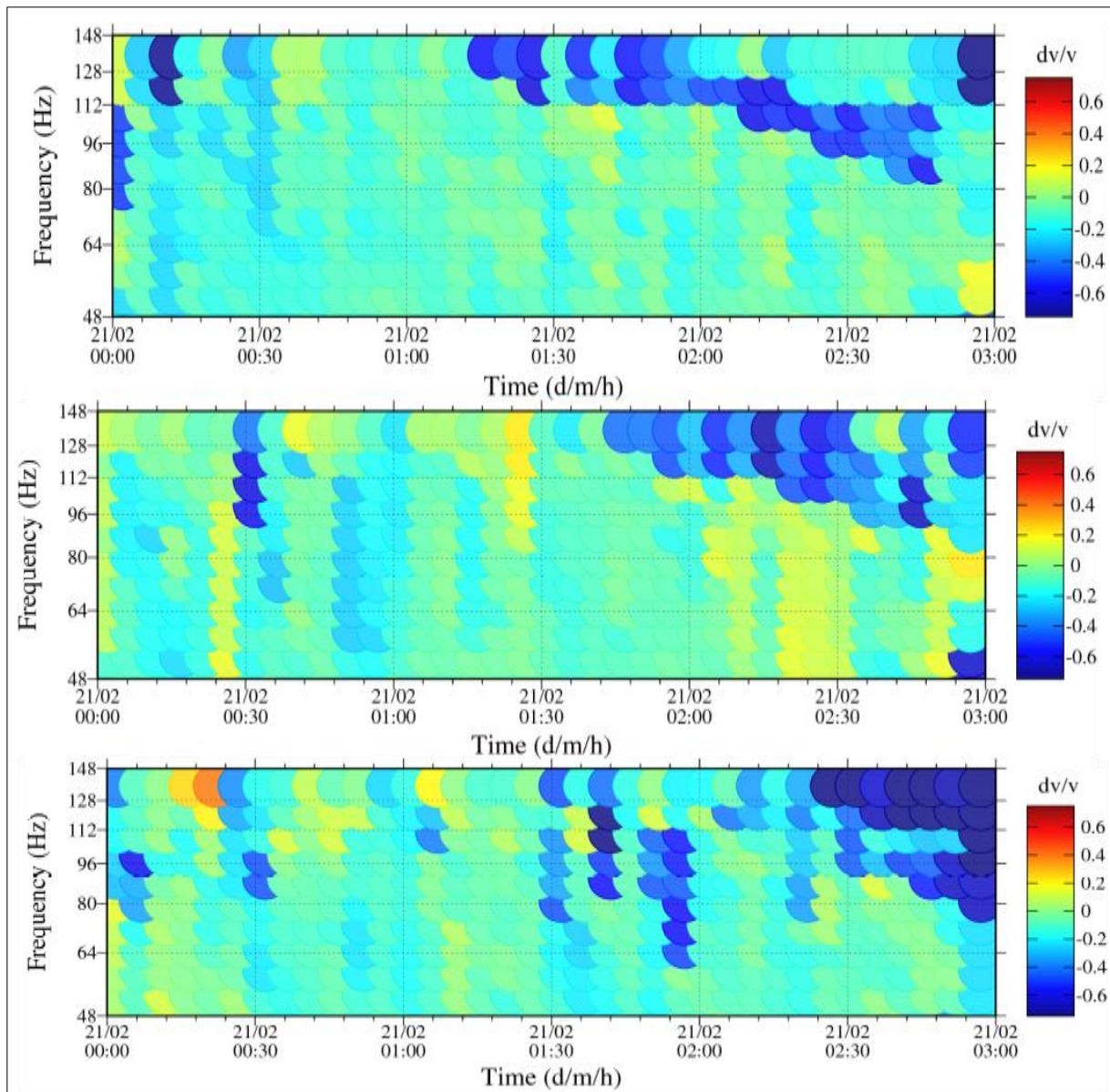


Figure 38 Relative velocity changes between stations PL01-PL02 at RR (top) and TT (middle) and ZZ (bottom) components representative of different stages of plate loading test.

Results of prototype experiments show a decrease in relative velocity change ( $dV/V$ ) with increase in applied loading on the soil (Figure 38). These decrease in  $dV/V$  may possibly be linked with the degree of soil microfracturing. These microfractures link together in the form of cracks at the slope surface which propagate through the soil and lead the collapse. However, in the present study we were not able induce some observable crack at the surface of normal slope.

### 3.5.2.1. TERRESTRIAL LASER SCANNING

The DEM of each loading interval are shown in Figure 39. From the beginning to end no observable changes are detected mainly because of the absence of centimeter scaled fractures on the slope surface. These are also supported by the visual observations during experiment. Only internal soil failure was taken place and changes were occurred because of the microfractures that developed along the shear surfaces.

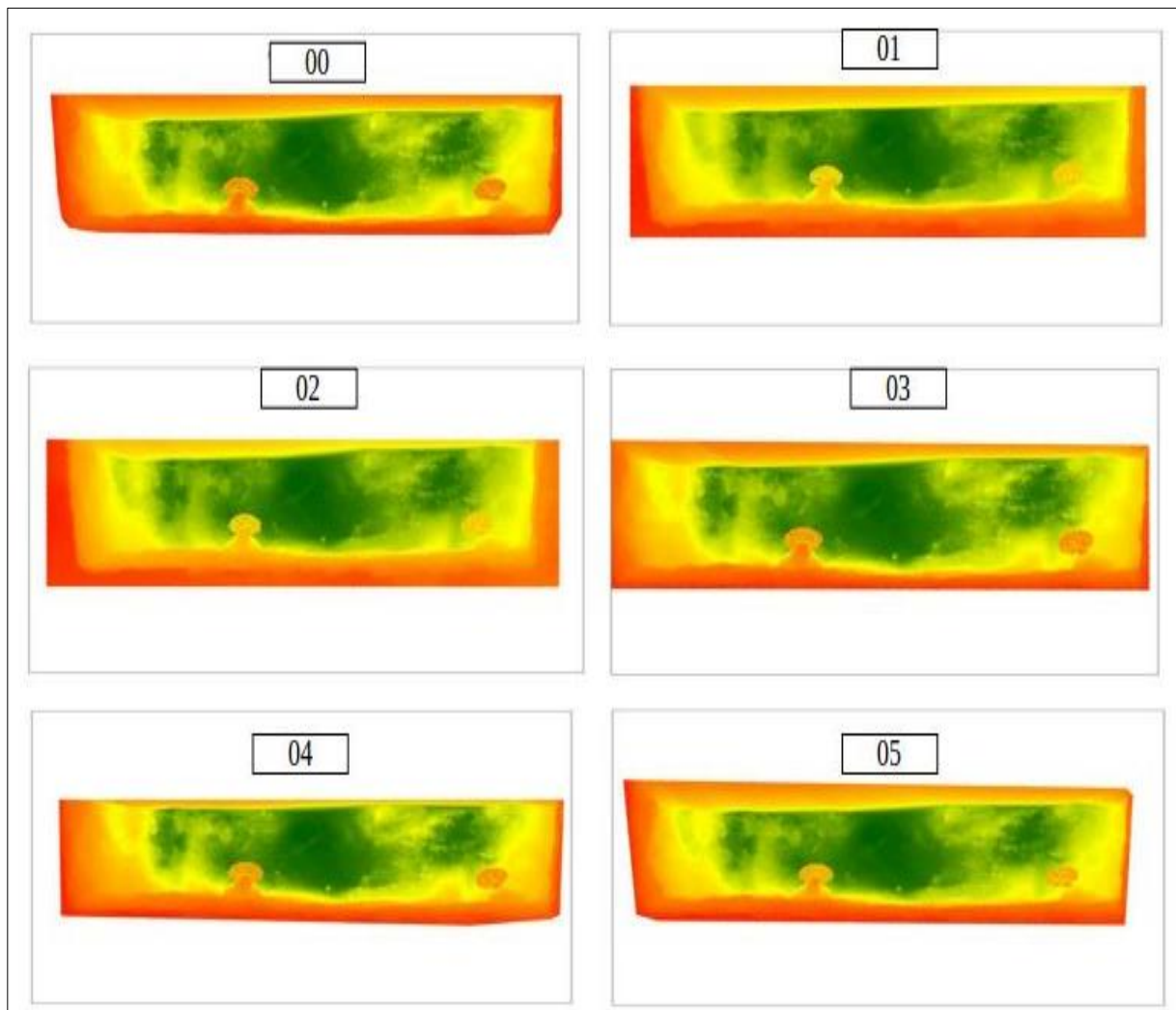


Figure 39 DEM of the normal slope surface at 5 minute temporal delays from beginning (0) to 25 minute (05).

### 3.5.2. SOBRADINHO LANDSLIDE

We have demonstrated that the velocity of the seismic waves at higher frequency is sensitive to changes of stress levels inside the soil. Because the physics of wave propagation is scale

independent and because of the high sensitivity of the noise monitoring technique (Fores et al., 2018), the seasonal monitoring of a natural scale landslide is done with ambient noise interferometry where there are no changes in relative velocity change at a frequency range of 2-24 Hz are observed that are linked with the absence of dynamism in the landslide mass.

There are very small changes over dry period are observed (Figure 40). These changes may possibly be produced by the action of river or because of uneven distributions of noise sources around the sensors.

A large amount of rainfall water is required for the highly porous tropical clay to reach its saturation point as dominating the surficial geology of the site. Based on preliminary numerical computations carried out in the University of Brasilia on such type of soil, it is concluded that a huge amount of water would be necessary to change the degree of saturation. Due to the high porosity of the soil (>55%), water would run through the soil mass to lower elevations saturating them first (Silva, 2009). However, during the recording campaign, the soil did not reach an optimal saturation required to show changes in  $dV/V$ .

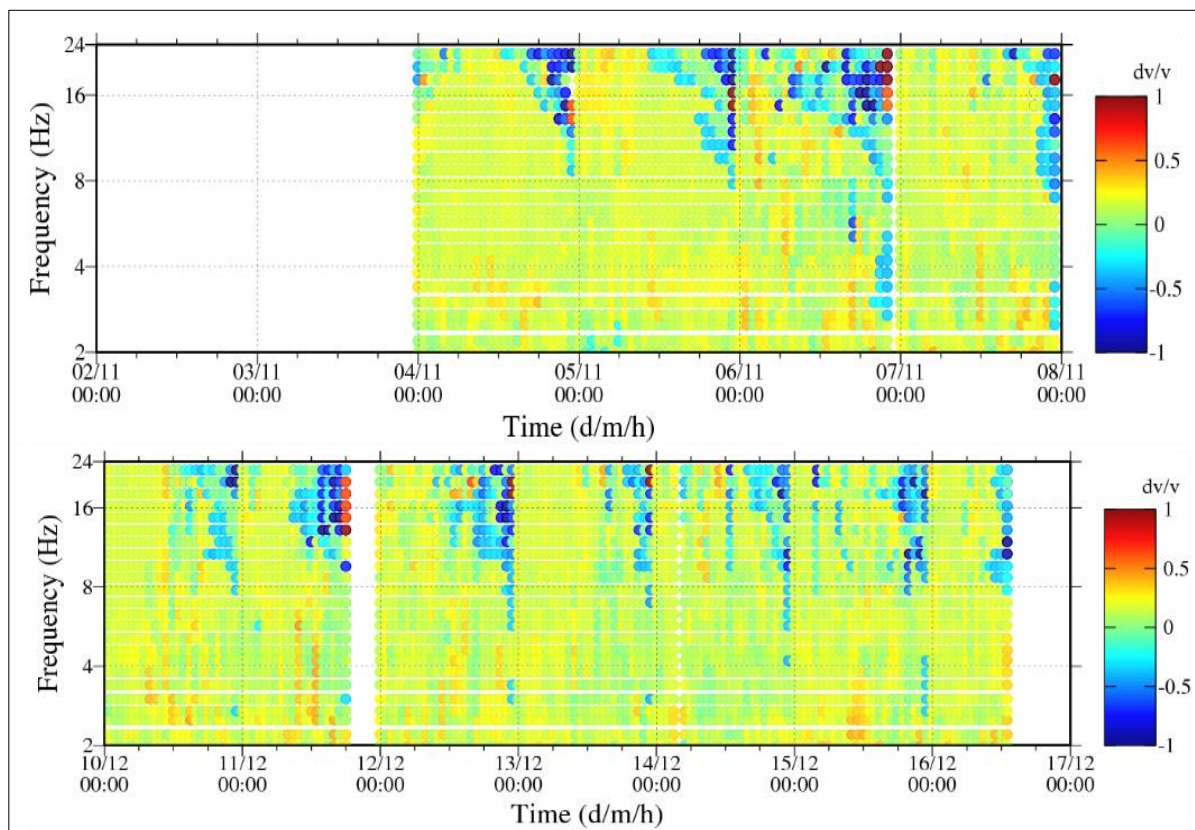


Figure 40 Relative velocity changes between stations DF01-DF02 at ZZ component representative of dry (above) and wet (below) conditions. Color bar presents  $dV/V$  values.

Related to the seismic emissions based techniques, no distinct phase onsets could be identified on the records of both experiments that had made the event localization difficult, thus the event screening is done with sonogram screening which is done in NanoseismicSuite, a specially designed software for the characterization and localization of the weak energy events. High energy events are observed over supersonogram at the end of experiment. These results are consistent with the soil displacement measured on load-displacement curve (Figure 43). The extensometers data was recorded at each pull out episode. When extraction on the EB pile kept on rising the increase in soil displacement is observed. This displacement leads to the micro-fractures around the developed shear zones along the pile. These fractures may propagate with joining the adjacent fractures. These fractures release energies which are recoded by the surface sensors (seismometers). The typology of these signals are present in Figure 41 and in Figure 42 a zoomed images of their sonogram patterns.

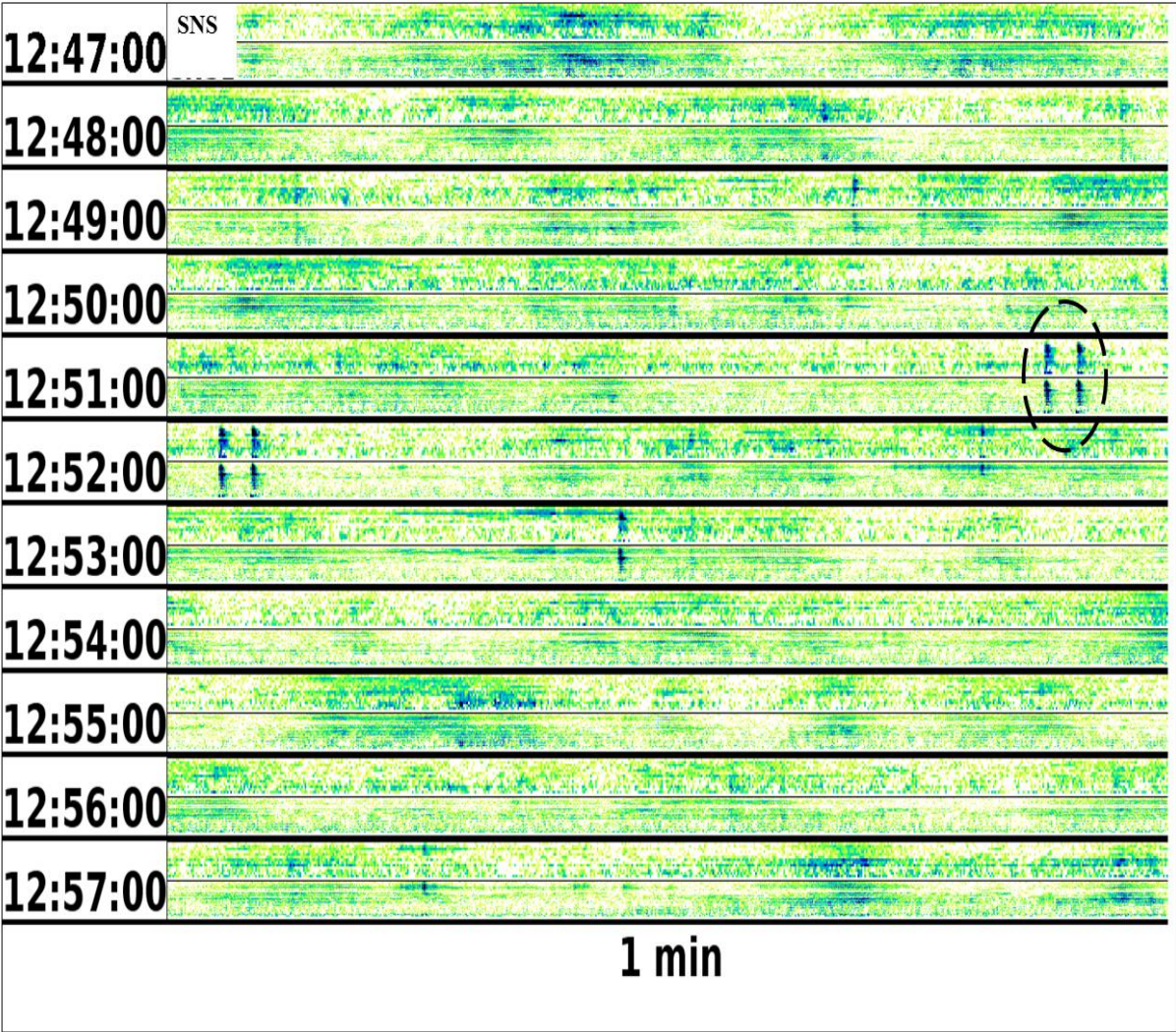


Figure 41 Event screening after 3 hours of the prototype experiment at the end of experiment the signals so identified are linked with the fracturing in the tropical soil.

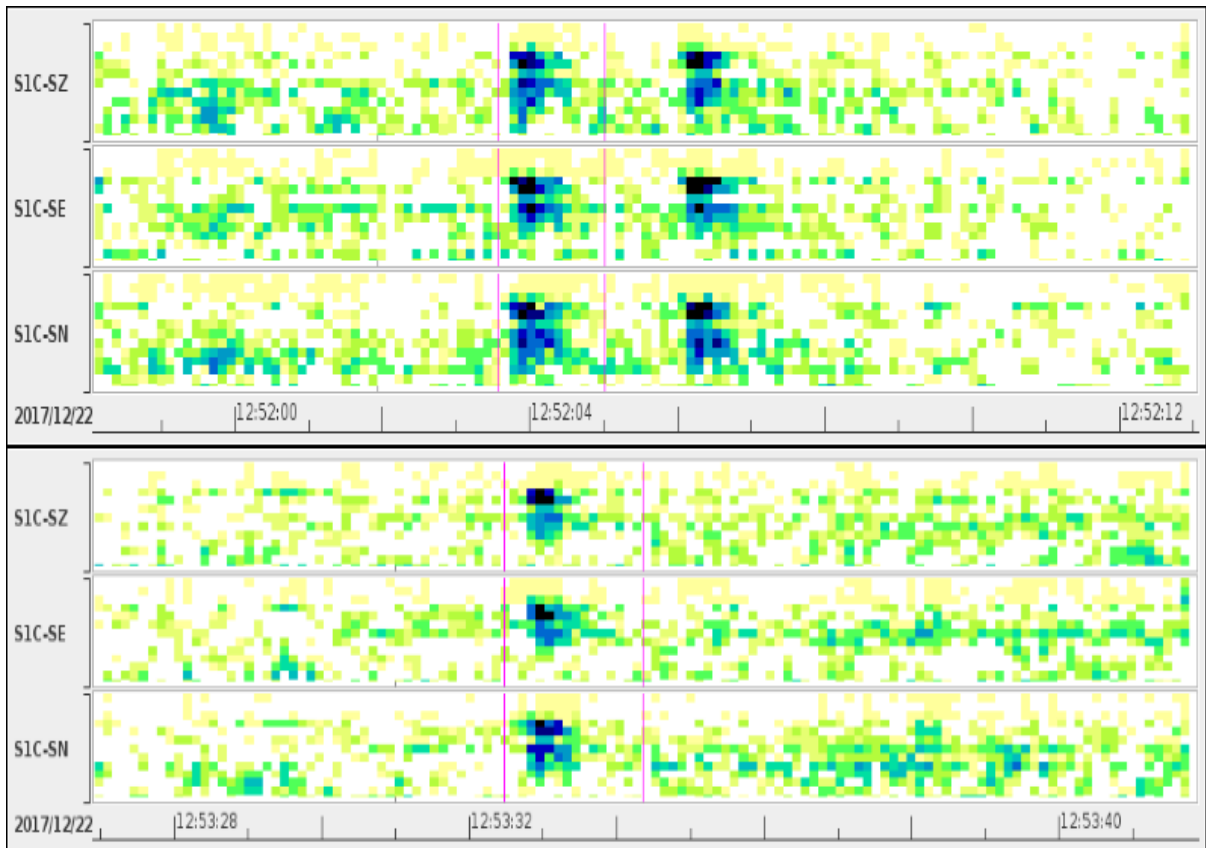


Figure 42 Zoomed sonogram images of the small energy fractures (micro-fractures) produced as a result of pullout test on an expendable body pile.

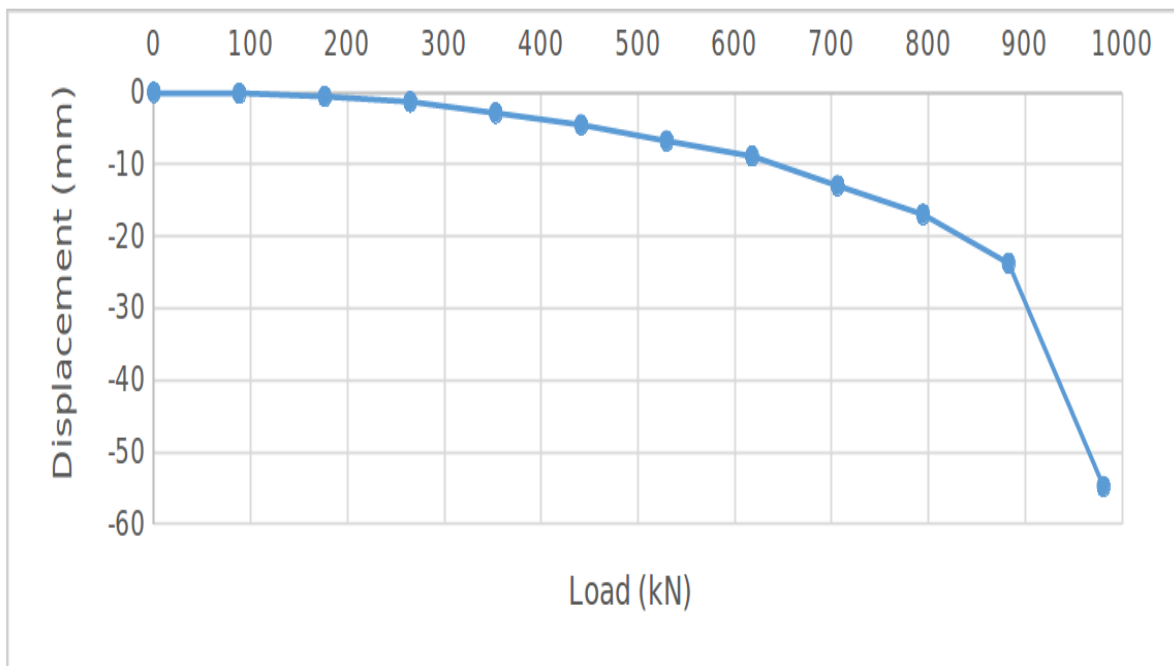


Figure 43 Load-displacement curve of the prototype expander body pile pullout experiment. Maximum soil displacement as well extension tremor are observed between 700-100 KN load.

The sonogram patterns of the dry period record at Sobradinho does not show any event that can be used for typological analysis. This can be linked with the absence of any activity at the site (Figure 44). The records of saturated conditions (rainfall) there are many events observed on the sonograms (Figure 44). There are two possible source mechanisms that had generated these signals, endogenic (dynamism inside the landslide) and exogenic (river bedload).

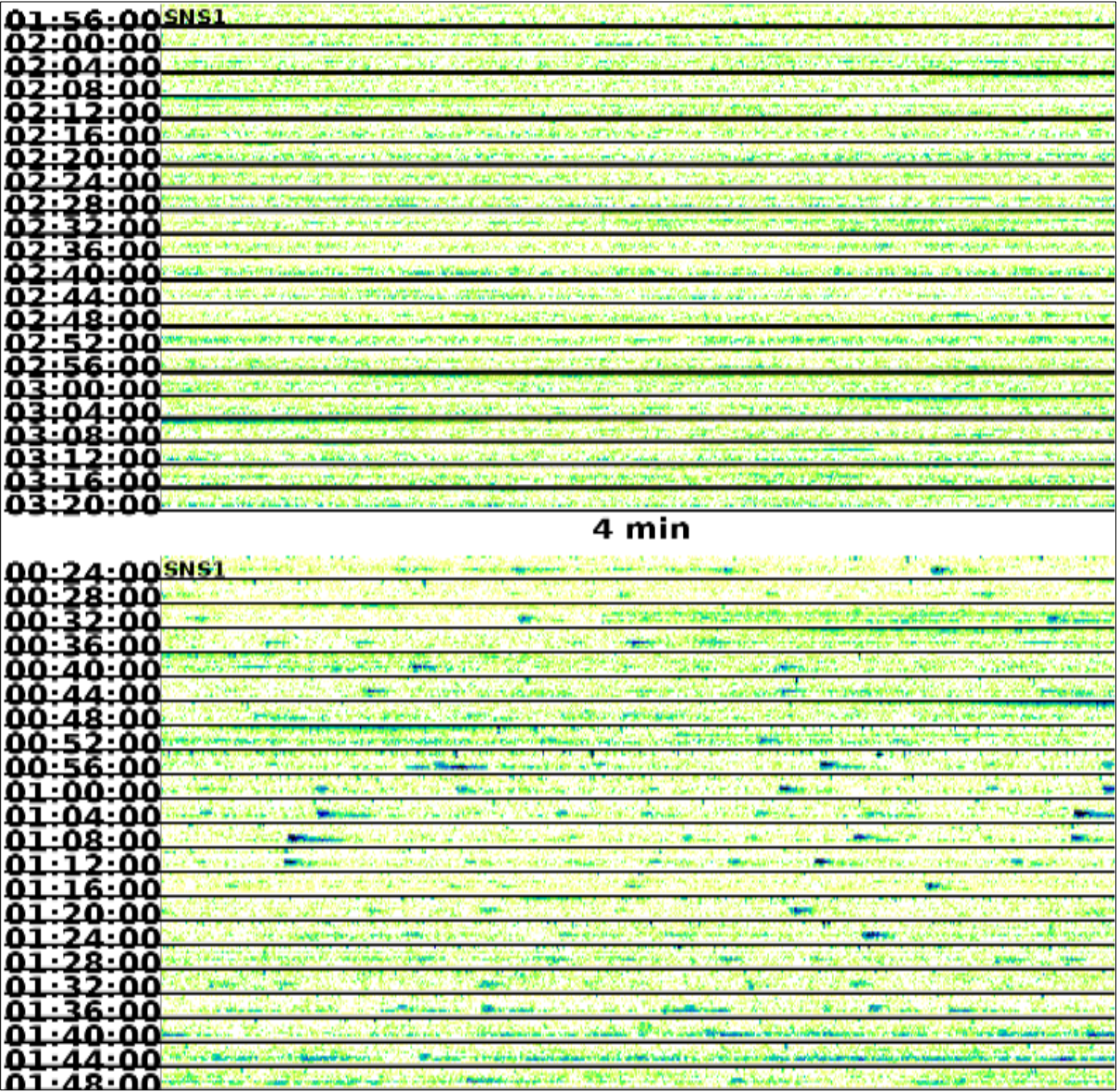


Figure 44 Zoom screening using supersonograms, natural scale a) dry, no prominent slidequakes are observed b) after rainfall events of propagating nature are identified which suspiciously linked the river dynamics.

There are two possible exogenic source mechanism are observed over the seismic record of landslide. First, at landslide different signals typologies are observed during rainy seasons (Figure 45). The events of propagative type are observed over the rainy season in the area. We

suppose that these signals are associated with bedload of the Capetinga River. During rainfall the sediment carrying energy of the river increase largely. The heavy sediments carry out by the river produce high seismic energies that are detected by the nearby seismometer Figure 46.

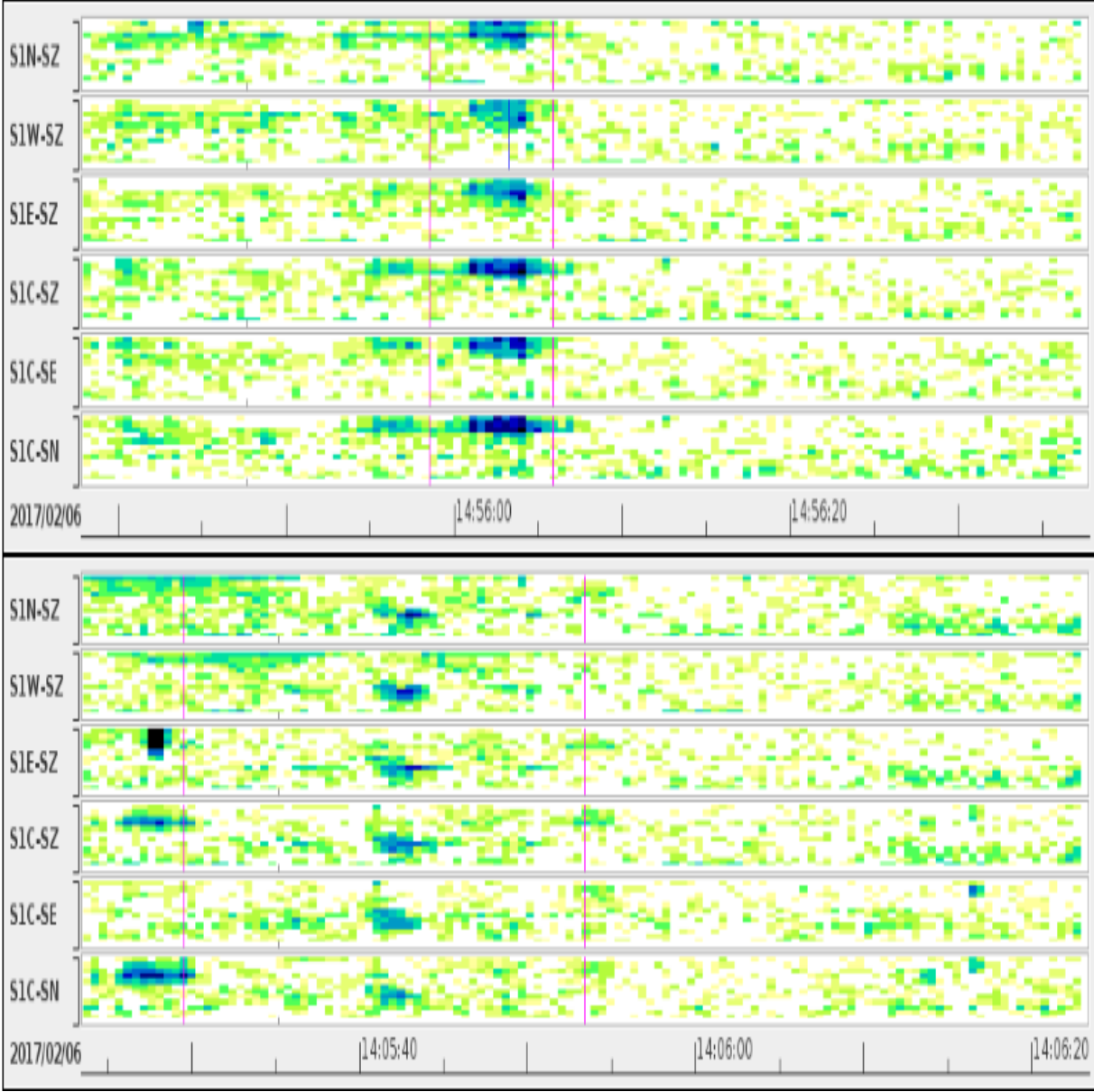


Figure 45 Zoomed sonogram presentation of the slidequakes at landslide immediate after the rainfall at two mini-arrays.

Second, the possible source mechanism of these propagative signals is the dynamism created by the river that in turn causing the tilting of seismometers, it has already studied by Anthony et al. (2018). So these signals may possible be generated by the aseismic processes and not by the activities in the landslide body itself. In order to prove this more controlled future experiments are recommended. The experiments must consist in geotechnical and geodetic

monitoring methodologies (Rothmund et al., 2017) so that the sources of signals can be linked with some superficial displacements and the degree of pore pressure inside the landslide mass.

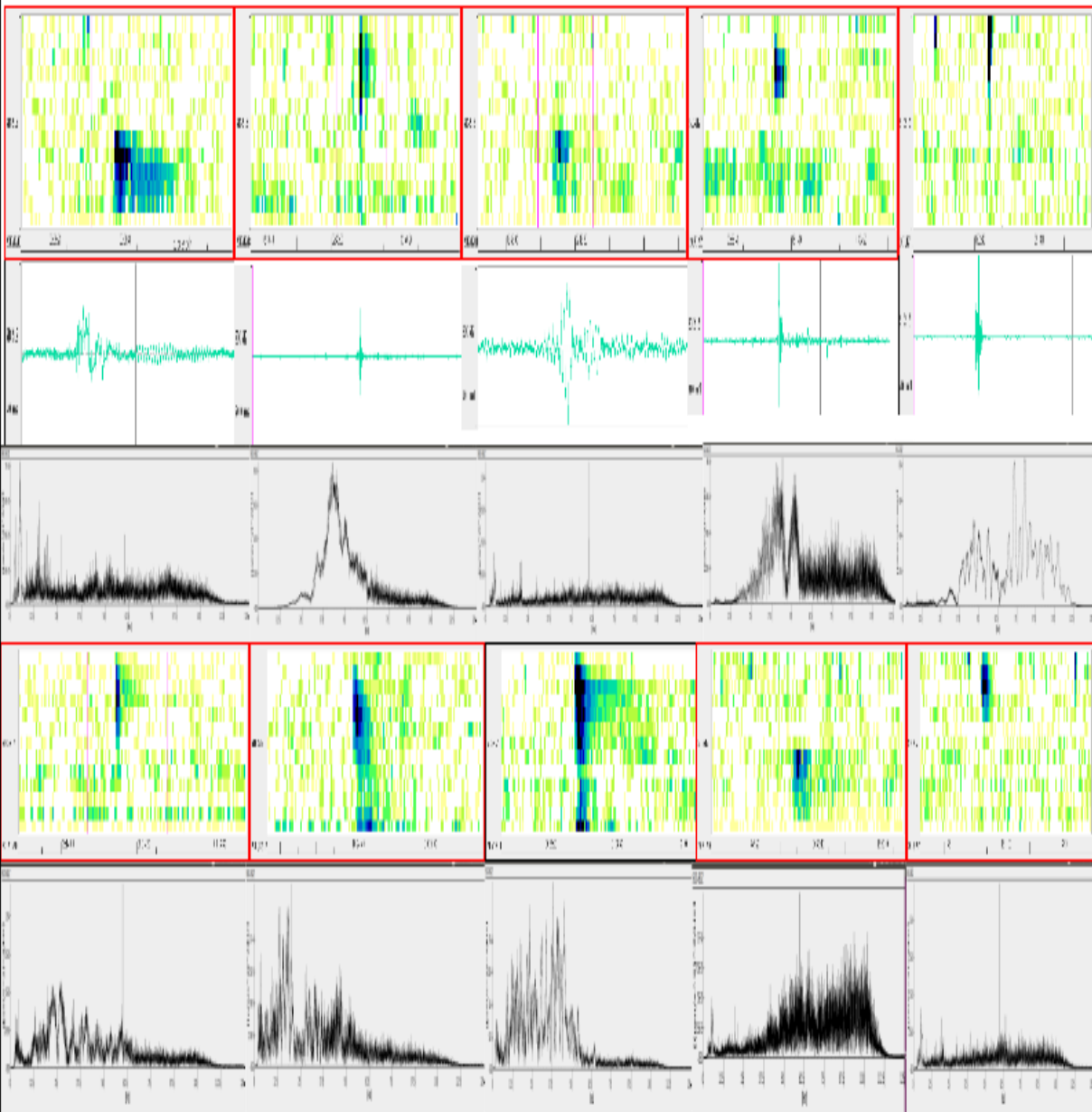


Figure 46 Typologies of the signals observed during rainy season at Sobradinho landslide, recorded using signal station. First row is the sonogram, 2nd and 3rd rows are waveform and spectrum, respectively.

#### 4. DISCUSSION AND CONCLUSIONS

The obtained results from the analysis of microtremor (>1 Hz) output that the contribution to the noise recorded at stations inside and outside the monitored mass movement is likely due to several factors including man-induced disturbance and instrument self-noise. From f-k analysis,

it is concluded that waves come at 260 degree azimuth are devoid of surface waves at the higher frequency range (greater than 7 Hz). These frequency dependent variations in velocity indicate a presence of surface waves. Shear wave velocities present three layered stratigraphy at 7, 12 and 24 m depths. It is assumed that the abrupt rheology change between the first and the second layer could be significant to trigger (reactivation) a landslide during a moderate or strong rainfall event. Site characterization results obtained from MASW showed a continuous increasing trend of material rigidity with depth. The profiles run parallel and perpendicular to the landslide body showed the material deformation in terms of disturbance in the Vs velocity layering. The profile recorded at the alluvial plain showed parallel Vs layers. On ERT profiles the slip surface was delineated very clearly. There are also high resistivity material were found at the landslide which may possibly be linked with the presence of coarse grain materials that may provide the permeable paths for the infiltration of rainfall water. The infiltrating water will develop pore pressure inside the landslide mass and may cause of problem related to its stability. The HVSR measurement taken inside the landslide body showed two peaks, one at low frequency (2 Hz) and second at high frequency (> 2Hz). The low frequency peak remained consistent on the measurements taken all around the landslide while peak at higher frequency peaks disappear as we move away from the landslide body. So it may possibly be related with the natural frequency of the landslide, the inverse of which is the natural period of the landslide.

The here obtained results from time-lapse ambient noise records using HVSR and ANI don't show any response to the rainfall induced changes in the landslide mass. The ambient noise recorded at a different saturation conditions are compared. Results of HVSR showed one peak at 2 Hz and secondary peak at high frequency however, results remained same throughout the experimental time span. No changes are observed in the form of percentage relative velocity changes ( $dV/V$ ) obtained from ANI at natural scale experiments.

The high porosity of the soil above 55% can create a problem in reaching the soil to its saturation level. For that soil type large amount of water is required to reach its saturation level under flat topographic condition. For the areas with topographic undulations such as Sobradinho landslide, an obstacle that deprived landslide mass reaches its saturation. Under these conditions the rainfall infiltrating water first saturate the soil at low elevation compared to the elevated soil. In Sobradinho the water moves through the soil and recharge the bottom flowing river. These are ground proofed by the onsite visual inspection. The short during of the data campaigns created problem with the results of ANI. The recorded time was short in which

the area did not receive sufficient amounts of rainfalls that can alter the degree of saturation in the soil.

In order to solve these problems of insufficient water in natural conditions, the applied methodologies were tested at prototype experiments in the experimental field. In these experiments, the rainfall as a trigger was replaced with the applied load that made the use of experiment effective in urban environments. The changes are induced in the tropical soil where monitoring with the same ambient noise based techniques are done. The here obtained results are completely different from the natural scale. HVSR curves calculated at each loading episode showed a clear response to the deformation. The same is true in the case of ANI results, a continuous decreasing trend in the middle of the experiment was observed that led to a maximum velocity decrease of -0.6% at the end of experiment. In other words, microfracturing produced in soil were detected in term of relative change in velocity and amplitude decrease on HVSR curve.

Following conclusions are drawn from the dynamic analysis using ambient noise

- The peak at 2 Hz is not related to fluvial process and instead represent the site response of seismically low velocity alluvium overlying higher velocity seismic bedrock.
- Secondary peaks are related with the detached blocks at the landslide mass and its amplitude is related with the degree of impedance contrast.
- Both peaks do not show any response to seasonal effects mainly because of the relatively lesser degree of soil saturation.
- Every increase in soil stress there is a small decrease in the amplitude of HVSR peak. HVSR shows amplitude variations in response to the development of microfractures in the tropical clay that can be used for the landslide early warning systems based on the real-time soil mechanism.
- The relative changes in velocity ( $dV/V$ ) decreased with the increase in load on the slope and reached a value of -0.6% at the end of experiment.
- No changes at the surface of normal slope are detected by TLS analysis. This means that during the loading process there were absence of centimeter scaled fractures.
- No changes were detected on Sobradinho landslide because the rainfall amounts were not sufficient to reach the soil of high porosity to reach its saturation

Next, the evaluation of seismic signature of extraction test on expander body pile in tropical clayey soil, the signals so detected are planned to use as a benchmark for the seasonal dynamical analysis of Sobradinho landslide that is representative of many landslides in the region.

- Signal release in response to soil failure are of short duration and related positively with the increase in soil displacement as observed on load-displacement curve.
- A unique topology the signals is observed during prototype field experiment and is termed as extension tremor (novel). The typology of extension tremor is differ from the one recorded at landslide, which show that this analysis has potential of separating the different stages of soil failure mechanisms based on these typologies.
- No nanoseismic signals (slidequakes) are detected on the Sobradinho landslide during dry season mainly because of the absence of dynamism in the landslide mass and low erosional as well as bed load carrying potential of the Capetinga River.
- During rainy season slidequakes are observed having many ambiguous source mechanisms like dynamism in the landslide body itself or because of the dynamism in the river (erosion or bed-load).

## **5 RECOMMENDATIONS**

The present study is a preliminarily step that will lead to a comprehensive application of geophysical techniques for the landslide hazard assessment. However, there are several technical and practical issues that deserve further investigations. Further detailed studies are required for the understanding of dynamism involved in the triggering of that mass movement. In this way be limitations of passive seismic monitoring such as high spatial uncertainty of the detected seismic events and hence speculative sources characterization, can be curtailed by the involvement of remote sensing and geodetic datasets as well as the geotechnical information of the area.

For normal slope experiment, a better loading mechanism is recommended that will lead to a complete slope collapse. This will help in understanding all episodes of slope failure like before during and after the slope collapse.

For better shear velocity measurement, more MASW profiles are required with same seismometers (2 Hz) so that a joint inversion of HVSR curves and dispersion curve obtained from MASW can be done.

For the ERT denser profiles are recommended so that a high resolution 3D model of Sobradinho landslide can be built. In this way the orientation and depth of fractures over the landslide body can be determined.

The natural period (fundamental site period) of SLS was derived from time-lapse single station horizontal to vertical spectral ration curves (HVSR by Equation (12).

$$1/T_s = V_s/4H \quad (12)$$

Where H is the thickness of the landslide mass and  $V_s$  is the shear-wave velocity of the landslide material.

This equation shows that period of LS is dependent of the shear wave velocity ( $V_s$ ). One possible cause of changes in  $V_s$  is the degree of saturation because of the rainfall. So the seasonal effects of period change can be predicted by numerical simulation using Coupled Newmark Approach' in SLAMMER Numerical Codes. This analysis can be used for the modeling of interaction of sliding shear stresses on the dynamic response of the landslide. In this model sliding surface is defined by its height (H), shear wave velocity, and damping ratio.

The effects of changes in the degree of saturation in terms of shear wave velocity change at a particular frequency can be modeled by using software developed by Herrmann, R.B. (2013). The S-wave velocity dry profile can be defined from previous studies. The current ( $V_t$ ) and reference ( $V_{ref}$ ) profiles can be calculated for the mean saturation of the whole period, which is the reference used to get the experimental  $dV/V$ .

## **ARTICLES**

### **JOURNAL PUBLICATION**

1. Hussain et al. (in press). Introductory review of potential applications of nanoseismic monitoring in seismic energy characterization, *Journal of Engineering Research*.
2. Hussain et al. (in press) Shear wave velocity estimation by a joint inversion of HVSR and f-k curves under diffuse field assumption: a case study of Sobradinho landslide. *Anuario do Instituto de Geociencias - UFRJ* (in press).
3. Hussain et al. (in press) Ambient Seismic Noise: A Continuous Source for the Dynamic Monitoring of Landslides, *Terrae Didactica*.
4. Hussain et al. (2018). Analysis of Surface Waves Recorded at a Mass Movement in Brasilia, Brazil: An Implication in Hazard Mitigation, *Geociencias*, 37(2):285-391.
5. Hussain et al. 2017. Microtremor Response of a Mass Movement in Federal District of Brazil, *Anuario do Instituto de Geociencias - UFRJ*, 40(5):212-221.
6. Braga, L.M.; Caldeira, D.; Nunes, J.G.S.; Hussain, Y. et al. (2018). Geomorphological description and erosive-depositional dynamics of hill slopes on Ribeirao Contagen Fluvial Valley-DF, *Anuario do Instituto de Geociencias - UFRJ*, 41(2):51-65.

### **CONFERENCE PAPERS**

1. Hussain et al. (2018) Typological Analysis of Microseismic Emission: An Experiment on Expandable Body Pile, *UKBrazilain Symposium*, Goinia, Brazil.
2. Hussain et al. (2017). Detecting the Soil Instabilities under Variable Loading Conditions by Rayleigh Wave Velocity Change, *IEEE/OES 2017 RIO ACOUSTICS*, Rio de Janeiro, Brazil.
3. Hussain et al. (2017) A Brief Introduction to Nanoseismic Monitoring, *15th International Congress of the Brazilian Geophysical Society and the EXPOGEf 2017*, Rio de Janeiro, Brazil.
4. Hussain et al. (2017) Seasonal Monitoring of Hydrological Stresses Developed by Varying Degree of Rainfall Induced Pore-Pressures Using Noise Data, *15th International Congress of the Brazilian Geophysical Society and the EXPOGEf 2017*, Rio de Janeiro, Brazil.
5. Hussain et al. (2017). Spectral analysis of the recorded ambient vibration at a mass movement in Brasilia, *SAGEEP 2017*, Denver, Colorado, USA.
6. Hussain et al. (2017). Detection of Seasonal Variations in Rigidity of a Clayey Landslide in Brasilia by Ambient Noise Interferometry (Preliminary Results), *GEOCENTRO2017*.

## Conference Abstracts

1. Mapping the Depth of Carbonate Rocks in a Small Colluvium of Contagem River Basin, Brasilia. In: Anais do X Simpósio Sul -Brasileiro de Geologia, 2017, Curitiba. Anais do X Simpósio Sul -Brasileiro de Geologia, 2017.
2. Time-lapse monitoring of a mass movement in Brasilia using noise interferometry towards failure prediction (first results). In: I Congresso Brasileiro de Reducao de Riscos de Desastres: Gestao Integrada em RRD no Brasil e o Marco de SENDAI, 2016, Curitiba, Parana, Brasil. I Congresso Brasileiro de Reducao de Riscos de Desastres, 2016.
3. Optimizing the detectability of microseismicity associated with stress-relief mechanism by relative rayleigh wave velocity change. In: 48o Congresso Brasileiro de Geologia, 2016, Porto Alegre – Brazil.
4. Nanoseismic Monitoring an Attractive Choice for Civil Engineers, IASPEI, Regional Assembly Latin-American and Caribbean Seismological Commission-LACSC

## REFERENCES

- Akpan, A.E., Ilori, A.O. & Essien, N.U. (2015). Geophysical investigation of Obot Ekpo Landslide site, Cross River State, Nigeria. *Journal of African Earth Sciences*, 109:154-167
- Anthony, R.E., Aster, R.C., Ryan, S., Rathburn, S. & Baker, M.G. (2018) Measuring Mountain River Discharge Using Seismographs Emplaced within the Hyporheic Zone. *Journal of Geophysical Research: Earth Surface*, 123(2):210-228.
- Araki, M.S. (1997). Aspectos relativos às propriedades dos solos porosos colapsáveis do Distrito Federal. Programa de Pós-graduação em Geotecnia, Departamento de Engenharia Civil, Universidade de Brasília, Dissertação de Mestrado, 121p.
- Arce, M. & Terceros Herrera, M.A. (2016). The Use of an Expander Body with Full Displacement Piles in Medium-Dense Sandy Soils. In *Geo-China 2016* (pp. 142-151).
- Bakulin, A., Mateeva, A., Mehta, K., Jorgensen, P., Ferrandis, J., Herhold, I. & Lopez, J. (2007). Virtual source applications to imaging and reservoir monitoring, *The Leading Edge*, 26(6):732–740.
- Bard, P.Y. & SESAME-Team: Guidelines for the implementation of the H/V spectral ratio technique on ambient vibrations-measurements, processing and interpretations, SESAME European research project EVG1-CT-2000-00026, deliverable D23.12, available at: <http://sesame-fp5.obs.ujf-grenoble.fr>, 2004.
- Bard, P.Y. (1999). ‘Microtremor measurements: a tool for site effect estimation?’, A.A. Balkema/Rotterdam/Brookfiel/1999
- Benjumea, B., Macau, A., Gabàs, A. & Figueras, S. (2016). Characterization of a complex near-surface structure using well logging and passive seismic measurements. *Solid Earth*, 7, 685-701.
- Bensen, G.D., Ritzwoller, M.H., Barmin, M.P., Levshin, A.L., Lin, F., Moschetti, M.P. .... & Yang, Y. (2007). Processing seismic ambient noise data to obtain reliable broad-band surface wave dispersion measurements. *Geophysical Journal International*, 169(3):1239-1260.
- Bichler, A., Bobrowsky, P., Best, M., Douma, M., Hunter, J., Calvert, T. & Burns, R. (2004). Three-dimensional mapping of a landslide using a multi-geophysical approach: the Quesnel Forks landslide. *Landslides*, 1(1):29-40.
- Bonnefoy-Claudet, S., Köhler, A., Cornou, C., Wathelet, M. & Bard, P.-Y., (2008). Effects of love waves on microtremor H/V Ratio. *Bulletin of the Seismological Society of America*, 98(1):288–300.
- Bottelin, P., Baillet, L., Larose, E., Jongmans, D., Hantz, D., Brenguier, O.,....& Helmstetter, A. (2017). Monitoring rock reinforcement works with ambient vibrations: La Bourne case study (Vercors, France). *Engineering Geology*, 226:136-145.

- Boué, P., Poli, P., Campillo, M., Pedersen, H., Briand, X. & Roux, P. (2013). Teleseismic correlations of ambient seismic noise for deep global imaging of the earth. *Geophysical Journal International*, 194(2):844–848
- Braga, L.M., Caldeira, D., da Silva Nunes J.G., Hussain Y., Carvajal H.M. & Uagoda, R. (2018). Caracterização Geomorfológica e Dinâmica Erosivo-Deposicional de Encostas no Vale Fluvial do Ribeirão Contagem-DF, Brasil (in Portuguese), *Anuário do Instituto de Geociências – UFRJ*, 41(2): 51-65.
- Brenguier, F., Shapiro, N.M., Campillo, M., Ferrazzini, V., Duputel, Z., Coutant, O. & Nercessian, A. (2008b). Towards forecasting volcanic eruptions using seismic noise. *Nature Geoscience*, 1(2):126–130.
- Burda, J., Hartvich, F., Valenta, J., Smítka, V. & Rybár, J. (2013). Climate-induced landslide reactivation at the edge of the Most Basin (Czech Republic)-progress towards better landslide prediction. *Natural Hazards and Earth System Sciences*, 13(2): 361.
- Burjánek, J., Gassner-Stamm, G., Poggi, V., Moore, J.R. & Fäh, D. (2010). Ambient vibration analysis of an unstable mountain slope. *International Journal of Geophysics*, 180(2):820–828.
- Campos, J.E.G. (2004). Hidrogeologia do Distrito Federal: Bases para a Gestão dos Recursos hídricos Subterrâneos. *Revista Brasileira de Geociências*, 34(1):41-48.
- Cárdenas-Soto, M., Ramos-Saldaña, H. & Vidal-García, M. (2016). Interferometría de ruido sísmico para la caracterización de la estructura de velocidad 3D de un talud en la 3ª Sección del Bosque de Chapultepec, Ciudad de México. *Boletín de la Sociedad Geológica Mexicana*, 6(2):173-186. (In Spanish).
- Chatelain, J.L., Guillier, B., Cara, F., Duval, A.M., Atakan, K. & Bard, P.Y. (2008). Evaluation of the influence of experimental conditions on H/V results from ambient noise recordings. *Bulletin of Earthquake Engineering*, 6(1):33-74.
- Chesley, J.T., Leier, A.L., White, S. & Torres, R. (2017). Using unmanned aerial vehicles and structure-from-motion photogrammetry to characterize sedimentary outcrops: An example from the Morrison Formation, Utah, USA. *Sedimentary Geology*, 354:1-8.
- Clarke, D., Zaccarelli, L., Shapiro, N.M. & Brenguier, F. (2011). Assessment of resolution and accuracy of the Moving Window Cross Spectral technique for monitoring crustal temporal variations using ambient seismic noise. *Geophysical Journal International*, 186(2):867-882.
- Colangelo, G., Lapenna, V., Loperte, A., Perrone, A. & Telesca, L. (2008). 2D electrical resistivity tomographies for investigating recent activation landslides in Basilicata Region (Southern Italy). *Annals of Geophysics*.

- Czarny, R., Marcak, H., Nakata, N., Pilecki, Z. & Isakow, Z. (2016). Monitoring Velocity Changes Caused By Underground Coal Mining Using Seismic Noise. *Pure and Applied Geophysics*, 173(6):1907-1916.
- D'HOUR, V. (2015). Medium change monitoring using ambient seismic noise and coda wave interferometry: examples from intraplate NE Brazil and the Mid-Atlantic Ridge, doctoral thesis, Universidade Federal do Rio Grande do Norte, Natal, Brazil.
- Dantas, O.A.B., do Nascimento, A.F. & Schimmel, M. (2018). Retrieval of body-wave reflections using ambient noise interferometry using a small-scale experiment. *Pure and Applied Geophysics*, 175(6):2009–2022.
- de Vasconcelos, I. & Snieder, R., (2008). Interferometry by deconvolution: Part 1-Theory for acoustic waves and numerical examples. *Geophysics*, 73(3):S115-S128.
- Del Gaudio V. & Wasowski J. (2011). Advances and problems in understanding the seismic response of potentially unstable slopes. *Engineering Geology*, 122(1):73–83.
- Delgado, J., Garrido, J., Lenti, L., Lopez-Casado, C., Martino, S. & Sierra, F.J. (2015). Unconventional pseudostatic stability analysis of the Diezma landslide (Granada, Spain) based on a high-resolution engineering-geological model. *Engineering Geology*, 184:81-95.
- Deparis, J., Jongmans, D., Cotton, F., Baillet, L., Thouvenot, F. & Hantz, D. (2008). Analysis of rock-fall and rock-fall avalanche seismograms in the French Alps. *Bulletin of the Seismological Society of America*, 98(4), 1781-1796.
- Fernandes, N.F. & Amaral, C. (1997). Movimentos de Massa: uma abordagem geológico-geomorfológica. In: GUERRA, A.P.T. & CUNHA, B. (Orgs.), *Geomorfologia e Meio Ambiente*. Rio de Janeiro, Editora Bertran Brasil, p. 123-194.
- Ferreira, R.S. & Uagoda, R. (2015). Morphometric study of controls to Erosional Features and identification of areas susceptible to Mass Movement Hazards in the Contagem Watershed. Distrito Federal. *Espaço & Geografia*, 18(1):187-216
- Fiorucci, M., Iannucci, R., Lenti, L., Martino, S., Paciello, A., Prestininzi, A. & Rivellino, S. (2017). Nanoseismic monitoring of gravity-induced slope instabilities for the risk management of an aqueduct infrastructure in Central Apennines (Italy). *Natural Hazards*, 86(2):345-362.
- Fiorucci, M., Iannucci, R., Martino, S. & Paciello, A. (2016). Detection of nanoseismic events related to slope instabilities in the quarry district of Coreno Ausonio (Italy). *Italian Journal of Engineering Geology and Environment*, 16(2):51-63.
- Fores, B., Champollion, C., Mainsant, G., Albaric, J. & Fort, A. (2018). Monitoring saturation changes with ambient seismic noise and gravimetry in a Karst Environment. *Vadose Zone Journal*, 17(1)(in press).

- Freitas-Silva, F.H. & Campos, J.E.G. (1998). Geologia do Distrito Federal. In: IEMA/SEMATEC/UnB. Inventário Hidrogeológico e dos Recursos Hídricos Superficiais do Distrito Federal. Brasília. IEMA/SEMATEC/UnB. Vol. 1, Part I. P86.
- Galea, P., D'Amico, S. & Farrugia, D. (2014). Dynamic characteristics of an active coastal spreading area using ambient noise measurements—Anchor Bay, Malta. *Geophysical Journal International*, 199(2):1166-1175.
- Gomberg, J., Bodin, P., Savage, W. & Jackson, M. (1995). The Slumgullion earthflow, Colorado: A useful analog to crustal tectonics. *Geology*, 23:41–44.
- Gomberg, J., Schulz, W., Bodin, P. & Kean, J. (2011). Seismic and geodetic signatures of fault slip at the Slumgullion Landslide Natural Laboratory, *Journal of Geophysical Research*, 116.
- Gomes, R.A.T., Guimarães, R.F., Carvalho, J., Abílio, O., Fernandes, N.F. & Amaral Júnior, E.V. (2013). Combining spatial models for shallow landslides and debris-flows prediction. *Remote Sensing*, 5(5): 2219-2237.
- Gosar, A. & Lenart, A. (2010). Mapping the thickness of sediments in the Ljubljana Moor basin (Slovenia) using microtremors. *Bulletin of Earthquake Engineering*, 8(3):501-518.
- Got, J.L., Mourot, P. & Grangeon, J. (2010). Pre-failure behaviour of an unstable limestone cliff from displacement and seismic data. *Natural Hazards and Earth System Sciences*, 10(4):819-829.
- Gret, A., Snieder, R. & Özbay, U. (2006). Monitoring in situ stress changes in a mining environment with coda wave interferometry. *Geophysical Journal International*, 167(2):586–598.
- Hadziioannou, C., Larose, E., Coutant, O., Roux, P. & Campillo, M. (2009). Stability of monitoring weak changes in multiply scattering media with ambient noise correlation: Laboratory experiments. *The Journal of the Acoustical Society of America*, 125(6):3688-3695.
- Häge, M. & Joswig, M. (2009). Microseismic feasibility study: detection of small magnitude events ( $M_L < 0.0$ ) for mapping active faults in the Betic Cordillera (Spain). *Annals of Geophysics* 52(2):117-126.
- Harba, P. & Pilecki, Z. (2017). Assessment of time–spatial changes of shear wave velocities of flysch formation prone to mass movements by seismic interferometry with the use of ambient noise. *Landslides*, 14(3):1225-1233.
- Heincke, B., Green, A.G., van der Kruk, J. & Horstmeyer, H. (2005). Acquisition and processing strategies for 3D georadar surveying a region characterized by rugged topography. *Geophysics*, 70, K53eK61.
- Herrmann, R.B. (2013) Computer programs in seismology: An evolving tool for instruction and research, *Seismological Research Letters*, 84:1081-1088.

- Hobiger, M., Wegler, U., Shiomi, K. & Nakahara, H. (2014). Single-station cross-correlation analysis of ambient seismic noise: application to stations in the surroundings of the 2008 Iwate-Miyagi Nairiku earthquake. *Geophysical journal international*, 198(1):90-109.
- Hotovec-Ellis, A.J., Gomberg, J., Vidale, J.E. & Creager, K.C. (2014). A continuous record of intereruption velocity change at Mount St. Helens from coda wave interferometry. *Journal of Geophysical Research: Solid Earth*, 119(3):2199-2214.
- Iannucci, R., Martino, S., Martorelli, F., Falconi, L. & Verrubbi, V. (2017, May). Susceptibility to Sea Cliff Failures at Cala Rossa Bay in Favignana Island (Italy). In *Workshop on World Landslide Forum* (pp. 537-546). Springer, Cham. in M. Mikoš et al. (eds.), *Advancing Culture of Living with Landslides*, DOI 10.1007/978-3-319-53485-5\_63, 537-546.
- Iannucci, R., Martino, S., Paciello, A., D'Amico, S. & Galea, P. (2018). Engineering geological zonation of a complex landslide system through seismic ambient noise measurements at the Selmun Promontory (Malta). *Geophysical Journal International*, 213(2):1146-1161.
- Imposa, S., Grassi, S., Fazio, F., Rannisi, G. & Cino, P. (2017). Geophysical surveys to study a landslide body (north-eastern Sicily). *Natural Hazards*, 86(2):327-343.
- Jongmans, D. & Garambois, S. (2007). Geophysical investigation of landslides: a review. *Bulletin Société Géologique de France*, 178 (2):101-112.
- Jonsdottir, F. (2018). *Estimation of Relative Seismic Velocity Changes Around Katla Volcano, Using Coda in Ambient Seismic Noise*, Department of Earth Sciences, Uppsala University, Uppsala, pp.72.
- Joswig, G. (1990). Pattern recognition for earthquake detection. *Bulletin of the Seismological Society of America*, 80(1):170-186.
- Joswig, G. (1995). Automatic classification of local earthquake data in the BUG small array. *Geophysical Journal International*, 120(2):262-286.
- Joswig, M. & Schulte-Theis, H. (1993). Master-event correlations of weak local earthquake by dynamic waveform match, *Geophysical Journal International*, 113(3):562-574.
- Joswig, M. & Wust-Bloch, G.H. (2002). Monitoring material failure in sinkholes in the Dead Sea area by four-partite small array (Seismic Navigation System-SNS). *Israel Geological Society, Annual Meeting, Maagen, Israel*. p. 54.
- Joswig, M. (2006). *Nanoseismic monitoring: method and first applications*, <http://www.nanoseismic.net/>
- Joswig, M. (2008). Nanoseismic monitoring fills the gap between microseismic networks and passive seismic. *Special topic, Leveraging Technology, First Break*, 26:117–124.

- Joswig, M., Wust-Bloch, G. H. & Leonard, G. (2002). Nanoseismology: Development of an integrated technique for the monitoring of nanoseismic events triggered by natural subsurface material failure, Israel Atomic Energy Commission, Report # 2791458, 26p.
- Lapenna, V., Lorenzo, P., Perrone, A., Piscitelli, S., Rizzo, E. & Sdao, F. (2005). 2D electrical resistivity imaging of some complex landslides in Lucanian Apennine chain, southern Italy. *Geophysics*, 70(3):B11-B18.
- Lenti, L., Martino, S., Paciello, A., Prestininzi, A. & Rivellino, S. (2012). Microseismicity within a karstified rock mass due to cracks and collapses as a tool for risk management. *Natural Hazards*, 64(1):359-379.
- Lissak, C., Maquaire, O., Malet, J.P., Lavigne, F., Virmoux, C., Gomez, C. & Davidson, R. (2015). Ground-penetrating radar observations for estimating the vertical displacement of rotational landslides. *Natural Hazards and Earth System Sciences*, 15(6):1399-1406.
- Lockner, D.A., Walsh, J.B. & Byerlee, J.D. (1977). Changes in seismic velocity and attenuation during deformation of granite. *Journal of Geophysical Research*, 82:5374–5378.
- Loke, M.H. (2004). Tutorial: 2-D and 3-D electrical imaging surveys. Geotomo Software.
- Lontsi, A. M., Ohrnberger, M., Krüger, F. & Sánchez-Sesma, F. J. (2016). Combining surface-wave phase-velocity dispersion curves and full microtremor horizontal-to-vertical spectral ratio for subsurface sedimentary site characterization. *Interpretation*, 4(4), SQ41-SQ49.
- Mainsant, G., Jongmans, D., Chambon, G., Larose, E. & Baillet, L. (2012). Shear-wave velocity as an indicator for rheological changes in clay materials: Lessons from laboratory experiments. *Geophysical research letters*, 39(19)
- Malehmir, A., Socco, L.V., Bastani, M., Krawczyk, C.M., Pfaffhuber, A.A., Miller, R.D., Maurer, H., Frauenfelder, R., Suto, K., Bazin, S., Merz, K. & Dahlin, T. (2016). Near-Surface Geophysical Characterization of Areas Prone to Natural Hazards: A Review of the Current and Perspective on the Future. In L. Nielsen (Ed.) *Advances in Geophysics* (pp. 51–146). ISBN: 9780128095331
- Martino, S., Lenti, L., Delgado, J., Garrido, J. & Lopez-Casado, C. (2016). Application of a characteristic periods-based (CPB) approach to estimate earthquake-induced displacements of landslides through dynamic numerical modelling. *Geophysical Journal International*, 206(1), 85-102.
- Martins, T.D., Vieira, B.C., Fernandes, N.F., Oka-Fiori, C., David, Montgomery, R. (2017). Application of the SHALSTAB model for the identification of areas susceptible to landslides: Brazilian case studies. *Revista de Geomorfologie*, 19:136–144.
- Maurer, H. & Hauck, C. (2007). Instruments and methods e geophysical imaging of alpine rock glaciers. *Journal of Glaciology*, 53, 110e120.

- Mendonça, A.F.; Pires, A.C.B. & Barros, J.G.C. (1994). Pseudosinkhole occurrences in Brasilia, Brazil. *Environmental Geology*, 23(1):36-40
- Menegoni, N., Meisina, C., Perotti, C. & Crozi, M. (2018). Analysis by UAV Digital Photogrammetry of Folds and Related Fractures in the Monte Antola Flysch Formation (Ponte Organasco, Italy). *Geosciences*, 8, 299.
- Méric O., Garambois S., Malet J.P., Cadet H., Gueguen P. & Jongmans D. (2007). Seismic noise-based methods for soft-rock landslide characterization. *Bulletin de la Société Géologique de France*, 178(2):137-148.
- Micromed, T. (2007). An introduction to the H/V inversion for stratigraphic purposes. Micromed, Treviso, 31 pp.
- Nakamura, Y. (1989). A method for dynamic characteristics estimation of subsurface using microtremor on the ground surface. *Quarterly Report of Railway Technical Research Institute*, 30(1):25–33.
- Nakata, N. & Snieder, R. (2014). Monitoring a building using deconvolution interferometry. II: ambient-vibration analysis. *Bulletin of Seismological Society of America*, 104(1):204–213.
- Nakata, N., Snieder, R., Kuroda, S, Ito, S., Aizawa, T. & Kunimi, T. (2013). Monitoring a building using deconvolution interferometry. I: Earthquake-data analysis. *Bulletin of the Seismological Society of America*, 103(3):1662-1678.
- Nakata, N., Snieder, R., Tsuji, T., Larner, K. & Matsuoka, T. (2011). Shear wave imaging from traffic noise using seismic interferometry by cross-coherence. *Geophysics*, 76(6):SA97-SA106.
- Niethammer, U., Rothmund, S., James, M.R., Travelletti, J. & Joswig, M. (2010). UAV-based remote sensing of landslides. *International Archives of Photogrammetry. Remote Sensing and Spatial Information Sciences*, 38(Part 5):496-501.
- Nur, A. (1971). Effects of stress on velocity anisotropy in rocks with cracks. *Journal of Geophysical Research, Wiley Online Library*, 76:2022-2034
- Obermann, A., Planès, T., Larose, E. & Campillo, M. (2013). Imaging pre-eruptive and co-eruptive structural and mechanical changes of a volcano with ambient seismic noise. *Journal of Geophysical Research*, 118(12):6285–6294.
- O'Connell, R.J. & Budsonsky, B. (1974). Seismic velocities in dry and saturated cracked solids. *Journal of Geophysical Research*, 79(35):5412-5426.
- Panzer F., D'Amico S., Lotteri A., Galea P. & Lombardo G. (2012). Seismic site response of unstable steep slope using noise measurements: the case study of Xemxija bay area, Malta. *Natural Hazards and Earth System Sciences*, 12(11):3421.
- Park, C.B., Miller, R.D. & Xia, J. (1999). Multichannel analysis of surface waves, *Geophysics*, 800–808.

- Peterson, J. (1993). Observation and modeling of seismic background noise. USA, Geological Survey Open File report 93-322, 95p.
- Planès, T., Mooney, M.A., Rittgers, J.B.R., Parekh, M.L., Behm, M. & Snieder, R. (2016). Time-lapse monitoring of internal erosion in earthen dams and levees using ambient seismic noise. *Geotechnique*, 66(4):301-312.
- Planès, T., Rittgers, J.B., Mooney, M.A., Kanning, W. & Draganov, D. (2017). Monitoring the tidal response of a sea levee with ambient seismic noise. *Journal of Applied Geophysics*, 138:253-263.
- Poupinet, G., Ellsworth, W.L. & Frechet, J. (1984). Monitoring velocity variations in the crust using earthquake doublets: An application to the Calaveras Fault, California. *Journal of Geophysical Research: Solid Earth*, 89(B7):5719-5731.
- Prieto, G.A., Lawrence, J.F. & Beroza, G.C. (2009). Anelastic earth structure from the coherency of the ambient seismic field. *Journal of Geophysical Research*, 114, B07303.
- Provost, F., Hibert, C. & Malet, J.P. (2017). Automatic classification of endogenous landslide seismicity using the Random Forest supervised classifier. *Geophysical Research Letters*, 44(1):113-120.
- Renalier F, Bièvre G, Jongmans D, Campillo, M. & Bard, P.Y. (2010a). Clayey landslide investigations using active and passive Vs measurements. In: Miller R.D., Bradford J.H., Holliger K (eds) *Advances in near-surface seismology and ground-penetrating radar*, Geophys. dev. Ser, vol15. Society of Exploration Geophysicists, Tulsa, pp. 397–414.
- Renalier, F., Jongmans, D., Campillo, M. & Bard, P.Y. (2010b). Shear wave velocity imaging of the Avignonet landslide (France) using ambient noise cross correlation. *Journal of Geophysical Research*, 115:F03032.
- Richter, T., Sens -Schönfelder, C., Kind, R. & Asch, G. (2014). Comprehensive observation and modeling of earthquake and temperature related seismic velocity changes in northern Chile with passive image interferometry. *Journal of Geophysical Research*, 119(6): 4747-4765.
- Rieke-Zapp, D.H., Wegmann, H., Santel, F. & Nearing, M.A. (2001). Digital photogrammetry for measuring soil surface roughness. *Proceedings of the American Society of Photogrammetry & Remote Sensing 2001 Conference: Gateway to the New Millennium*, St Louis, Missouri, USA. 8 pages.
- Rost, S. & Thomas, C. (2002). Array seismology: Methods and applications. *Reviews of Geophysics*, 40(3): 2-27.
- Rothmund, S. Vouillamoz, N. & Joswig, M. (2017). Mapping slow-moving alpine landslides by UAV-opportunities and limitations. *The Leading Edge*, 36:571-579.

- Saar, M.O. & Manga, M. (2003) Seismicity induced by seasonal groundwater recharge at Mt. Hood, Oregon. *Earth and Planetary Science Letters*, 214(3-4):605-618.
- Sánchez-Sesma, F.J., Rodríguez, M., Iturrarán-Viveros, U., Luzón, F., Campillo, M., Margerin, L., García-Jerez, A., Suarez, M., Santoyo, M.A. & Rodríguez-Castellanos, A. (2011). A theory for microtremor H/V spectral ratio: application for a layered medium. *Geophysical Journal International*, 186(1):221-225.
- Sasaki, Y. (1992). Resolution of resistivity tomography inferred from numerical simulation: *Geophysical Prospecting*, 54, 453–464.
- Sauvin, G., Vanneste, M., L'Heureux, J.S., O'Connor, P., O'Rourke, S., O'Connell, Y. & Long, M. (2016). Impact of data acquisition parameters and processing techniques on S-wave velocity profiles from MASW—Examples from Trondheim, Norway. In *Proceedings of the 17th Nordic Geotechnical Meeting*.
- Sauvin, S., Lecomte, I., Bazin, S., L'Heureux, J.S., Vanneste, M., Solberg, I.L. & Dalsegg, E. (2013). Towards geophysical and geotechnical integration for quick-clay mapping in Norway. *Near Surface Geophysics*, 11(6):613-623.
- Schimmel, M., Stutzmann, E. & Gallart, J. (2011). Using instantaneous phase coherence for signal extraction from ambient noise data at a local to a global scale. *Geophysical Journal International*, 184(1):494-506.
- Sens-Schönfelder, C. & Wegler, U. (2006). Passive image interferometry and seasonal variations of seismic velocities at Merapi volcano, Indonesia. *Geophysical Research Letters*, 33(21):L21302.
- SESAME (2004). Guidelines for the Implementation of the H/V Spectral Ratio Technique on Ambient Vibrations. Measurements, Processing and Interpretation. SESAME European Research Project WP12—D23.12. [http://sesame-fp5.obs.ujf-grenoble.fr/Papers/HV\\_User\\_Guidelines.pdf](http://sesame-fp5.obs.ujf-grenoble.fr/Papers/HV_User_Guidelines.pdf).
- Sgattoni, G., Gudmundsson, Ó., Einarsson, P., Lucchi, F., Li, K.L., Sadeghisorkhani, H., ... & Tryggvason, A. (2017). The 2011 unrest at Katla volcano: Characterization and interpretation of the tremor sources. *Journal of Volcanology and Geothermal Research*, 338:63-78.
- Sick, B., Guggenmos, M. & Joswig, M. (2015). Chances and limits of single-station seismic event clustering by unsupervised pattern recognition. *Geophysical Journal International* 201(3):1801–1813.
- Sick, B., Walter, M. & Joswig, M. (2014) Visual event screening of continuous seismic data by supersonograms. *Pure and Applied Geophysics*, 171(3-5):549-559.
- Silva, A.G.D. (2010). Estudo do potencial da técnica de nanossísmica para o monitoramento de hidrofraturamento em reservatórios de hidrocarbonetos, Masters Thesis, Universidade Federal Do Rio Grande Do Norte, Natal, Brazil.

- Singh, Y., Haq, A.U., Bhat, G.M., Pandita, S.K., Singh, A., Sangra, R.,..... & Kotwal, S.S. (2018). Rainfall-induced landslide in the active frontal fold–thrust belt of Northwestern Himalaya, Jammu: dynamics inferred by geological evidences and Ground Penetrating Radar. *Environmental Earth Sciences*, 77(16): 592.
- Snieder, R. & Safak, E. (2006). Extracting the building response using seismic interferometry: theory and application to the Millikan Library in Pasadena, California. *Bulletin of Seismological Society of America*, 96(2):586-598.
- Soler-Llorens, J.L., Galiana-Merino, J.J., Giner-Caturla, J.J., Jauregui-Eslava, P., Rosa-Cintas, S., Rosa-Herranz, J. & Benabdeloued, B.Y.N. (2018). Design and test of Geophonino-3D: A low-cost three-component seismic noise recorder for the application of the H/V method. *Sensors and Actuators A: Physical*, 269:342-354.
- Stanko, D., Markušić S., Strelec S. & Gazdek M. (2017). HVSR analysis of seismic site effects and soil-structure resonance in Varaždin city (North Croatia). *Soil Dynamics and Earthquake Engineering*, 92:666-677.
- Stark, T.D., Nazarian, S., Ho, C.L. & Tutumluer, E. (2013, April). Seismic testing for track substructure (ballast and subgrade) assessment for passenger/freight corridors. In 2013 Joint Rail Conference (pp. V001T01A013-V001T01A013). American Society of Mechanical Engineers.
- Stehly, L., Campillo, M. & Shapiro, N.M. (2007). Traveltime measurements from noise correlation: stability and detection of instrumental time shifts. *Geophysical Journal International*, 171:223-230.
- Su, L.J., Xu, X.Q., Geng, X.Y. & Liang, S.Q. (2017). An integrated geophysical approach for investigating hydro-geological characteristics of a debris landslide in the Wenchuan earthquake area. *Engineering Geology*, 219: 52-63.
- Taira, T. & Brenguier, F. (2016). Response of hydrothermal system to stress transients at Lassen Volcanic Center, California, inferred from seismic interferometry with ambient noise. *Earth, Planets and Space*, 68(1):
- Tonnellier, A., Helmstetter, A., Malet, J.P., Schmittbuhl, J., Corsini, A. & Joswig, M. (2013). Seismic monitoring of soft-rock landslides: the Super-Sauze and Valoria case studies. *Geophysical Journal International*, 193(3):1515-1536.
- Varnes, D.J. (1978). Slope movement types and processes. In: Schuster RL, Krizek RJ (eds) *Landslides: analysis and control*. Spec rep 176. Transportation Research Board, National Research Council, Washington, DC, pp 11–33.
- Voisin, C., Garambois, S., Massey, C. & Brossier, R. (2016). Seismic noise monitoring of the water table in a deep-seated, slow-moving landslide. *Interpretation*, 4(3):SJ67-SJ76.

- Vouillamoz, N. (2015). Microseismic characterization of Fribourg area (Switzerland) by Nanoseismic Monitoring, PhD Thesis, Institute of Geoscience, Stuttgart University, Stuttgart, Germany.
- Vouillamoz, N., Rothmund, S. & Joswig, M. (2018). Characterizing the complexity of microseismic signals at slow-moving clay-rich debris slides: the Super-Sauze (southeastern France) and Pechgraben (Upper Austria) case studies. *Earth Surface Dynamics*, 6(2):525
- Walter, M. & Joswig, M. (2008). Seismic monitoring of fracture processes generated by a creeping landslide in the Vorarlberg Alps. *First Break* 26(6).
- Walter, M. & Joswig, M. (2012). Seismic monitoring of precursory fracture signals from a destructive rockfall in the Vorarlberg Alps, Austria. *Natural Hazards and Earth System Sciences*, 12(11):35-45.
- Walter, M. Niethammer, U., Rothmund, S. & Joswig, M. (2009). Joint analysis of the Super-Sauze (French Alps) mudslide by nanoseismic monitoring and UAV-based remote sensing. *First Break*, 27(8):53–60.
- Walter, M., Arnhardt, C. & Joswig, M. (2012). Seismic monitoring of rockfalls, slide quakes, and fissure development at the Super-Sauze mudslide, French Alps. *Engineering Geology*, 128:12–22.
- Walter, M., Gomberg, J., Schulz, W., Bodin, P. & Joswig, M. (2013). Slidequake generation versus viscous creep at softrock-landslides: synopsis of three different scenarios at Slumgullion Landslide, Heumoes Slope, and Super-Sauze Mudslide. *Journal of Environmental & Engineering Geophysics*, 18(4):269–280.
- Walter, M., Schwaderer, U. & Joswig, M. (2015). Analysis of pre-collapse failure signals from a destructive rockfall by Nanoseismic Monitoring. *Engineering Geology for Society and Territory- Volume 2:1531-1535*.
- Walter, M., Walser, M. & Joswig, M. (2011). Mapping rainfall-triggered slidequakes and seismic landslide-volume estimation at Heumoes slope. *Vadose Zone Journal* 10(2):487-495.
- Wapenaar, K. (2004, January). Relations between reflection and transmission responses of 3-D inhomogeneous media. In 2003 SEG Annual Meeting. Society of Exploration Geophysicists.
- Wegler, U. & C. Sens-Schönfelder (2007). Fault zone monitoring with passive image interferometry. *Geophysical Journal International*, 168:1029-1033.
- Wubda, M., Descloitres, M., Yalo, N., Ribolzi, O., Vouillamoz, J.M., Boukari, M., ... & Séguis, L. (2017). Time-lapse electrical surveys to locate infiltration zones in weathered hard rock tropical areas. *Journal of Applied Geophysics*, 142, 23-37.

- Wust-Bloch, G.H. & Joswig, M. (2006). Pre-collapse identification of sinkholes in unconsolidated media at Dead Sea area by “nanoseismic monitoring” (graphical jackknife location of weak sources by few, low-SNR records). *Geophysical Journal International*, 167(3):1220-1232.
- Wust-Bloch, G.H. & Tsesarsky, M. (2013). Structure health monitoring in natural environments: pre-failure event location and full-waveform characterization by Nanoseismic Monitoring. *Journal of Environmental & Engineering Geophysics*, 18(4): 219–232.
- Wust-Bloch, H.G. (2009). Characterizing and locating very weak ( $-2.2 \geq M_l \geq -3.4$ ) induced seismicity in unstable sandstone cliffs by nanoseismic monitoring. *Pure and Applied Geophysics*, 167(1-2):153-167.
- Anthony, R.E., Aster, R.C., Ryan, S., Rathburn, S. and Baker, M.G. (2018). Measuring mountain river discharge using seismographs emplaced within the hyporheic zone. *Journal of Geophysical Research: Earth Surface*.
- Yalcinkaya, E., Alp, H., Ozel, O., Gorgun, E., Martino, S., Lenti, L., & Coccia, S. (2016). Near-surface geophysical methods for investigating the Buyukcekmece landslide in Istanbul, Turkey. *Journal of Applied Geophysics*, 134:23-35.
- Zoby J.L.G. (1999). Hidrogeologia de Brasilia–DF, Bacia do Ribeirão Sobradinho. Programa de Pós-graduação em Geociências, Universidade de Sao Paulo. Dissertação de Mestrado, 178p.